

Design and Control approaches for Energy Harvesting Wireless Sensor Networks



Thesis submitted for the degree of Doctor of Philosophy at

Department of Electric Engineering and Information Technology
UNIVERSITY FEDERICO II
Naples, Italy

by

Antonio Frezzetti

Tutor
Prof. Sabato Manfredi

Company Tutor
Eng. Antonio Bisogno

March 2016

*We are just an advanced breed of monkeys on
a minor planet of a very average star. But
we can understand the Universe. That makes
us something very special.*

— Stephen Hawking

Abstract

WIRELESS Sensor Networks are monitoring infrastructures composed of sensing (measuring), computing, and communication devices used to observe, supervise and monitor environmental phenomena. Energy Harvesting Wireless Sensor Networks (EH-WSN) have the additional feature to save energy from the environment in order to ensure long life autonomy of the entire network, without ideally the human intervention over long periods of time.

The present work is aimed to address some of the most significant limitations of the actual EH-WSN, making a step forward the perpetual operation of EH-WSN. In this dissertation, design methodology and management policies are proposed to improve EH-WSN in terms of application performances, traffic congestion and energy efficiency. The study explicitly targets to energy-efficient affordable ways to develop more reliable and trustworthy EH-WSN, capable to ensure long life and desired performances. The presentation is organized into two macro sections, or *Parts*: the first one is dedicated to design the main EH-WSN hardware and software parameters that affect the energy efficiency of a sensor node, while in the second part three dynamic control strategies are proposed to outperform the EH-WSN in terms of energy efficiency, traffic congestion and application requirements. The topic of each *Part* is briefly outlined hereafter.

Preliminary, the problem of the static co-design of EH-WSN is addressed. Indeed, in *Part I.* the design procedures of parameters related to both harvesting system and to data compression techniques are proposed. In particular, in **Chapter 2** an approach for hardware co-design of a system to cope with supply autonomy and conversion efficiency is provided. In **Chapter 3** a Co-design procedure aimed to select the data compression algorithm and its related parameters in order to improve WSN autonomy and signal reconstruction performance is studied.

In *Part II.*, the EH-WSN structure is conceptually divided into three layers of abstraction (physical, transport and application layer) and for each one a control strategy to enhance the WSN performances is devised. Specifically, in **Chapter 4** a model predictive strategy to cope with *physical layer* limitations, such as energy storage management from harvesting source and battery degradation is proposed. Differently, in **Chapter 5** a distributed control algorithm at the *transport layer* aimed to regulate data traffic subject to link capacity and power consumption constraints is proposed. In **Chapter 6** it is presented a control law at the *application layer* that takes into account

the energy resource at each node and the desired level of data accuracy to regulate the network throughput is proposed. Finally, conclusions are given.

Acknowledgments

THE doctorate is part of the project "Dottorato di Ricerca in Azienda" - POR Campania F.S.E. 2007/2013, Axis IV, sponsored by the Italian Ministry of Education, University and Research (MIUR) and by the Campania region and has been with the department of Electrical Engineering and Information Technology (DIETI) of the University Federico II in Napoli. Activities have been carried out in partnership with Medinok Spa in Volla (Napoli) and with the department of Electrical and Electronic Engineering at the Imperial College University in London.

Foremost, among those I would like to thank, is the PhD Tutor Prof. Sabato Manfredi for his guidance and support throughout my research. His work reminded me that theory and practice should be always in balance. I am grateful for all his thorough help with papers that made me realise the importance of good presentation. Together with Prof. Mario Pagano, the supervisor of my Master Thesis at University Federico II of Naples, he is the main source of inspiration for choosing my thesis topic on Wireless Sensor Networks, and helped me to grow from being a student, to become a more responsible and disciplined thinking scientist. A special thank goes to Prof. David Angeli, Imperial College London, for having introduced me to the model predictive control theory and application. I feel to thank also Dr. Francesco Tedesco, post doctorate at University of Calabria, for his productive comments and for all the interesting discussions we had during the time spent together in London.

The work activities at Medinok Spa in Napoli and with their Research & Development group department settled in Salerno has given me the opportunity to grow up as electronics engineer and firmware C and Java programmer. With them, I have gained the expertise to cover the activities of a whole life cycle of a project, starting from its design and arriving to the hands-on implementation and testing. So, I feel to be deeply thankful to the Medinok R&D team and to each of its components. In particular, a special thank you is to Eng. Eugenio Venere, for the time spent during our meetings in defining the 'common path' between the academic purpose and the company interest about my research topic. I am also profoundly thankful to Eng. Antonio Bisogno and to Eng. Mario Pucciarelli for having shared with me their enthusiasm, their know-how and their expertise in electronics and wireless sensor network fields.

Thanks to all the friends I met throughout this experience. I am grateful to Luigi, Onyema, Steve and Alexis for their warm friendship, for our jogging time and for our endless and inspiring conversations. A great thank you is to Tiziana ed Edmondo, research colleagues and friends of adventure at University Federico II. Finally, a loving thank goes to my family and my sweet girlfriend for their continuous presence, support and encouragement.

Again, my heartfelt thanks to all of you.

Napoli, March 2016
Antonio Frezzetti

Contents

1. Introduction	1
1.1. Wireless node	1
1.1.1. On-board micro-controller	2
1.1.2. On-board sensors	2
1.1.3. Transceiver Module	3
1.2. Harvesting system	4
1.2.1. Harvesting controllers overview	4
1.2.1.1. Solar harvesting controllers	4
1.2.1.2. Vibrational harvesting controllers	5
1.2.1.3. Thermoelectric harvesting controllers	5
1.2.1.4. RF antenna harvesting controllers	5
1.2.2. Overview on energy accumulation devices	6
1.3. Applications	7
1.4. Issues in WSN	9
1.4.1. Energy	9
1.4.2. Wireless communication	10
1.4.3. Network Self-Organization	10
1.4.4. Security	11
1.4.5. Node Unit Costs	11
1.4.6. Space Constraints	11
1.5. Challenges in WSN	11
1.6. Thesis outline and contribution	13

I. Procedures for EH-WSN Co-Design	15
2. Co-design of Harvesting control system	1
2.1. Introduction	1
2.1.1. Contribution	2
2.2. Solar harvesting control system scheme	4
2.2.1. PV and C_{IN}	4
2.2.2. Controller and Converter blocks	4
2.2.3. C_{UC} and the WSn load	4
2.3. Harvesting control system analysis and efficiency evaluation	5
2.3.1. $\bar{\eta}_{AP}$ evaluation	5
2.3.2. $\bar{\eta}_{TP}$ evaluation	7
2.3.3. $\bar{\eta}$ evaluation	8
2.4. System design methodology	8
2.4.1. WSn power consumption model	8
2.4.2. System performance	9
2.4.3. Constraints on the UC	9
2.4.4. Design conditions	10
2.5. An example of design procedure	11
2.5.1. Design condition formulation	12
2.5.2. Co-design procedure	15
2.6. Experimental validation	15
2.7. Conclusion	17
3. Co-design of Compressive Sensing methods	20
3.1. Introduction	20
3.1.1. Related works	21
3.1.2. Contributions and chapter outline	23
3.2. Network Model Formulation	23
3.2.1. Node upstream	24
3.2.2. Node energy model	26
3.3. Performance metrics	27
3.3.1. T_l metric	27
3.3.2. Reconstruction error metrics: $MSE^{(m)}$, $MSE^{(n_Y o)}$	28
3.4. WSN co-design tool	28

3.5.	Case Studio: Compressive Sensing co-design	30
3.5.1.	Compressive Sensing Modelling	30
3.5.2.	CS approaches in WSN	32
3.5.2.1.	classic CS (cCS)	32
3.5.2.2.	random sampling CS (rsCS)	33
3.5.2.3.	adaptive CS (aCS)	33
3.5.3.	Co-design example of Compressive Sensing methods	34
3.5.3.1.	cCS and rsCS analysis	35
3.5.3.2.	aCS analysis	37
3.5.3.3.	Discussion	38
3.6.	Conclusion	39

II. Control approaches for EH-WSNs 40

4.	Control techniques for harvesting system energy management 41
4.1.	Motivation 41
4.2.	Related works 42
4.2.1.	Chapter contribution and outline 44
4.3.	Background 45
4.4.	System modelling 46
4.4.1.	Ultracapacitor and Battery electrical models 47
4.4.1.1.	Ultracapacitor 47
4.4.1.2.	Battery 49
4.4.1.3.	State-of-Health (SOH) 51
4.4.2.	State-Space model 53
4.5.	Energy management strategies development 54
4.5.1.	MPC-based energy management strategy 55
4.5.2.	Threshold-based energy management strategy 55
4.5.3.	Adaptive energy management strategy 57
4.5.4.	Controller performances 58
4.6.	Simulation validation 59
4.6.1.	MPC-based energy management strategy 61
4.6.2.	Threshold-based energy management strategy 63
4.6.3.	Adaptive energy management strategy 64
4.6.4.	Performance comparison and remarks 66

4.7. Conclusion	67
5. Distributed flow control in EH-WSN	69
5.1. Motivation	69
5.1.1. Related works	70
5.1.2. Contribution and chapter outline	71
5.2. Wireless Network definition	72
5.2.1. Data traffic model	72
5.2.2. Battery model	73
5.3. Optimal flow control in EH-WSN	73
5.3.1. Primal Problem formulation	73
5.3.2. Lagrangian Dual Approach	74
5.3.3. Distributed optimization	75
5.4. Distributed flow control law formulation	76
5.4.1. Penalty function $\mathbf{\Gamma}$	76
5.4.2. Generation rate control \mathbf{F}	77
5.5. Convergence and stability analysis	77
5.5.1. Convergence analysis	78
5.5.2. Stability analysis	78
5.6. Simulation Validation	83
5.7. Experimental validation	84
5.7.1. Flow control protocol implementation	85
5.7.2. Setup overview	85
5.7.3. Experimental results	89
5.8. Conclusion	91
6. Double Layer control for EH-WSN	94
6.1. Motivation	94
6.1.1. Related Works and chapter Contribution	94
6.1.2. Chapter Organization and Notation	95
6.2. Random Sampling Compressive Sensing in EH-WSN	96
6.3. Network Performances	97
6.4. The two-layer controller scheme	98
6.4.1. Global controller	98
6.4.2. Local controllers	99
6.4.3. The two-layer controller implementation	101

6.5. Simulation validation	101
6.5.1. Nominal scenario	102
6.5.2. Presence of Energy Harvesting process	106
6.5.3. Controller tracking performance	107
6.6. Conclusion	108
7. Conclusions	110
A. Appendix to Chapter 2	112
B. Appendix to Chapter 4	116
C. Appendix to Chapter 5	122

List of Figures

1.1. Generic WSN network structure.	7
1.2. A simplified multi-layer stack for the EH-WSN.	12
2.1. General solar harvesting control system scheme for a WSn.	2
2.2. Time evolution of the controlled v_{CIN}	5
2.3. The solar harvesting control system scheme considered for the design example.	11
2.4. (a) Experimental setup carried out in the validation section; (b) A detail of the prototyped Solar Harvesting Control System: [1] PV cell, [2] Converter, [3] Controller, [4] UC, [5] the supplied TI <i>eZ430 – RF4500</i> mote.	16
2.5. Dynamic evolution of: (a) v_{CIN} (continuous line) and V_{MPP} (dashed line); (b) V_{UC} ; (c) I_L	17
3.1. Centralized-fusion WSN infrastructure.	21
3.2. The adopted WSN simulator tool.	28
3.3. Network Lifetime (T_l) vs (a) n_Y for cCS (continuous line) and (b) ρ_s for rsCS (continuous line). No-compression approach (dashed lines).	35
3.4. Reconstruction error $MSE^{(n_Y)}$ for: (a) cCS as function of n_Y and (b) rsCS as function of $\bar{n}_Y(\rho_s)$, in ideal case of no-packet loss (continuous lines) and if packet collisions are considered (dashed lines).	36
3.5. aCS: dynamic evolution of (upper panels) μ and (lower panels) reconstruction errors $MSE^{(n_Y)}-MSE^{(n_Y o)}$ (continuous lines - dashed lines with star markers respectively) under the case of (a) absence of packet loss and (b) presence of packet loss.	37
4.1. Overview of hybrid power system topologies: (a) to (d) schemes studied in literature; (e) the proposed hybrid scheme.	42
4.2. Proposed hybrid system for WSN.	46

4.3.	Ultracapacitor equivalent dynamic model.	47
4.4.	Dynamic response of an UC model.	48
4.5.	Battery equivalent model: (a) SOC dynamics, (b) voltage dynamics.	49
4.6.	Example of non linear and linearly approximated relation between SOC_B and V_{oc}^B	49
4.7.	Dynamic response of an BA model.	50
4.8.	MPC-based strategy, simulation of the first scenario: (a) solar current profile \hat{u}_h ; (f) and (g) optimal decision variables; (b) and (c) input current and outputs of ultracapacitor; (d) and (e) input current flow and outputs of battery; (h) Harvesting rate utilization index ρ_h and node allocation index ρ_l ; (j) Battery degradation index ρ_B over simulation time.	60
4.9.	MPC-based strategy, simulation of the second scenario.	62
4.10.	Threshold-based energy management strategy: simulation of first scenario.	63
4.11.	Threshold-based energy management strategy: simulation of second scenario.	64
4.12.	Adaptive energy management: simulation of the first scenario.	65
4.13.	Adaptive energy management: simulation of the second scenario.	66
5.1.	Network topology considered for the simulation validation scenario of Sec. 5.6.	83
5.2.	Dynamic evolution of the proposed simulation scenario.	84
5.3.	A Wireless Sensor Node, named "Medimote" (photo by courtesy of Medinok Spa.) used in the experimental validation section.	86
5.4.	Setup description: (a) Measurement setup; (b) User-friendly serial interface terminal: XReTi Translator.	87
5.5.	Flowchart description of the micro-controller firmware implemented for the experimental validation section.	88
5.6.	Picture of the experiment carried out at the Embedded System Laboratory, University Federico II of Naples. Particulars are highlighted: sensor nodes (from 1 to 5), gateway (G), photo-resistor (Ph).	89
5.7.	Characterization of node consumption p_i (in Watt) as function of $r_i(t)$ (in <i>packet</i> / ΔT): experimental data (black), linear fitting curve (red).	90
5.8.	Experimental results: (a) generation rates $\mathbf{g}(t)$ (continuous lines) and the respective optimal solutions of the primal problem (dashed lines), (b) aggregate rate $\mathbf{R}(t)$ and (c) the total network utility $\mathcal{U}(\mathbf{g})$	91
6.1.	General scheme of rsCS consisting of a centralized FC controller and a network of sampling nodes. On the base of incoming rate \mathbf{R}_g the FC sets the control parameter p_{FC} in order to achieve the desired $\overline{\text{MSE}}$	95

6.2.	Global controller at the FC layer.	98
6.3.	Local controllers implemented at each node i -th: box 1) controller of node sampling probability $p^{(i)}$; box 2) routing energy-aware controller of node weight $\omega^{(i)}$	99
6.4.	$\mathbb{E}(\mathbf{MSE})$ performance achieved with the S-rsCS strategy under rsCS with $p^{(i)} = p \forall i, p \in (0, 1]$	102
6.5.	S-rsCS strategy: (a) Uniform sampling probability $p^{(i)} = p = 0.5 \forall i$; (b) Dynamic evolution of energy levels $e_i(k)$; (c) Dynamic evolution of $\varepsilon = \overline{\text{MSE}} - \text{MSE}$ with $\overline{\text{MSE}} = 0.15$	103
6.6.	EA-rsCS strategy: (a) Sampling probability $p^{(i)}$ (continuous line); (b) Dynamic evolution of energy levels $e_i(k)$; (c) Dynamic evolution of $\varepsilon = \overline{\text{MSE}} - \text{MSE}$ with $\overline{\text{MSE}} = 0.15$	104
6.7.	TL-rsCS strategy: (a) Sampling probability $p^{(i)}$ (continuous line), sampling reference p_{FC} (thick line); (b) Dynamic evolution of energy levels $e_i(k)$; (c) Dynamic evolution of $\varepsilon = \overline{\text{MSE}} - \text{MSE}$ (continuous line) and $\hat{\varepsilon} = \overline{\text{MSE}} - \widehat{\text{MSE}}$ (dashed line) with $\overline{\text{MSE}} = 0.15$	104
6.8.	EA-rsCS in the presence of non uniform initial battery energies and Energy Harvesting: (a) Sampling probability $p^{(i)}$; (b) Dynamic evolution of energy levels $e_i(k)$; (c) Dynamic evolution of $\varepsilon = \overline{\text{MSE}} - \text{MSE}$ with $\overline{\text{MSE}} = 0.15$	105
6.9.	TL-rsCS in the presence of non uniform initial battery energies and Energy Harvesting: (a) Sampling probability $p^{(i)}$ (continuous line), sampling reference p_{FC} (thick line); (b) Dynamic evolution of energy levels $e_i(k)$; (c) Dynamic evolution of $\varepsilon = \overline{\text{MSE}} - \text{MSE}$ (continuous line) and $\hat{\varepsilon} = \overline{\text{MSE}} - \widehat{\text{MSE}}$ (dashed line) with $\overline{\text{MSE}} = 0.15$	106
6.10.	Tracking performance of the TL-rsCS strategy: (a) Sampling probability $p^{(i)}$ and reference p_{FC} (thick line); (b) Dynamic evolution of energy levels $e_i(k)$; (c) Dynamic evolution of $\varepsilon = \overline{\text{MSE}} - \text{MSE}$ (continuous line) and $\hat{\varepsilon} = \overline{\text{MSE}} - \widehat{\text{MSE}}$ (dashed line) with $\overline{\text{MSE}} = 0.15$	107
A.1.	Schematic for the MPPT topology: (a) Converter and controller; (b) detail for the timer.	113
B.1.	Hardware implementation for the hybrid system scheme in Fig. 4.2.	116
B.2.	From LTC3330 Datasheet: Efficiency of the integrated (a) Buck-Boost Converter and (b) Buck Converter under different current load conditions.	117
B.3.	From NTGD1100L Datasheet: a) Simplified Internal scheme; b) Series ON resistance as function of input voltage.	118

B.4. From LT6118 Datasheet: a) Simplified Internal scheme and polarization; b) Amplifier gain vs. input frequency.	119
B.5. CAD design of the Smart Harvester board (Altium Designer): a) PCB layout and b) 3D view.	120
B.6. A photo of the proposed hybrid system scheme.	121
C.1. Set definition for the LaSalle invariance principle.	123

Introduction

A wireless sensor network (WSN) [1, 2, 3] is an infrastructure composed of sensing (measuring), computing, and communication devices that is used to observe, supervise and react to events and phenomena into the environment where it has been allocated. The environment can be the physical world, a biological system, or an information technology (IT) framework. Sensor devices, or wireless nodes (WSn) or also motes [4, 5, 6, 7, 8], send messages to a central unit, or Fusion Center (FC). In this chapter, WSNs are presented in many of its aspects: starting from a description of wireless sensor nodes' properties, the WSN is analysed from the point of view of its usage in many market sectors, such as industry, navy, health care diagnostic and medicine. Then, the most relevant challenges in actual WSN technology are presented. It is underlined that current technical limitations turn the WSN to be not completely considered trustworthy, although the technology is almost mature, and the design of the network is the result of trade-offs of autonomy, traffic and application performances. Conclusions and Thesis outline are then provided.

1.1. Wireless node

Today's wireless sensors can be described as smart inexpensive devices with multiple on-board sensing elements. They are typically used to retrieve information from environment and to communicate such local data to collecting (monitoring) stations that aggregate some or all of the information. They are then typically characterized by on board sensors for data environment sensing and by a wireless transceiver for communication purpose. Nevertheless, they are capable of local micro-controller unit (MCU) and data storage memory for manage data communication flow and sensed data. Typically deployed over remote and extended area in lack of a stable supply energy from grid infrastructure (line feed), it is even more extensive the usage of stand-alone supply systems that extract energy directly from the environment by means of power controllers. Such supply

systems which make use of alternative source of energy are typically named "Harvesting systems", because of their capacity of collect energy and "harvest" it into an accumulation device.

In the following of the section, each component of sensor node will be described in details.

1.1.1. On-board micro-controller

Each sensor node is equipped with a MCU which acts as a local control center for collecting and processing data, arbitrating its behaviour to manage network communication and traffic data. Typically, high clock frequency and low power consumption performances are required. Additionally, embedded peripherals required are: analogue-to-digital converter (ADC) unit to sample analogue voltage levels, serialized logic (UART, I2C) for communication with sensors and with the RF module, internal memory for quick data consultation, pulse width modulation (PWM) for driving logic purpose. With the current technology, MCU can operate in the range of frequencies from 31 kHz to 125 MHz. The energy required for computation is function of the operative frequency. For low power and low computational overhead, 31 kHz can be considered. In other cases, higher frequency values may be set accordingly to the required performance.

1.1.2. On-board sensors

A sensor is an electronic device that converts a physical quantity into an electrical signal. Sensor nodes are equipped with one or more sensors and with on-board signal processing capabilities for extraction and manipulation of physical environment information. Sensors can be used to study and monitor a variety of phenomena and environments. Perhaps the more logical way to classify on-board sensors is with regards to the physical signal they are able to measure from the environment. The most common categories include:

- 1) Meteorological Sensors. In this class of sensors, temperature and humidity sensors and light sensors fall. A temperature sensor bases the temperature estimation on a change in a physical parameter (voltage drop of a diode junction) that corresponds indirectly to a temperature change. Similarly is the way a light sensor estimates the incident light intensity. Most common humidity sensors are in counterpart based on capacitive, resistive, or thermal conductivity measurement techniques because of the huge number of ways it is measured into: absolute humidity measurements (ratio of water vapour to the volume of substance), relative measurements (compared to the saturated moisture level) or dew point measurements (temperature and pressure at which the observed gas starts to turn into liquid).

- 2) Inertial sensors. With the technological improvement in the field of silicon integration, inertial sensors are rapidly becoming ubiquitous with their adoption into many types of consumer electronics products, including smart phones, tablets, sensor network, robotics. Based on Micro Electro-Mechanical (MEMs) technology, their adoption in the fields of low power sensors has been promoted by the steep reduction in cost, space occupation and energy expenditure. Typically this class of sensors is able to measure: pressure, velocity, vibration and acceleration from essentially the measure of micro-scaled variations of integrated capacitances.
- 3) Chemical sensors. This class of sensors detect the presence or concentration of particle chemical elements or compounds in a given sample. A chemical sensor usually consists of a chemically sensitive film or a membrane and a transducer. A chemical process occurring in or on a chemically sensitive film or membrane causes a signal to be generated at the transducer. Examples of mechanisms commonly employed include host-guest binding, catalytic reactions or a red-ox process. Chemical sensors have a vast variety of applications ranging from medical diagnostics and nutritional sciences through security to automotive industry.

1.1.3. Transceiver Module

In the past years, communication among nodes have been based on vendor's proprietary technology out of standard. Communication was only possible among nodes of the same type and the home development of WSn platform was difficult or impossible to be done. WSns typically transmit small volumes of simple data (e.g., threshold-based alarms). In the early 2000s, standardization of wireless communication was established. Initially, the IEEE Wi-Fi standard 802.11b for sensors were used for node communication. However, this standard results to be too complex and allocates more bandwidth than is actually needed for typical sensors. In a second instance, Bluetooth (IEEE 802.15.1) technology was taken into consideration, but it was too energy expensive and therefore not suitable for low power consumption devices. The emerging constraint requirements on WSN technology has opened the door for a new standard (the IEEE 802.15.4) along with the ZigBee (more specifically, ZigBee is based on the IEEE 802.15.4 and comprises additional software layers to obtain an user friendly wireless device). IEEE 802.15.4 operates in the 2.4 GHz radio band and supports data transmission at rates up to 250 kbps at ranges from 30 to 200 ft. With the emergence of the ZigBee/IEEE 802.15.4 standard, systems are expected to transition to standards-based approaches, allowing not homogeneous sensors to transfer data through a standardized ways. ZigBee/IEEE 802.15.4 is targeted at commercial point-to-point sensing applications where low power and low cost are required for the implementation [9].

1.2. Harvesting system

With technological progress, wireless sensors are becoming even more compact in size and reduced in weight. They can be considered as portable devices at all, and consequently it is even more frequent the use of batteries to supply this technology. The use of battery, however, puts a significant limitation to the reliability of motes. Limited lifetime is a key bottleneck for most battery equipped devices. Studies on low power strategies try to maximize the battery lifetime and therefore to minimize the rate of battery replacement. Harvesting technology has been widely recognized as a promising approach to ensure the sustainability of the network, extending sensors' lifetime. WSN supplied with an Energy Harvesting system is in literature usually indicated with the acronym of EH-WSN. Typical harvesting transducers adopted for portable electronics are: small size solar panels, thermoelectric, vibrational cells and RF energy harvesting antenna. Harvesting transducers are characterized by random energy availability. This causes a huge difference in energy accumulation and supply electronics than grid connected devices. Moreover, electronic systems for energy harvesting differ one to another in relation with the specific renewable source adopted. A brief overview of harvesting controllers and their operative principles will be treated in the following of this section. Aside from their specific implementation, harvesting controllers are characterized by one synthetic parameter that is the efficiency of conversion. It represents the ability of the harvesting system to collect the environmental energy, convert and store it into local accumulation device, e.g. battery.

1.2.1. Harvesting controllers overview

In what follows, a brief introduction of harvesting controllers is provided. They will be classified on the basis of the harvesting generator typology (solar, vibration, thermoelectric, radio-frequency) they are designed to deal with. A reach discussion of the above controllers is behind the scope of this chapter. For additional information about principles of operations and manufacturing process, the reader is referred to the numerous literature on this topic (e.g. [10, 11, 12, 13]).

1.2.1.1. Solar harvesting controllers

The interaction of photons and semiconductor materials composing a solar cell causes the generation of a current of electrons through a phenomenon that is address with the name of photovoltaic effect. A solar cell can be modelled as an unideal current generator, characterized by a non linear dependence between voltage drop and current generated. Solar cell provides the maximum power if it works at a specific polarization point, that for convention is named with Maximum Power Point

(MPP). Therefore, a fundamental behaviour for harvesting controller is to maintain the polarization point in the nearby of MPP. Additionally, since the maximum generated power depends on the solar light intensity, the MPP varies with light intensity. Clearly, a solar harvesting controller tracks the MPP over time, as function of light conditions.

1.2.1.2. Vibrational harvesting controllers

Many sources of vibrations can be recognized ranging from human motion machines industrial. Crowd walking on the street, motor rotation, noise pollution are all examples of energy convertible into electricity. Harvesting cells that convert vibrations into electricity base their working principle on the piezoelectric effect. The piezoelectricity is the interaction between the mechanical and the electrical state in certain crystalline materials. It is a reversible process in that materials generates a certain amount of charge as consequence of an applied mechanical force. Also in this case, there exists a polarization point where the maximum power conversion is achieved, and then a harvesting controller may track and polarize the source at its MPP. Unfortunately, since crystals produce the maximum power transfer at their resonance frequency, the crystal must be specifically chosen in relation with the vibration frequency of the source, in order to achieve the maximum power transfer.

1.2.1.3. Thermoelectric harvesting controllers

Gradients of temperature between two faces of a material can be converted in electrical power by means of the so called Seebeck effect: a junction of two different types of wire at different temperatures lead to a voltage drop across the wires. Since thermocouples are based on metals, they are able to withstand high differences of temperature, then high power can be generated by thermocouples. Many heat sources can be found in nature (sun heat, geysers, etc.) as well as in man-made machinery (pumps and motors, steam pipes, etc.). These represent an immense source of convertible energy.

1.2.1.4. RF antenna harvesting controllers

The recovery of energy from electromagnetic radiation devices through radio waves is nowadays presented as a viable power source. This statement is based on the fact that the amount of transmitted and received signals, and the powers in play in the spectrum of Radio frequency is dramatically increased. The power required by the loads currently is of the order of milliwatts or micro watts. There are many signals of different frequencies in the environment that can be recovered and, also if these signals carry a small amount of power, the possibility to harvest from RF has been studied. The spectra available in different sectors have different characteristics that depend on many

	Lead acid	NiMH	Li-ion	Ultracapacitor
Nominal voltage	2V	1.2V	3.3V-3.6V	2.3V-2.5V-2.7V
Specific energy	30-45 Wh/kg	30-80 Wh/kg	90-220 Wh/kg	10-20 Wh/kg
Specific power	180 W/kg	250-1000 W/kg	600-3400 W/kg	10 kW/kg
Cycle life	500-800	500-1000	1000-8000	>10k
Relative costs	Low	Moderate	High	Highest

Table 1.1.: Performance comparison on different accumulation device technologies.

environmental variables. For example the efficiency of the power transfer depends on the distance between RF energy source and receiver, the antennas’ mutual coupling, presence of moisture in the air. Nevertheless the advantage in recharge batteries through RF power has a main importance especially in such fields where human intervention is dangerous or invasive for the life, as in medicine surgery.

1.2.2. Overview on energy accumulation devices

Many of today’s WSNs rely on energy accumulation device as the primary supply source. Both batteries and ultracapacitors can be used to supply WSNs. Mature is technology of rechargeable batteries. Their recharging property is based on the chemical reduction-oxidation reaction. More recent is the technology behind ultracapacitors. Two different chemical technologies are integrated: electrostatic double-layer capacitance and electrochemical pseudo-capacitance. The first one uses carbon electrodes or derivatives to achieve separation of charge. Like capacitors, ultracapacitors store energy in an electric field, which is created between two oppositely charged particles when they are separated. On the other hand, electrochemical pseudo-capacitors use metal oxide or conducting polymer electrodes with elevated porosity to obtain charge-transfer with redox reactions. Like ordinary batteries, Ultracapacitors accumulate energy in terms of potential energy by the separation among positive and negative ions. In Table 1.1 a comparison of both devices batteries and ultracapacitors has been reported. As can be seen, Ultracapacitors have lower specific energy, higher specific power, very higher cycle life, and highest cost than LI-Ion batteries. The complementary performances of the two devices has encouraged in WSN the adoption of hybrid supply systems. The optimal management of accumulation devices in an hybrid supply system is nowadays an open challenge.

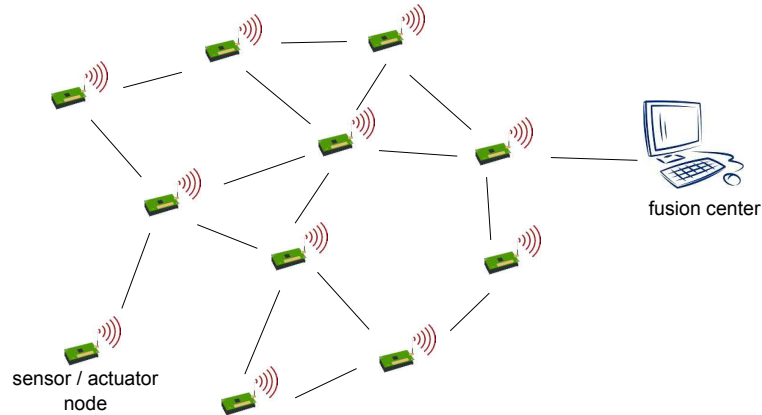


Figure 1.1.: Generic WSN network structure.

1.3. Applications

Wireless Sensors have a variety of purposes, functions, and capabilities. Traditionally, sensor networks have been used in the context of high-end applications working in hazardous areas, such as radioactive areas, war field. They have been adopted in these areas as radiation detection systems, over-the-horizon weapon sensors for navy. They have been also adopted in biomedical applications, habitat sensing, and seismic monitoring.

Besides, emerging technologies (high scale integration on silicon, MEMs, etc.) more recently has led to a decrease in the size, weight and cost of sensors and sensor arrays by orders of magnitude, and this implies a reduction in budget cost and maintenance. Large number of sensors may be integrated into systems to improve performance and sensors' versatility. As a result, WSNs composed of sensor and micro-sensors can deal with sensing and controlling functionalities in commercial applications [14]. Due to the vast and non-homogeneous gamma of applications that WSN are used in, there is a not unique way to classify WSN. First classification that is provided refers to the network structure. With reference to Fig. 1.1 we distinguishes:

1. **Centralized WSN:** WSN is characterized by a central unit, or Fusion Centre (FC), which is demanded to the coordination of the network. Sensors are considered as network end-points and repeaters, having tasks of data sampling and/or actuators. FC gathers information from the sensors, analyses such data, takes decisions and eventually gives instruction to end-points.
2. **Distributed WSN:** In this case, FC only observes the WSN from a remote terminal. Elaboration and coordination tasks are performed by sensors that have the ability to exchange information and to take collaboratively agreement on their actions.

Another classification of WSN is based on the kind of information nodes are used to exchange. The following categories are distinguished:

1. **Monitoring WSN:** Constant stream of data is transferred in this case. Exchanged data are sensed from the monitored field. Periodically reporting measured values can be taken with the help of sensors. In this case, WSN can be used for example to monitor a physical value (like room temperature). The stream rate is application dependent and is typically triggered by application or driven by the end user.
2. **Event Triggered WSN:** One message is sent when occurs a specified event. Typically, the collaboration of nearby sensors is essential to exclude an occasional local false alarm (actually the event is not occurred) or to confirm the emergency (the event has been detected also by the nearby nodes). In last case detected alarms should be report to the sink.

WSN are successfully used for many different purposes, some of that are reported hereafter.

1. **Military applications:** The development of WSNs was inspired by military applications, notably surveillance in conflict zones. Nowadays, sensors are essential for cruise control of missiles, aerial vehicles and drones. Some recent sensor networks projects such as the ZebraNet project [15] have used mobile sensor nodes with sensors mounted on soldiers or aerial vehicles to interact with spatially deployed sensor network.
2. **Medical applications:** WSN technology applications have being widely explored in number of hospitals and medical centers. It includes pre-hospital and in-hospital emergency care, disaster response, and stroke patient rehabilitation. By allowing important health parameters to be constantly collected and integrated automatically into the patient care records and used for real-time and long-term observation, it is possible to improve the monitoring of patient parameters and react on time to health complications. WSNs also permit collection of long-term medical information which populates databases of clinical data.
3. **Home Control applications:** Applications of WSN in home automation provide control and safety by facilitating flexible management of common services (lighting, heating, and cooling systems) in a smart way which minimizes the human intervention. High detailed electric, water, and gas monitoring can improve resources efficiency, reduce costs and plant maintenance.
4. **Smart cities and Traffic control:** Even more used in everyday speech is the term of 'smart cities'. It refers to cities or part of them (roads, offices, etc.) capable of an high level of

automation. In the middle of such technological revolution is the adoption of Wireless Sensor Networks to monitor and optimize cities' wastes and traffic congestion. The information about density, speed of vehicles on the road, pollutant concentration, surveillance and so on, are mansions that can be successfully performed by WSN.

5. **Agricultural applications:** Wireless sensor networks can be deployed in large farm areas. A typical agriculture application is the so called precision agriculture. In this case, the area is taken in terms of resource distribution and change in the climate, weeds and pests are taken as its response. On the basis of these results farmers decide which kind of pesticides, fertilizers and water resources must be used for the farm. Actually, types of soil, nutrient content, and other important factors vary widely from place to place. The final result of this management is to enhance the final productivity. Also for applications like this, WSN are going to be used in large scale.

1.4. Issues in WSN

Being WSNs deployed in potentially harsh, uncertain, and dynamic environments, they are envisioned to operate in an autonomous and untethered fashion. This poses considerable challenges ranging through signal processing, communication scheduling, routing control, network organization, topology discovery and energy management. In the following of this section, a summary of the most relevant issues characterizing modern WSN is discussed.

1.4.1. Energy

A current challenge is to develop low-power communication with low-cost processing and self-organizing connectivity/protocols; another critical challenge is the need for extended temporal operation of the sensing node despite a (typically) limited power supply and battery life. In particular, the architecture of the radio, including the use of low-power circuitry, must be properly selected. Low power consumption is a key factor to cope with long operating horizons for such battery supplied systems. Additionally, accumulation devices must operatively work and at the same time preserve its life degradation. In more details these two aspects are considered hereafter.

Energy-Efficient operations In lack of battery replacement or supply grid connection, sensor node may operate in an energy-efficient way. Sensor node performs many operations, such as: detection of events, local data processing, and information communication. Power consumption can therefore be allocated to three functional domains: sensing, communication, and data processing. Power management and energy conservation are critical functions for sensor networks, and

designers have to enable power-aware protocols and algorithms. Maximization of network reliability and minimization of delays are desired performances for WSN, that are in trade-off with power consumption of the network [16]. Hence, reliability, delay and power consumption coexist in trade-off that the network designers need to consider during the definition of network policies regarding the power management and the energy conservation.

Battery capacity preservation An additional way to increase the operating horizons of a wireless node is to use energy accumulation system. Basically, from a renewable source, the energy is accumulated into a battery for future on-demand utilization. There are several ways to store the energy with advantages and disadvantages in terms of energy and power ratings, life degradation issue and monetary cost. Obviously, different energy accumulation devices show different battery life degradation behaviour ([17, 18]). In fact, rechargeable battery are characterized by degradation phenomenon that leads to the reduction in battery capacity during time. In this respect, preserve battery from capacity degradation can reduce maintaining costs and increases the autonomy. Many strategies are studied in literature in order to cope with battery degradation. The most interesting way is to use hybrid accumulation systems, using two or more accumulation devices ([19, 20]).

1.4.2. Wireless communication

In a WSN, sensor data must be sent to the FC which process them for monitoring and control actions. Wireless communication is not perfect, since packets can be discarded or lost. The packet loss is a well known phenomenon in telecommunication engineering. The propagation channel is characterized by limited bandwidth, is time varying and is affected by noise. Such unideal factors causes degradation of the wireless communication between a transmitter and its receiver. Consequently, messages reach their destination in a certain amount of time. Sensor information however must reach the sink within some deadline, because out-of-date messages are generally not useful for monitoring applications. Moreover, delays of communication can also affect distributed control applications [21, 22]. In practical world, delays exist and depend on many factors: a) one-to-one link is not instantaneous, but is typically constrained by channel limitations; b) communication between source and its destination can involve intermediate nodes that work as repeaters. In this case, the overall delivery time is proportional to the number of hops.

1.4.3. Network Self-Organization

In many applications, WSN may be able to autonomously organize their communication paths by themselves. This is because in the most general case, one WSN could be deployed in mass or be injected in the sensor field individually (e.g., they can be deployed singularly by a human or

a robot or by dropping them from an helicopter). Any time after deployment, topology changes may occur. For example, change in position or additional sensor nodes can be deployed to replace faulty nodes. Therefore, although some sensor nodes may fail, this should not affect the overall operation of the sensor network. Although many protocols and algorithms have been proposed for traditional wireless ad-hoc networks, they are not well suited to cover for the WSN applications as whole [2].

1.4.4. Security

Since WSNs may operate in a hostile environment, security is crucial to ensure the integrity of sensitive information. To do so, the network traffic in certain applications is encrypted. The constrained computation and communication capability of sensor nodes make conventional encryption techniques unsuitable for WSN. More affordable and energetically efficient encryption techniques (e.g. Compressive Sensing based algorithms) have been recently proposed in the literature and the topic is under increasing consideration for researchers.

1.4.5. Node Unit Costs

Sensor networks typically are composed of a large set of sensor nodes. Clearly, monetary cost of each sensor node has to be as low as possible to keep the overall WSN cost in acceptable ranges. Besides to fixed costs, other variable costs may be taken into account. Nodes operate in hostile areas and may be designed to be robust to time degradation. This in order to reduce the cost of node replacement due to malfunctioning and battery ageing.

1.4.6. Space Constraints

Last, but not the least, is the space occupation of a sensor node. Even more applications (e.g. home automation, wearable electronics) require sensor nodes to be small in size, as small as to fit into a tight module on the order of tens of centimetres. This trend is supported by technological improvements in scale integration device trustworthy. However, even more integrated functionalities are required, so that space constraints are one of the main issues in designing sensor nodes.

1.5. Challenges in WSN

The allocation of the above resources is not a trivial task, as it affects many performances of EH-WSNs. In the following some trade-offs existing in EH-WSN:

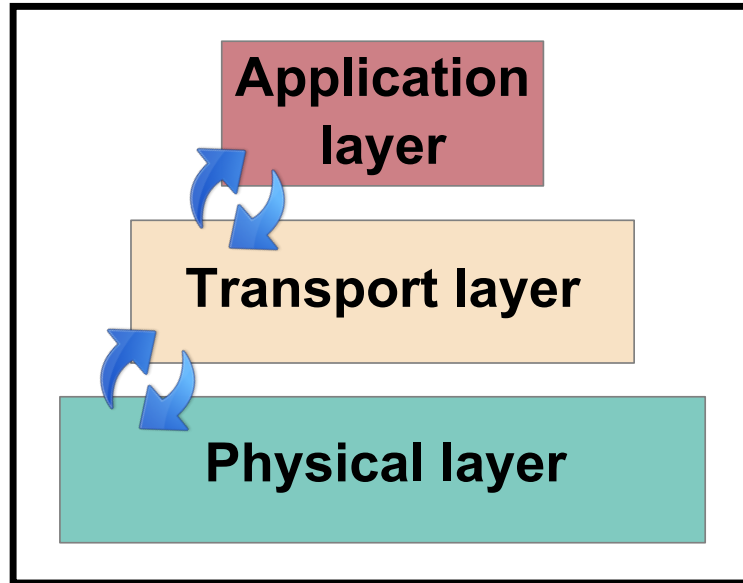


Figure 1.2.: A simplified multi-layer stack for the EH-WSN.

1. Energy saving policies and battery life preservation techniques reduce the rate at which battery has to be replaced, thus reducing cost for WSN management. The usage of rechargeable batteries with energy harvesting recharge systems can improve the node autonomy, but can also increase cost and the space occupation of sensor node.
2. In lack of the energy resource, one can try to save energy by reducing communication activity and sampling operations. This however reduces the throughput of the network.
3. In presence of packet loss, communication reliability can be improved by adopting data retransmission. This policy may however reduce the network lifetime.
4. In presence of delay, one can try to reduce the communication distance between source and destination by increasing the transmission radius. This increases the power consumption.

These examples, and many others, motivate to systematically study design and management procedures to guarantee over time energy efficient and reliable EH-WSNs. In this dissertation, the following network performances are considered: node and network lifetime, battery State-Of-Health (SOH), queue congestion and reconstruction error. Their definitions are briefly given in the following.

Lifetime of a wireless node is the time needed for the battery to run out of energy. Therefore, network lifetime will be referred to lifetime of the node in the network that faults earlier than the others during time.

Battery capacity is the maximum amount of energy that can be stored. The usage of a battery degrades its capacity over time. SOH refers to the current battery capacity normalized to the initial capacity of the battery.

In networked systems, queue congestion indicates a reduction in network communication performance due to intensive packet traffic. Queue congestion is an unwanted condition since it causes packet loss phenomena.

WSNs are distributed monitoring systems. Measurements acquired by nodes and gathered by the FC are post-elaborated to extract the original profile of monitored signals. The error between the recovered signal and the monitored one is generically referred with the name of reconstruction error.

1.6. Thesis outline and contribution

The present work is aimed to overcome some of the most significant limitations of the actual EH-WSN, making a step forward the perpetual working of EH-WSN. In this dissertation, design methodology and management policies are proposed to improve an Energy Harvesting Wireless Sensor Network performances in terms of congestion and energy efficiency. The study explicitly targets to energy-efficient affordable ways to develop more reliable and trustworthy EH-WSN, capable to ensure long life time and desired performances. The presentation is organized into two macro areas, or *Parts*: the first one is dedicated to design the main EH-WSN hardware and software parameters that impact the energy efficiency of a sensor node, while in the second part three dynamic control strategies are proposed to improve the EH-WSN performances defined in previous section. The topic of each *Part* is briefly outlined hereafter.

In *Part I.*, two works are proposed.

- In Chapter 2, a comprehensive procedure oriented to the hardware co-design of EH-WSN is provided. The procedure takes into account autonomy requirements and efficiency constraints and returns the set of main hardware components that fulfil given requirements. An example of a co-design procedure is provided and implemented to show the effectiveness of the proposed approach.
- In Chapter 3, many compression techniques, such as the Compressive Sensing, are analysed to quantitatively exploit the existing trade-off between energy efficiency and reconstruction error. From the inspection of the achieved results, one can statically choose the parameters of a compression scheme to fulfil the desired constraints on node autonomy and accuracy of compressed data. A software tool for the static co-design of data compression method is therefore derived.

The above design procedures are static and are implemented to plan a EH-WSN to cope with given performance requirements.

In *Part II.* of this dissertation, dynamic strategies are proposed to manage the available energy and network resources to cope with dynamic scenarios.

To this aim, three levels of abstraction are considered: the physical layer, the transport layer and the application layer (Fig. 1.2). In this context, at the physical layer hardware devices dynamically manages the energy harvested from the environment; at the transport layer control strategies manage data traffic and avoid congestion; at the application layer control strategies guarantee the quality of information that WSN delivers to the end users.

In the *Part II.* of this dissertation, three control strategies, one developed at each level of abstraction (physical, transport and application) are proposed to improve EH-WSNs performances. Briefly, details are summarized hereafter.

- In Chapter 4, performances of the physical layer are taken into consideration and in trade off with the energy efficiency of the node. Hybrid supply systems composed of a battery and an ultracapacitor, are proposed to ensure at the same time battery life preservation and prolonged supply autonomy. After having described the literature background about this topic, a model predictive control framework based on a novel hybrid supply system configuration is formulated and studied. Predictive controller maximizes the node autonomy and reduces the battery degradation by taking into account the estimated energy harvested by the system.
- In Chapter 5 an optimal traffic control law is implemented in order to avoid queue congestion and energy node fault. The control problem is formulated as a convex min problem and a control law is designed by using the theory of primal-dual Lagrangian decomposition. To prove the effectiveness of the proposed control law, a WSN model is provided and the distributed traffic protocol is implemented over a real EH-WSN.
- In Chapter 6, the reconstruction error is considered as application layer performance and is controlled by a multi-layer controller which takes into account the energy node availability in order to increase the network lifetime. With reference to Fig. 1.1, the controller is developed over two layers: a global controller at the FC level and local controllers at each sensor node. The global controller is aimed to regulate the signal reconstruction error to a desired value, given as set point. On the other hand, local controllers try to limit the node power consumption by controlling both the signal sampling probability and the incoming traffic rate. An extensive simulation validation is provided to demonstrate the effectiveness of the proposed approach.

Part I.

Procedures for EH-WSN Co-Design

Co-design of Harvesting control system

2.1. Introduction

THE recent development of low cost smart sensors and micro-controllers supporting network connectivity ([23]) is promoting the implementation of distributed monitoring and control algorithms in many industrial and civilian applications (e.g. environment monitoring, home automation, military and automotive industry) through architectures ([24]) composed of *Wireless Sensor nodes* (WSNs). Wireless data communication networks aim to reduce costs in both management and maintenance. One of the main challenges in the WSNs design is the energy efficiency, because nodes are usually deployed in remote area, where the access points to the electrical grid are absent. WSN load current profiles are typically impulsive. Their power consumption ranges from some μW in the sleep mode to tens of $m\text{W}$ during communication mode ([25, 25, 26, 27, 28]). Stand-alone WSN are usually equipped with renewable photovoltaic (PV) cell and storage device, that allow a perpetual solar energy supplying. In this case, a Maximum Power Point (MPP) tracking method has to be implemented in order to guarantee the maximum power production. It has been noted that WSN can be efficiently supplied by Ultracapacitors (UCs) storage device, because this technology shows higher power density, lower Equivalent Series Resistance, lower leakage current ([29, 30]) and slower degradation effects than the typical rechargeable batteries. A typical PV-based harvesting system scheme considered in the literature (e.g. [31, 31, 32]) is depicted in Fig. 2.1. It consists of: the PV cell, a power converter stage, the storage device (e.g. UC) and a solar harvesting system controller. While the power converter interfaces the PV source with the storage buffer, the controller tracks the actual MPP value and dynamically modulates the operating point of the PV cell through the converter.

Many studies investigate the efficiency of power conversion system pointing out the relation of system losses and tracking reliability with the overall system efficiency. In order to increase the

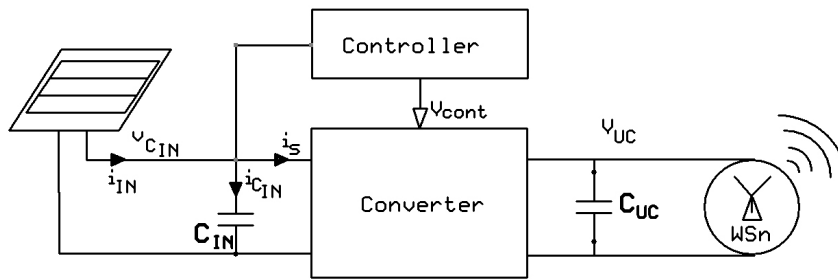


Figure 2.1.: General solar harvesting control system scheme for a WSn.

tracking reliability, in [33] authors propose to use two PV cells aimed 1) to harvest energy and 2) to instantaneously track the voltage of MPP, namely V_{MPP} value. In this setup, however, the system consumption due to the presence of two cells is neglected. Most part of schemes presented in literature (e.g. [34]) includes a single cell and a low power timer that periodically disables the harvesting process and estimates the V_{MPP} voltage value. In this case, when the irradiation variability is slow in time, the use of just a single PV cell allows to assess a good MPP tracking capability. Finally, with reference to Fig. 2.1, it is equally assessed in literature the use of buck or boost power converters ([31]), due to their low losses and high efficiency in power conversion.

With the reference of the system in Fig. 2.1, the following efficiency definitions are usually adopted in the literature and will be used hereafter: 1) MPP tracking efficiency, 2) input system efficiency and 3) converter stage efficiency. The *MPP tracking efficiency* is related to ability of the tracking algorithm to correctly estimate the real MPP. The *input system efficiency* refers to the ability of the MPPT system to dynamically seek the estimated MPP. Finally, the *converter stage efficiency* is the amount of harvested energy divided by the energy at the input of the converter and it gives indications of actual power delivered to the output as it takes into account the system power losses.

2.1.1. Contribution

In this context, this chapter derives an analytical formulation of the overall efficiency of a solar harvesting control system in Fig. 2.1. On the base of previous analysis, a design methodology is carried out to both select the PV cell and UC and design the converter and controller parameters in order to cope with the desired performance in terms of system efficiency and autonomy. As representative example, the proposed approach is used to design a low cost representative solar harvesting control system to supply an off-the shelf mote.

In the literature, only few works propose a study to design the efficiency of a PV-based harvesting system. In [32] authors derive the theoretical converter stage efficiency and the formulation is experimentally validated for different set of parameters. Based on the modelled efficiency, authors

provide a series of guidelines to design the system parameters in order to achieve only the maximization of the converter stage efficiency. In [31] authors provide a more accurate overall system efficiency formulation than in [32], taking into account also the MPP tracking efficiency and the input system efficiency. An example of system design is provided and a prototype is implemented in order to validate the effectiveness of the proposed formulation. Other works propose embedded and low consumption harvesting schemes with high efficiency (e.g. [35, 36]). Most of the above implementations are characterized by an external battery that supports the system autonomy.

In this scenario, the chapter contribution are the following:

1. in the analytical formulation, the input system efficiency is taken into account in addition to the converter stage efficiency. Moreover, differently from many formulations given in the literature, herein we explicitly consider power losses related to the switch and parasitic elements. Finally, we approximate the PV cell characteristic around the MPPT point with a complete second-order Taylor polynomial, resulting in a more accurate derivation of the input system efficiency and therefore of the overall system efficiency as well;
2. differently than existing approaches, herein is presented a systematic procedure to design the harvesting control system in order to cope with the desired performance in terms of system efficiency and autonomy. We give simple and low computationally demanding design conditions based on the above analytical derivation that considers in a unified framework the overall system efficiency, autonomy, system reliability requirements and components constraints;
3. the above procedure is used and validated to design a low cost harvesting control system prototype to supply a representative off-the-shelf Texas Instruments mote. This makes the procedure potentially applicable to the design of harvesting control system for a wide range of off-the-shelf devices;
4. finally, about the technological implementation of the developed prototype is notable that our system is completely supplied by the UC and this characteristic distinguishes our implementation from the most part of implementations found in literature.

The outline of the manuscript is given. In Sec. 2.2, the general solar harvesting control system considered in the chapter is briefly introduced. In Sec. 2.3, a theoretical analysis of the PV-based harvesting system efficiency is formulated and the system of inequalities is provided. As representative example, the proposed approach is used to design a PV-based harvesting system (Sec. 2.5) with assigned WSn load, autonomy constraints and fixed overall efficiency. Finally in Sec. 2.6, a prototype of the designed harvesting system has been implemented and the effectiveness of the design procedure has been experimentally validated with four days of experimental test.

2.2. Solar harvesting control system scheme

In this section, the PV-based harvesting system scheme depicted in Fig. 2.1 will be briefly introduced. Herein, we describe the physical function of each system component in Fig. 2.1 and we also formulate the MPP controller law.

2.2.1. PV and C_{IN}

The PV and C_{IN} devices convert the environmental solar light in the electric power and deliver it to the converter.

2.2.2. Controller and Converter blocks

A wide variety of MPPT controller schemes have been studied and implemented in the literature. The general principle behind these works considers an ON-OFF control over the PV cell voltage $v_{C_{IN}}(t)$ with a fixed hysteresis V_H according to:

$$V_{cont} = \begin{cases} ON, & \text{if } v_{C_{IN}}(t) > V_{MPP} + \frac{V_H}{2} \\ OFF, & \text{if } v_{C_{IN}}(t) < V_{MPP} - \frac{V_H}{2} \end{cases} \quad (2.1)$$

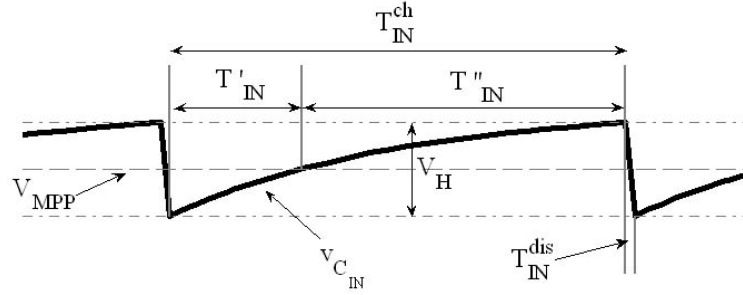
where V_{MPP} is the desired voltage value, i.e. the MPP voltage of the cell. V_{MPP} can be estimated by one of the well known methods proposed in literature ([29, 32, 34]).

The converter transfers energy from C_{IN} input capacitor to the UC. Moreover, the voltage level on C_{IN} swings around the estimated V_{MPP} voltage. An analysis on mean voltage values is carried out. We define the charging time T_{IN}^{ch} as the period of time during which C_{IN} is charged. On the other hand, the period of time during which the energy is transferred to the UC is the harvesting time T_{IN}^{dis} . Charging and harvesting times are cyclically repeated over a time period $T = T_{IN}^{ch} + T_{IN}^{dis}$ to perform the PV polarization at the estimated V_{MPP} voltage. An example of $v_{C_{IN}}$ dynamic evolution is represented in Fig. 2.2.

The controller parameter V_H affects the overall system efficiency as it will be detailed later, and therefore V_H will be tuned by the proposed design procedure.

2.2.3. C_{UC} and the WSn load

C_{UC} harvests energy from the input network and supplies the WSn. The main task of a sensor node is to detect events, perform quick local data processing, and then transmit the data. Power consumption can be divided into three domains: sensing, communication, and data processing. Sensing and data processing power varies with the nature of applications. However, usually, the most part of the power consumption of a sensor node is due to the transmission phase ([2]).


 Figure 2.2.: Time evolution of the controlled $v_{C_{IN}}$.

2.3. Harvesting control system analysis and efficiency evaluation

In this section the mathematical expression of the efficiency for a generic PV-based harvesting control system pictured in Fig. 2.1 is derived. The mean theoretical efficiency can be defined as:

$$\bar{\eta} = \frac{\bar{P}_{UC}}{\bar{P}_{MPP}} \quad (2.2)$$

where \bar{P}_{UC} is the mean power delivered to the UC and \bar{P}_{MPP} is the mean available power at the PV cell. In (2.2) we refer to theoretical mean efficiency because the mean power terms is computed according to $\bar{P} = \frac{1}{\tau} \int_{\tau} i(t) \cdot v(t) dt$ where $i(t)$ and $v(t)$ are the instantaneous current and voltage values and τ is the time duration over which the mean value is evaluated. In counterpart, with $\bar{\eta}_{me}$ we indicate the experimental mean efficiency that is the ratio between the measured value of \bar{P}_{UC} and \bar{P}_{MPP} . $\bar{\eta}_{me}$ will be measured on the MPPT system prototype once that the design procedure has been completed. $\bar{\eta}$ in (2.2) can be expressed as: $\bar{\eta} = \bar{\eta}_{AP} \cdot \bar{\eta}_{TP}$ where:

- $\bar{\eta}_{AP}$ (AP = Available Power) is the input system efficiency, i.e. the efficiency to transfer power from the PV to the input capacitor C_{IN} : it can be defined as $\bar{\eta}_{AP} = \frac{\bar{P}_{C_{IN}}}{\bar{P}_{MPP}}$, with $\bar{P}_{C_{IN}}$ being the input power to C_{IN} averaged over a time period $\tau = T_{IN}^{ch}$ managed during the charging period.
- $\bar{\eta}_{TP}$ (TP = Transferred Power) represents the converter stage efficiency, i.e. the percentage of energy transferred from C_{IN} to the UC. It is defined as follows: $\bar{\eta}_{TP} = \frac{\bar{P}_{UC}}{\bar{P}_{C_{IN}}}$, where the average is evaluated over a time period $\tau = T_{IN}^{dis}$.

2.3.1. $\bar{\eta}_{AP}$ evaluation

During the steady-state operations, the hysteresis control in (2.1) causes the $v_{C_{IN}}$ to be bounded around the V_{MPP} value. When $v_{C_{IN}}$ is below the threshold $V^- = V_{MPP} - \frac{V_H}{2}$, the controller turns

off the series switch and $v_{C_{IN}}$ increases due to the PV power. During T_{IN}^{ch} , C_{IN} is charged and $v_{C_{IN}}$ reaches the upper threshold $V^+ = V_{MPP} + \frac{V_H}{2}$. Then, the controller turns on the switch and the energy flows from C_{IN} to the UC (i.e. $v_{C_{IN}}$ decreases). After T_{IN}^{dis} , the turn-off condition is imposed and another cycle starts. From Fig. 2.2, the power transferred into C_{IN} during T_{IN}' and T_{IN}'' periods can be evaluated as:

$$\bar{P}'_{C_{IN}} = \frac{1}{T_{IN}'} \int_{T_{IN}'} i_{C_{IN}}(t) \cdot v_{C_{IN}}(t) dt \quad ; \quad \bar{P}''_{C_{IN}} = \frac{1}{T_{IN}''} \int_{T_{IN}''} i_{C_{IN}}(t) \cdot v_{C_{IN}}(t) dt$$

and:

$$\bar{P}_{C_{IN}} = \frac{T_{IN}' \cdot \bar{P}'_{C_{IN}} + T_{IN}'' \cdot \bar{P}''_{C_{IN}}}{T_{IN}' + T_{IN}''} \quad (2.3)$$

In order to find the theoretical formulation for T_{IN}' , T_{IN}'' , $\bar{P}'_{C_{IN}}$ and $\bar{P}''_{C_{IN}}$, the characteristic equation of the input capacitor C_{IN} is considered:

$$\bar{P}'_{C_{IN}} = \frac{1}{T_{IN}'} \int_{T_{IN}'} C_{IN} \cdot \frac{dv_{C_{IN}}}{dt}(t) \cdot v_{C_{IN}}(t) dt = \frac{C_{IN} \cdot V_H}{2T_{IN}'} \cdot \left(V_{MPP} - \frac{V_H}{4} \right)$$

Following the same calculation, it can be found that:

$$\bar{P}''_{C_{IN}} = \frac{C_{IN} \cdot V_H}{2T_{IN}''} \cdot \left(V_{MPP} + \frac{V_H}{4} \right)$$

By substituting $\bar{P}'_{C_{IN}}$ and $\bar{P}''_{C_{IN}}$ in (2.3) it results:

$$\bar{P}_{C_{IN}} = \frac{C_{IN} \cdot V_H \cdot V_{MPP}}{T_{IN}' + T_{IN}''} = \frac{C_{IN} \cdot V_H \cdot V_{MPP}}{T_{IN}^{ch}} \quad (2.4)$$

where $T_{IN}^{ch} = T_{IN}' + T_{IN}''$. T_{IN}' and T_{IN}'' can be evaluated by the following equations:

$$T_{IN}' = \int_{V_{MPP} - \frac{V_H}{2}}^{V_{MPP}} \frac{C_{IN}}{i_{C_{IN}}(v_{C_{IN}})} dv_{C_{IN}} \quad ; \quad T_{IN}'' = \int_{V_{MPP}}^{V_{MPP} + \frac{V_H}{2}} \frac{C_{IN}}{i_{C_{IN}}(v_{C_{IN}})} dv_{C_{IN}} \quad (2.5)$$

To evaluate T_{IN}' (and T_{IN}'') we refer to the ideal PV cell characteristic:

$$i_{C_{IN}}(v_{C_{IN}}) = I_{PV} - I_O \cdot e^{\frac{v_{C_{IN}}}{n_t \cdot V_t}}$$

where: 1) I_{PV} is the photo-generated current usually related to I_{MPP} by $I_{MPP} = \sigma_I \cdot I_{PV}$, (σ_I is an almost constant, positive value [34]); 2) I_O is the reverse saturation current; 3) V_t is the thermal voltage; 4) n_t is the junction unideal factor. In our calculation, we use the ideal PV model in the following of this paper, although a faithful PV cell model formulation can be considered ([37]). The considered MPPT method constrains the PV cell voltage to assume values in a short interval

around the V_{MPP} value. By assuming that $f(v_{CIN}) = \frac{1}{i_{CIN}(v_{CIN})}$ can be approximated by its second order Taylor polynomial, it can be shown that:

$$T'_{IN} = \frac{C_{IN} \cdot V_H}{2I_{MPP}} \left[1 - \left(\frac{1 - \sigma_I}{\sigma_I} \right) \frac{V_H}{4n_t V_t} + \sigma \frac{V_H^2}{24n_t^2 V_t^2} \right]$$

$$T''_{IN} = \frac{C_{IN} \cdot V_H}{2I_{MPP}} \left[1 + \left(\frac{1 - \sigma_I}{\sigma_I} \right) \frac{V_H}{4n_t V_t} + \sigma \frac{V_H^2}{24n_t^2 V_t^2} \right]$$

The charging time, T_{IN}^{ch} , can be computed as:

$$T_{IN}^{ch} = T'_{IN} + T''_{IN} = \frac{C_{IN} \cdot V_H}{I_{MPP}} \left[1 + \sigma \frac{V_H^2}{24n_t^2 V_t^2} \right] \quad (2.6)$$

Intermediate calculation are reported in Appendix A, for the sake of presentation. Finally, $\bar{\eta}_{AP}$ results in:

$$\bar{\eta}_{AP} = \frac{1}{1 + \sigma \frac{V_H^2}{24n_t^2 V_t^2}} \quad (2.7)$$

Notice that $\bar{\eta}_{AP}$ is strongly related to the PV cell parameters and V_H .

2.3.2. $\bar{\eta}_{TP}$ evaluation

The $\bar{\eta}_{TP}$ mean efficiency is defined as $\bar{\eta}_{TP} = \frac{\bar{P}_{UC}}{\bar{P}_{CIN}}$. In order to combine the system losses components we define:

- \bar{P}_{cnv} and \hat{P}_{cnv} the mean and the maximum converter power losses, respectively.
- \bar{P}_{cnt} and \hat{P}_{cnt} the mean and the maximum controller power losses, respectively.

Then, the $\bar{\eta}_{TP}$ mean efficiency is:

$$\bar{\eta}_{TP} = \frac{\bar{P}_{CIN} - \bar{P}_{cnv} - \bar{P}_{cnt}}{\bar{P}_{CIN}} \quad (2.8)$$

\bar{P}_{cnv} depends not only on the converter implementation but also on both the level of solar irradiation and the level of UC charge. \bar{P}_{cnt} is considered as a given value depending only on technological controller implementation.

2.3.3. $\bar{\eta}$ evaluation

The overall mean efficiency is derived as:

$$\begin{aligned}\bar{\eta} &= \frac{\bar{P}_{CIN} - \bar{P}_{cnv} - \bar{P}_{cnt}}{\bar{P}_{MPP}} = \bar{\eta}_{AP} - \frac{\bar{P}_{cnv} + \bar{P}_{cnt}}{\bar{P}_{MPP}} \\ &= \frac{1}{1 + \sigma \frac{V_H^2}{24n_t^2 \cdot V_t^2}} - \frac{\bar{P}_{cnv} + \bar{P}_{cnt}}{\bar{P}_{MPP}}\end{aligned}\quad (2.9)$$

Notice that $\bar{\eta}$ presents a minimum value, namely η_{MIN} , if \hat{P}_{cnv} and \hat{P}_{cnt} are considered in place of \bar{P}_{cnv} and \bar{P}_{cnt} in (2.9). Analytically,

$$\eta_{MIN} = \bar{\eta}_{AP} - \frac{\hat{P}_{cnv} + \hat{P}_{cnt}}{\bar{P}_{MPP}} = \frac{1}{1 + \sigma \frac{V_H^2}{24n_t^2 \cdot V_t^2}} - \frac{\hat{P}_{cnv} + \hat{P}_{cnt}}{\bar{P}_{MPP}}\quad (2.10)$$

and it results: $\eta_{MIN} \leq \bar{\eta} \leq 1$.

2.4. System design methodology

In this section, a system design procedure to cope with the application requirements is proposed. Firstly, a WSn power consumption model is considered. Then, the performance requirements and the operative constraints are analytically formulated. Finally, a system of inequalities is given to be numerically solved for the design purpose.

2.4.1. WSn power consumption model

We model the WSn power consumption behaviour by a current square waveform I_L at a constant voltage value V_L . During the sensing and data processing mode, $I_L = I_{min}$, whereas during the active mode (transmitting, receiving or synchronizing), $I_L = I_{max}$, being $I_{min} < I_{max}$. Accordingly, the mean power \bar{P}_L can be expressed by ([15, 26]):

$$\bar{P}_L = V_L I_L = V_L \cdot (I_{max} - I_{min}) \cdot \frac{T_{ON}}{T_L} + V_L \cdot I_{min} = V_L \cdot \left[I_{min} \cdot (1 - \delta) + I_{max} \cdot \delta \right]\quad (2.11)$$

where:

- I_{max} is the maximum peak current absorbed during wireless transmission and measurement;
- I_{min} is the minimal current absorbed in sleeping mode;
- V_L is the supply voltage of the sensor node;

- T_{ON} represents the 'active' time for the node;
- T_L is the sum of the 'active' and 'sleep' times;
- $\delta = \frac{T_{ON}}{T_L}$ is the duty-cycle of the WSn activity.

The power request \bar{P}_L and $V_L, I_{max}, I_{min}, T_L, \delta$ values depend on the specific WSn in use.

2.4.2. System performance

The first required performance is the supply autonomy. Specifically, it has to be guaranteed that the energy stored in the UC during T_{light} (the expected period in which the PV is able to charge the UC) is sufficient to cope with the WSn load requirement during the period T_{dark} (the expected period in which the PV cell is not able to charge the UC). During T_{dark} the UC is the only energy source able to supply the WSn load which requires an amount of energy: $\Delta E_{UC}^{dark} = \bar{P}_L \cdot T_{dark}$. On the other hand, during T_{light} the overall provided mean energy is $\Delta E_{PV} = T_{light} \cdot \bar{\eta} \cdot \bar{P}_{MPP}$. Let $\Delta E_L = T_{light} \cdot \bar{P}_L$ be the energy required by the WSn load during T_{light} , the design of the proposed scheme has to satisfy the following energy balance condition:

$$\Delta E_{PV} - \Delta E_L \geq \Delta E_{UC}^{dark} \implies T_{light} \cdot \bar{\eta} \cdot \bar{P}_{MPP} - T_{light} \cdot \bar{P}_L \geq \bar{P}_L \cdot T_{dark} \quad (2.12)$$

The additional requirement is in terms of system efficiency. Let η be the required minimum value of the system efficiency, it needs to guarantee that $\bar{\eta} \geq \eta$. To this aim, it is sufficient to assess $\eta_{MIN} \geq \eta$, being $\bar{\eta} \geq \eta_{MIN}$.

2.4.3. Constraints on the UC

In order to guarantee the UC's linear behaviour, it is a good practice to set the minimum UC voltage $V_{UC}^{min} = \frac{1}{2} V_{UC}^{max}$, being V_{UC}^{max} the maximum value of UC voltage ([30]) and $V_{UC}^{min} > \frac{1}{2} V_{UC}^{max}$. Besides, the choice of the UC takes into account both T_{light} and T_{dark} in this way:

- 1) The period of time spent to recharge the UC device must be lower than T_{light} ;
- 2) The energy harvested must be sufficient to supply both the WSn and the MPPT controller during the period T_{dark} .

The size of the UC can be derived according to the following inequality ([30]):

$$C_{UC} \geq C_{UC} \Bigg|_{MIN} = \frac{2 \cdot \Delta E_{UC}^{dark}}{\Delta V_{UC}^2} \quad (2.13)$$

with: $\Delta V_{UC}^2 = (V_{UC}^{max})^2 - (V_{UC}^{min})^2$.

The design of V_{UC}^{min} and V_{UC}^{max} derives by the constraints of the system logic. Specifically, V_{UC}^{max} may ensure that the series switch is properly polarized under any operative irradiations and UC conditions, namely: $V_{UC}^{max} \leq V_{MPP}^{min} - V_{C_{DROP}}^{min}$, being V_{MPP}^{min} the photovoltaic MPP voltage at minimal irradiation and $V_{C_{DROP}}^{min}$ the minimum allowed voltage drop upon the series switch. Finally, it needs to guarantee the minimum supply voltage for the load, namely $V_{UC}^{min} \geq V_L^{min}$.

2.4.4. Design conditions

The design conditions can be summarized as:

$$\begin{cases} \eta_{MIN}(C_{IN}, L, V_H) \geq \eta \\ T_{light} \cdot \eta_{MIN} \cdot \bar{P}_{MPP} - T_{light} \cdot \bar{P}_L \geq T_{dark} \cdot \bar{P}_L \end{cases} \quad (2.14)$$

subject to the constraints:

$$\begin{cases} C_{UC} > C_{UC} \Big|_{MIN} = \frac{2 \cdot \Delta E_{UC}^{dark}}{(V_{UC}^{max})^2 - (V_{UC}^{min})^2} \\ V_{UC}^{min} \geq V_L^{min} \\ V_{UC}^{max} \leq V_{MPP}^{min} - V_{C_{DROP}}^{min} \end{cases} \quad (2.15)$$

The equations in (2.14) and (2.15) depend on:

- a) PV cell parameters: $\sigma_I, n_t, V_t, V_{MPP}, \bar{P}_{MPP}$;
- b) UC parameters: $C_{UC}, V_{UC}^{min}, V_{UC}^{max}$;
- c) converter parameters: $V_{C_{DROP}}^{min}, \hat{P}_{cnt}, \hat{P}_{cnv}, C_{IN}, L$;
- d) controller parameter: V_H .
- e) load specifications: $I_{min}, I_{max}, V_L, T_L, \delta$;
- f) system performance: $T_{light}, T_{dark}, \eta$;

Notably, the mathematical system (2.14) is as more general as possible and many different design procedures can be carried out according to specific requirements. Indeed, some parameters of one or more of the sets a)-f) may be fixed (e.g. for economic or stock constraint purposes), and the design procedure is used to tune the other parameters in order to satisfy the desired system performance.

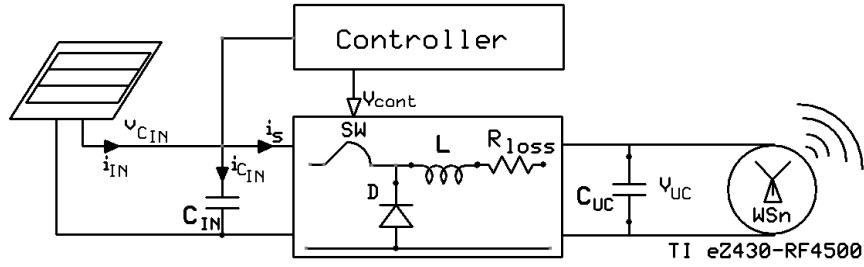


Figure 2.3.: The solar harvesting control system scheme considered for the design example.

2.5. An example of design procedure

Herein, we provide an example of the application of the proposed approach to design a low cost PV-based harvesting control system (Fig. 2.3) composed of a PV source, a step-down converter and UC storage device. The harvesting system is aimed to supply an off-the-shelf Texas Instruments *eZ430 – RF4500* mote that is a WSn with high integration and ultra-low-power 16-MHz MSP430 MCU consumption. The mote measures local temperature once per minute and then enters in a low-power mode to reduce the battery usage. According to the model provided in (2.11), the mote power consumption model parameters are summarized in Table 2.1. For more details on *TI eZ430 – RF4500*, the reader may refer to the related datasheet ([38]).

In the prototyped system, the MPPT operation performs the following two steps: 1) an estimation phase and 2) a seek phase. During the first step, estimation of the MPPT is carried out, whereas during the second phase the controller polarizes the PV to work on the estimated MPP ([39, 40]). For low power applications, it is fairly accepted in literature the use of the Fractional Open Circuit Voltage (FOCV) method ([32, 34, 41]) as an MPP tracking algorithm. The FOCV method estimates the maximum power point voltage V_{MPP} of the PV cell by means of the linear relation: $V_{MPP} = \sigma_V \cdot V_{OC}$, being V_{OC} the PV open-circuit voltage and σ_V a constant positive coefficient, related to the specific PV cell and experimentally ranged in $[0.7, 0.8]$ ([34]). Although σ_V is not exactly constant with the solar power irradiation, the FOCV method merges a good MPP tracking efficiency and a low power consumption performance. The periodic evaluation of V_{MPP} is carried out in hardware by a timer and an S&H blocks. Details about the controller implementation are reported in Appendix B.

In the following, we show an example of application to system in Fig. 2.3 of the design procedure described in Sec. 2.4 in order to select:

- a) PV cell (V_{MPP}, \bar{P}_{MPP}),
- b) UC device ($C_{UC}, V_{UC}^{min}, V_{UC}^{max}$),

I_{min}	I_{max}	V_L	T_L	δ
1.9mA	2.2mA	3.3V	60sec	0.3

Table 2.1: *TI eZ430 – RF4500*
Consumption model parameters.

T_{dark}	T_{light}	η
12 h	12 h	0.7

Table 2.2:
Application requirements

σ_V	σ_I	n_t	V_t	$V_{C_{DROP}}^{min}$	$ I_{C_{IN}}^{max} $	\bar{P}_{cnt}	R_{loss}
0.76	0.8	15	25 mV	1V	1A	1mW	200 $\mu\Omega$

Table 2.3: Given parameter values for the system in Fig. 2.3

and to design:

- c) converter parameters (C_{IN}, L),
- d) controller parameter (V_H),

We consider the following design data: a) *TI eZ430 – RF4500* supply specifications (Table 2.1), b) application requirements (Table 2.2), c) given parameter data in the problem formulation (Table 2.3). The design procedure is carried out according to the system of inequalities provided in (2.14)-(2.15). In order to achieve this aim, in the following section the overall system efficiency $\eta_{MIN}(C_{IN}, L, V_H)$, generically formulated in (2.10) and required by (2.14), is particularised with respect to the topology in Fig. 2.3.

2.5.1. Design condition formulation

In the provided formulation, we find out that η_{MIN} depends also on the loss terms (i.e. \bar{P}_{cnv} and \bar{P}_{cnt}) and, therefore, in the following we will derive \bar{P}_{cnv} and \bar{P}_{cnt} . As already noted, because the controller supply depends on the adopted technology implementation (with discrete or integrated components), \bar{P}_{cnt} may be considered constant and equal to the power consumption available on datasheets or directly measured on controller circuit implementation. On the other hand, \bar{P}_{cnv} depends not only on the topological implementation of the converter, but also on both environmental conditions (i.e. solar irradiation) and the level of UC charge. As an example of application, we estimate the \bar{P}_{cnv} contribution under the worst case scenario (that gives \hat{P}_{cnt} value), by studying the specific MPPT circuit implementation depicted in Fig. 2.3, where R_{loss} represents the overall loss resistance due to parasitics of the adopted converter elements. In order to find the analytical expression of the \bar{P}_{cnv} for the considered circuit in Fig. 2.3, we observe that $\bar{P}_{cnv} = \bar{P}_{sw} + \bar{P}_{loss}$, with \bar{P}_{loss} being the mean power loss due to the parasitic resistance R_{loss} in Fig. 2.3 and \bar{P}_{sw} the

mean switch power consumption. Additionally, $\bar{P}_{cnv} \leq \hat{P}_{sw} + \hat{P}_{loss}$, being \hat{P}_{sw} and \hat{P}_{loss} respectively the maximum switching and parasitic power losses.

In order to analytically formulate these loss terms, we preliminary evaluate the theoretical formulation of $v_{C_{IN}}(t)$, $i_s(t)$ and T_{IN}^{dis} . When the switch is ON it results $v_{C_{IN}}(0) = V_{MPP} + \frac{V_H}{2}$ by effect of hysteresis control. Let consider the mesh at the controller output. The input voltage evolution $v_{C_{IN}}(t)$ over time is ruled by both PV current I_{PV} and the discharging current by the switch. By setting up the system of equations for the mesh at the controller output and solving by $v_{C_{IN}}(t)$ it results:

$$v_{C_{IN}}(t) = e^{\alpha t} \left(\mathcal{A} \cos(\beta t) + \mathcal{B} \sin(\beta t) \right) + \mathcal{C}t + \mathcal{D} \quad (2.16)$$

with:

$$\begin{aligned} \alpha &= -\frac{R_{loss}}{2L}; \quad \beta = \sqrt{\frac{1}{L} \frac{C_{IN} + C_{UC}}{C_{IN} C_{UC}} - \frac{R_{loss}^2}{4L^2}} \\ \mathcal{A} &= \frac{C_{UC}}{C_{UC} + C_{IN}} \left(V_{MPP} + \frac{V_H}{2} - V_{UC}^0 - I_{PV} \cdot R_{loss} \frac{C_{UC}}{C_{UC} + C_{IN}} \right) \\ \mathcal{B} &= \frac{1}{\beta} \frac{C_{UC}}{C_{UC} + C_{IN}} \left(I_{PV} \frac{C_{IN} + C_{UC}}{C_{IN} \cdot C_{UC}} - I_{PV} \frac{R_{loss}^2}{2L} \frac{C_{UC}}{C_{UC} + C_{IN}} \right) - \frac{1}{\beta} \left(\frac{R_{loss}}{2L} \left(V_{MPP} + \frac{V_H}{2} - V_{UC}^0 \right) \right); \\ \mathcal{C} &= \frac{I_{PV}}{C_{IN} + C_{UC}}; \\ \mathcal{D} &= \frac{C_{IN}}{C_{UC} + C_{IN}} \left(V_{MPP} + \frac{V_H}{2} \right) + \frac{C_{UC}}{C_{UC} + C_{IN}} \left(V_{UC}^0 + I_{PV} \cdot R_{loss} \frac{C_{UC}}{C_{IN} + C_{UC}} \right) \end{aligned} \quad (2.17)$$

and $V_{UC}^0 = V_{UC}(T_{IN}^{dis})$. T_{IN}^{dis} can be found by positing:

$$T_{IN}^{dis} : v_{C_{IN}}(T_{IN}^{dis}) = V_{MPP} - \frac{V_H}{2} \quad (2.18)$$

Let evaluate the mean power loss contributions \bar{P}_{sw} and \bar{P}_{loss} . By assuming that the series switch is implemented by a bipolar transistor, \bar{P}_{sw} can be computed as ([42]):

$$\bar{P}_{sw} = \frac{1}{T} \int_0^T v_{CE}(t) \cdot i_s(t) dt + \frac{1}{T} \int_0^T v_{BE}(t) \cdot i_{BE}(t) dt \quad (2.19)$$

It can be stated that:

- the second term in (2.19) can be neglected ([42]),
- during the ON state, $v_{CE}(t) \leq V_{C_{DROP}}^{min}$ ([43]),

and, therefore:

$$\bar{P}_{sw} = \frac{1}{T} \int_0^{T_{IN}^{dis}} v_{CE}(t) \cdot i_s(t) dt \leq \frac{V_{CDROP}^{min}}{T} \int_0^{T_{IN}^{dis}} i_s(t) dt$$

that yields to:

$$\begin{aligned} \bar{P}_{sw} &\leq \frac{V_{CDROP}^{min}}{T} \int_0^{T_{IN}^{dis}} \left(I_{PV} - I_O \cdot e^{\frac{v_{CIN}(t)}{n_t \cdot V_t}} - i_{CIN}(t) \right) dt \leq V_{CDROP}^{min} \cdot I_{PV} \cdot \frac{T_{IN}^{dis}}{T} + C_{IN} \frac{V_{CDROP}^{min} \cdot V_H}{T} \\ &= \frac{V_{CDROP}^{min}}{T_{IN}^{dis} + T_{IN}^{ch}} \cdot \left(I_{PV} T_{IN}^{dis} + C_{IN} V_{CDROP}^{min} \cdot V_H \right) = \hat{P}_{sw} \end{aligned} \quad (2.20)$$

The second inequality is derived taking into account that $v_{CIN}(0) - v_{CIN}(T_{IN}^{dis}) = -V_H$. Finally, substituting the value of T_{IN}^{dis} in (2.20) we obtain the upper bound \hat{P}_{sw} so that $\bar{P}_{sw} \leq \hat{P}_{sw}$.

On the other hand, \bar{P}_{loss} is defined as:

$$\bar{P}_{loss} = \frac{R_{loss}}{T} \int_0^{T_{IN}^{dis}} i_s(t)^2 dt \quad (2.21)$$

\hat{P}_{loss} can be derived by (2.21) with the following analytical steps:

$$\begin{aligned} \bar{P}_{loss} &= \frac{R_{loss}}{T} \int_0^{T_{IN}^{dis}} \left(I_{PV} - I_O \cdot e^{\frac{v_{CIN}}{n_t \cdot V_t}} - i_{CIN}(t) \right)^2 dt \leq \frac{R_{loss}}{T} \int_0^{T_{IN}^{dis}} \left(I_{PV} + |I_{CIN}^{max}| \right)^2 dt \\ &\leq \frac{T_{IN}^{dis}}{T_{IN}^{dis} + T_{IN}^{ch}} \cdot R_{loss} \cdot \left(I_{PV} + |I_{CIN}^{max}| \right)^2 = \hat{P}_{loss} \end{aligned} \quad (2.22)$$

with $I_{CIN}^{max} = \max_{t \in [0, T_{IN}^{dis}]} i_{CIN}(t)$. By the analysis given above, we can define the converter maximum power consumption $\bar{P}_{cnv} = \hat{P}_{loss} + \hat{P}_{sw}$ such that $\bar{P}_{cnv} \leq \hat{P}_{cnv}$.

The efficiency (2.10) can be computed by the relations (2.4), (2.8), (2.20) and (2.21):

$$\begin{aligned} \eta_{MIN} &= \bar{\eta}_{AP} - \frac{\hat{P}_{loss}}{\bar{P}_{MPP}} - \frac{\hat{P}_{sw}}{\bar{P}_{MPP}} - \frac{\hat{P}_{cnt}}{\bar{P}_{MPP}} \\ &= \frac{1}{1 + \sigma \frac{V_H^2}{24n_t^2 \cdot V_t^2}} - \frac{V_{CDROP}^{min}}{T_{IN}^{dis} + T_{IN}^{ch}} \left(I_{PV} T_{IN}^{dis} + C_{IN} \cdot V_H \right) \frac{1}{\bar{P}_{MPP}} \\ &\quad - \frac{T_{IN}^{dis}}{T_{IN}^{dis} + T_{IN}^{ch}} \cdot R_{loss} \cdot \left(I_{PV} + |I_{CIN}^{max}| \right)^2 \frac{1}{\bar{P}_{MPP}} - \frac{\hat{P}_{cnt}}{\bar{P}_{MPP}} \end{aligned} \quad (2.23)$$

where T_{IN}^{ch} and T_{IN}^{dis} can be derived by equations (2.6) and (2.18), respectively. In what follows, we numerically solve the system inequalities (2.14)-(2.15) for the considered system, united with the expression of η_{MIN} of (2.23) and taking into account data given in Table 2.1 - 2.2 - 2.3 to select the PV cell, and the UC device and to design the system parameters C_{IN} , L , V_H .

2.5.2. Co-design procedure

Although the proposed design framework represents a dependent set of equations, it is solved by a recursive procedure that we enumerate hereafter:

Step1 Assign a value to \bar{P}_{MPP} such that: $\bar{P}_{MPP} \geq \frac{\bar{P}_L \cdot (T_{light} + T_{dark})}{\eta \cdot T_{light}}$, according to equation in (2.14);

Step2 Choose the UC parameters C_{UC} , V_{UC}^{max} and V_{UC}^{min} satisfying constraints, (2.15);

Step3 Tune the parameters C_{IN} , L and V_H , satisfying the first inequality of (2.14). If the condition cannot be fulfilled, turn back to the *Step1* and assign a new value for \bar{P}_{MPP} ;

The given procedure can guide the designer in the choice of the related hardware components. With the parameters given in Table 2.1 - 2.2 - 2.3, we obtain the design solution parameters:

- a) $V_{MPP} = 12V$, $\bar{P}_{MPP} = 1W$;
- b) $V_{UC}^{max} = 5.4V$, $V_{UC}^{min} = 3.5V$ and $C_{UC} = 60F$;
- c) $C_{IN} = 220\mu F$, $L = 20\mu H$;
- d) $V_H = 1V$;

achieving $\eta_{MIN} = 0.85 > \eta = 0.7$.

2.6. Experimental validation

A solar harvesting control system has been designed according to the procedure solution provided in the previous section. Details of the circuit topology and the main hardware components are reported in Appendix A and in Table A.1, respectively. The experimental set-up is reported in Fig. 2.4.(a) and the details of system components are depicted in Fig. 2.4.(b). Although the specific implementation is not the main aim of the manuscript, we emphasize that the final prototype is characterized by:

- a) low static power consumption of the controller, $\bar{P}_{cnt} \sim 330\mu W$,
- b) logic fully supplied by the UC, under all operative conditions, differently to most of similar works proposed in literature, where the controller logic is supplied by an additional battery ([31, 32]).

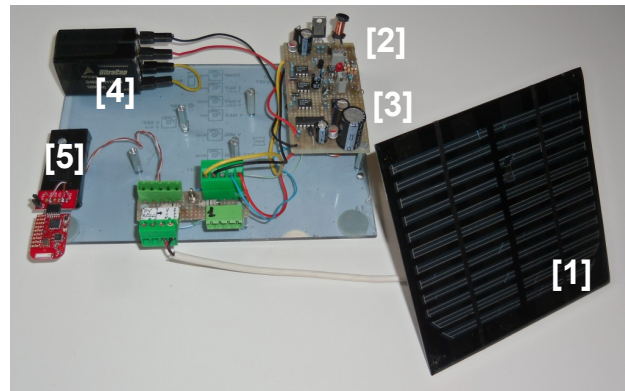
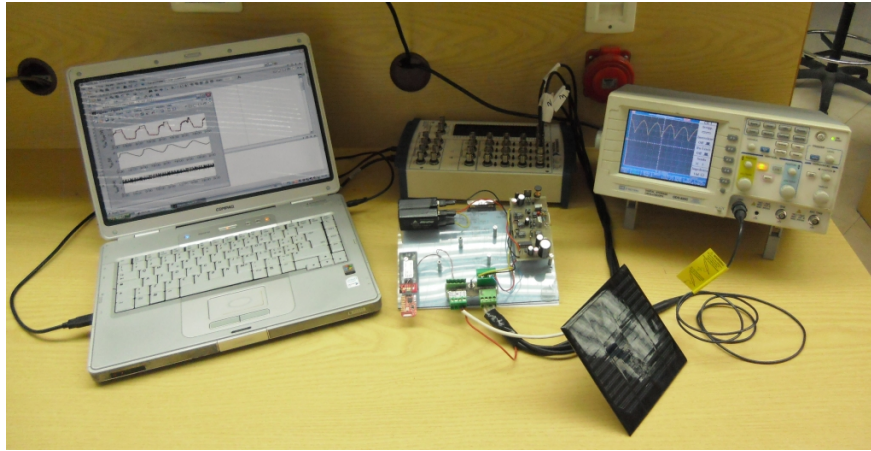


Figure 2.4.: (a) Experimental setup carried out in the validation section; (b) A detail of the prototyped Solar Harvesting Control System: [1] PV cell, [2] Converter, [3] Controller, [4] UC, [5] the supplied TI *eZ430 – RF4500* mote.

The prototyped PV-based harvesting system is then tested in a four days experiment. In Fig. 2.5 the time evolution of v_{CIN} (Fig. 2.5.(a)), V_{UC} (Fig. 2.5.(b)) and I_L (Fig. 2.5.(c)) are reported. During the light hours of the day, the PV source recharges the UC. During the night, the V_{UC} voltage decreases because the UC supplies the WSn load, while the PV open circuit voltage decreases to its minimal value. The solar harvesting system assures that the PV works at around its maximum power point (dashed line in Fig. 2.5.(a)). When the UC is fully charged (point [1] on the first day and other points in similar positions on the following days of this experimentation) the MPPT process is inhibited, resulting that $v_{CIN} > V_{MPP}$ (point [2] on the first day and similar positions on the following days). The MPPT operation starts again (point [3] and corresponding others) when UC operates out of its full-of-charge regime (point [4] and corresponding others) according to the constraint (2.15).

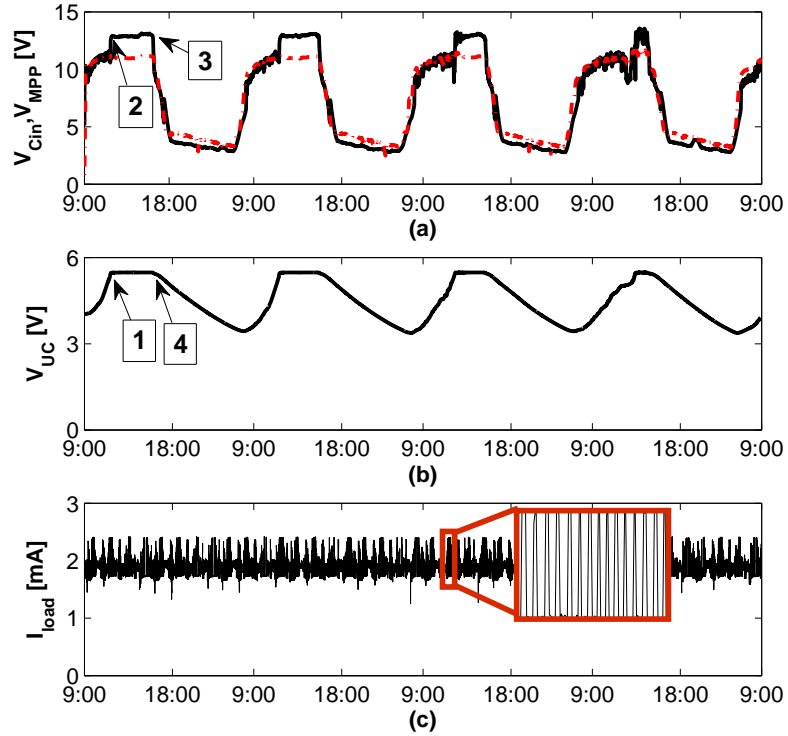


Figure 2.5.: Dynamic evolution of: (a) v_{CIN} (continuous line) and V_{MPP} (dashed line); (b) V_{UC} ; (c) I_L

The experimental results confirm the effectiveness of the proposed approach coping with the autonomy system requirement and efficiency. Finally, the measured overall system efficiency is $\bar{\eta}_{me} \sim 0.86$, that is in a good agreement with the required performance, being: $\bar{\eta}_{me} > \eta_{MIN} > \eta = 0.7$, where η is the desired performance efficiency.

2.7. Conclusion

In this chapter a design methodology of the PV-based harvesting control system components (i.e. PV cell, converter, controller and UC device) is provided to achieve the required level of efficiency and sensor node autonomy. An application example of the proposed approach is shown by carrying out the design of both the electronic PV-based harvesting control system components and the hysteresis controller parameter. The effectiveness of the proposed approach was experimentally validated by a prototype, that supplied an off-the-shelf Texas Instruments mote during a four days experiment. The test showed that the required performances were fulfilled in terms of system efficiency and autonomy. The method is general and it may be used to design a low cost solar

harvesting control system to potentially supply a wide range of consumer electronic off-the-shelf devices.

Co-design of Compressive Sensing methods

3.1. Introduction

RECENT technological innovations in wireless infrastructures and low power systems raise the market demand on low-cost Wireless Sensor Networks (WSNs) for industrial applications. WSNs are distributed measurement systems consisting of one elaboration node, or Fusion Centre (FC), and a large number of sensor units that capture information from the plant environment (Fig. 3.1). Here, the FC collects information for both monitoring and control purposes from all the deployed sensor nodes. Because of limited radio coverage of each transmitter, information from one node reaches the FC by defining minimum cost paths that involve other nodes of the network. Each node therefore works also as a router in order to transport the streams of data from all network nodes to the FC. We can distinguish two different centralized scenarios: monitoring or event trigger applications. When a network operates in the latter mode, each node emits own information only if a critical condition emerges from local measurements, while in monitoring mode, data are continuously acquired and sent during each quantum of time, denoted with ΔT in the following. An efficient energy management is a crucial component of wireless network design, since it can increase the network lifetime. This concept is meaningful for battery supplied devices ([44]) that do not have energy-harvesting capabilities and, hence, become inactive once their batteries run out of energy. Because an important part of energy demand is due to the radio-frequency (RF) activities, recent studies are focused on the reduction in managed data that in turn relax the traffic flows throughout the sensor nodes ([45]).

In typical WSN applications, on-board node sensors acquire signals of interest at the Nyquist rate. Without data processing, raw data are sent to FC that performs the data aggregation and extracts information of interest ([46]). In most recent years, with the increase of node computational capabilities, signal processing techniques have been widely adopted also in WSN infrastructures: in

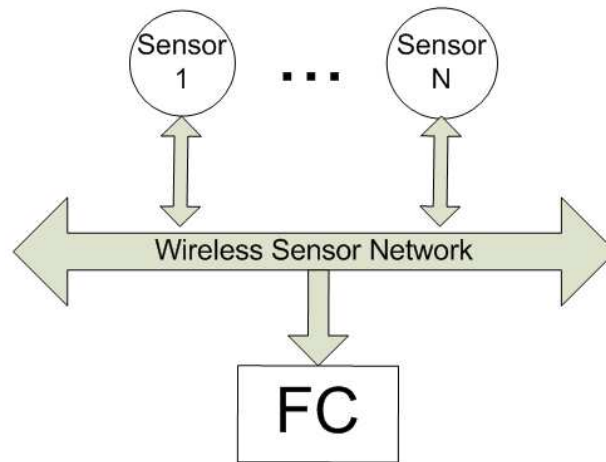


Figure 3.1.: Centralized-fusion WSN infrastructure.

this case, raw data are compressed and then sent. Although these techniques increase the elaboration power consumptions at the local node, they conversely reduce the RF activities and this is useful for both power consumption and traffic performance. Generally speaking, the idea behind standard signal processing methods is that the sampled signal is projected into a domain where a small number of coefficients contains the most part of signal information. Coefficient amplitudes and locations, that equivalently represents the signal in time domain, are then transmitted.

The recent discovers on the theory of Compressive Sensing (CS) ([47]) laid the foundations of efficiently compact sensed data in a small set of measurements. In [47] the CS applied on perfectly sparse signals is analytically studied. In [48, 49] CS compression and signal reconstruction error relationship has been investigated under the case of quasi-sparse and noisy measurements, respectively. It is proved that only perfectly sparse signals have exact reconstructions from their CS versions. Quasi-sparse and noise-affected signals can be reconstructed from their CS versions with a finite reconstruction error ([50]).

3.1.1. Related works

Recently, CS has found application in WSN monitoring systems to improve the network performance ([51, 52]). A CS framework can be easily applied for temporal ([53]) or spatial ([54]) monitored signals. The main advantage to use CS in WSN is to extend the network lifetime performance, because CS can hugely reduce the RF activity. The determination of the eligible set of measurements that ensures the recovery procedure to be acceptably reliable is, however, not trivial. Unfortunately, that choice strictly depends on the sparsity of the signal to be compressed and the only way to be exactly determined consists to periodically estimate it by some learning procedures.

However, such learning procedures typically involves a large amount of data to be processed and then they are energetically inefficient in WSN. Alternatively, in [53] authors describe an on-line procedure to dynamically set the amount of information without making use of any learning procedure. They show that it is possible to steer the CS reconstruction error by dynamically adjusting the number of average measurements provided by the network. The proposed scheme ensures the expected level of reconstruction error to be tracked.

Packet loss effect due to collisions is a well known drawback in WSN because it affects the power consumption and the reliability of the communication. A packet loss event is more frequent in intense data traffic communication. Specifically, if a WSN operates with a CS-based compression method, packet loss phenomena are in trade-off with the recovery error introduced by the CS-based method [55].

Although the above mentioned drawbacks interact one to each others and can significantly affect the WSN performances (autonomy, communication reliability and quality of recovered signal), these phenomena are typically analysed apart or pairwise in literature.

In [45] the authors propose an analysis of WSN autonomy performance under different compression approaches including the classic formulation of CS. To this aim, a node power consumption model as function of device computations and radio activities (receptions and transmissions) is provided. They characterize the power consumption of the network assuming different levels of: signal sparsity, network size and transmission ranges. The way they compute the CS recovery error is based on a theoretical formulation of the CS error instead of an on-line calculation. Additionally, in [56] the trade-off between energy and recovery error has been analysed more in details. The authors extend the analysis carried out in [45] by taking also into account the network performances as function of the data size. They base their analysis over a real WSN architecture and they evaluate the recovery error on-line.

Oppositely, few works investigate on the existing trade-off between CS recovery error and packet loss effects on WSN. In [55], authors formulate a random sampling CS scheme and they show evidence of the existing trade-off between the recovery error model and the packet loss probability in that scheme. Moreover, they provide a co-design procedure that is meant to minimize packet loss phenomenon and maximize the CS recovery reliability.

So far, many papers (e.g. [57, 58]) study the hardware/software co-design framework for a wireless sensor platform, which achieve to select network hardware/software configuration to optimize performances of the network. In particular, in [59] authors present a hardware/software co-design framework that adaptively tunes a reconfigurable wireless sensor platform in run-time in order to accomplish at many design requirements, such as the hardware acceleration (e.g. clock frequency and sleep inactivity), power consumption and network throughput. A similar analysis has been

addressed in [58]. Therein, the authors provide a co-design procedure to optimize the sampling accuracy and transport reliability of a WSN. They consider as optimization variable only the number of network sensor nodes, that in their formulation trade-off with the accuracy of the spatial sampling and the retransmissions.

3.1.2. Contributions and chapter outline

The main contributions of the present work are summarized. Firstly, we elaborate a WSN tool for the co-design of system parameters of the network in order to accomplish with given important network metrics such as network lifetime and signal error representation. Indeed, we formulate a network model composed by: a) an energy node consumption model (whose behaviour can be tuned on the base of the adopted compression algorithm) and b) a data traffic model (based on the concepts of data traffic and packet collision effect). Additionally, we adopt the provided co-design tool in order to explore the existing trade-off between energy autonomy and recovery performances in presence and in absence of packet loss phenomena, when a Compressive Sensing scheme is adopted to represent the transmitted data by the WSN. On the base of the shown co-design procedure, we are able to select the CS scheme (and related parameters) among some main representative schemes in literature in order to improve the theoretical system performances.

The rest of this chapter is organized as follows. The WSN co-design tool is widely presented in Sec. 3.2. Therein, we firstly formulate the WSN monitoring model and the performance metrics that we will consider in our co-design optimization. Then it follows the WSN co-design tool presentation and description. The provided WSN model is particularized in the case that a Compressive Sensing scheme is adopted to represent the environmental data. In Sec. 3.5.3 we provide an example of software co-design of CS-based monitoring WSN to select the combination of CS parameters in order to improve the network performances, previously presented. Conclusions are given in Sec. 3.6.

3.2. Network Model Formulation

In the following we will introduce the model of the overall monitoring architecture in Fig. 3.1 that supports the co-design procedure and the related performance evaluation for the considered compressive sensing algorithms. Firstly, In Sec. 3.2.1 we provide a mathematical description of the network layer. We additionally provide the formulation of the packet loss phenomenon. Secondly, in Sec. 3.2.2 the power consumption model is detailed.

Network parameter	meaning
D_P	Number of units of user data for each packet
B_P	number of bits contained into one packet
B_M	number of bits representing a unit of user data
$D_g^{(i)}$	number of user data generated by the i -th source node each ΔT
$D_r^{(i)}; D_t^{(i)}$	number of user data received or transmitted by node i node within a ΔT
$P_r^{(i)}; P_t^{(i)}$	number of packets received or transmitted by the i -th node within a ΔT .

Table 3.1.: Network and data flow symbols.

3.2.1. Node upstream

Let \mathcal{G} be a connected and undirected network graph composed of a set of n nodes. Let Ω define the vector of node weights $\Omega = [\omega^{(i)}], i = 1..n$.

Herein we assume that the source-destination path is computed according the Dijkstra's algorithm and that the i -th node input link weights are assigned to be equal to the node weight $\omega^{(i)}$.

For the sake of presentation we will introduce the following definition:

Definition 1. *The upstream tree $\mathcal{U}_\Omega^{(i)}$ of node i -th is the set of nodes so that the Dijkstra's path from such nodes to FC crosses the node i -th.*

Notice that the set $\mathcal{U}_\Omega^{(i)}$ depends on the Dijkstra's path and in turns on the set Ω .

In Computer Science a stream of 'user data' is quantized into atomic elements, or packets. In the monitoring applications, a unit of user data is a sensed measurement from environment that is numerically represented according to the considered compression approach. Let define \overline{D}_P as:

$$\overline{D}_P = \left\lfloor \frac{B_P}{B_M} \right\rfloor \tag{3.1}$$

where: B_P is the number of bits contained into one packet and B_M is the number of bits representing a unit of user data. $\lfloor \cdot \rfloor$ returns the higher integer number lower than its real argument (\cdot). \overline{D}_P represents the maximum number of units of user data that each packet can contain. Let D_P indicates the number of units of user data that the packet contains. D_P is a fraction of \overline{D}_P and may be expressed by the following relation:

$$D_P = \max \left\{ \lfloor \beta \overline{D}_P \rfloor, 1 \right\}$$

where $\beta \in (0, 1]$ is the filling factor of each packet. If $\beta = 1$ then the packet payload contains the highest number of user data it can contain.

Let $P_r^{(i)}$ ($P_t^{(i)}$) the number of received (resp. transmitted) packets by the i -th node within each ΔT . In order to analytically formulate $P_r^{(i)}$ and $P_t^{(i)}$, we preliminarily introduce:

1) $D_g^{(i)}$ the number of user data generated (i.e. acquired from environment and eventually elaborated) by the i -th source node for each ΔT . $D_g^{(i)} = n_Y^{(i)}$, being $n_Y^{(i)}$ the number of acquired samples of the i -th node.

2) $D_r^{(i)}$ the number of user data received by the i -th node during each ΔT . $D_r^{(i)}$ depends on both $\mathcal{U}_\Omega^{(i)}$ and the adopted compression. It can be formulated as:

$$D_r^{(i)} = \sum_{j \in \mathcal{U}_\Omega^{(i)}} D_g^{(j)} \quad (3.2)$$

3) $D_t^{(i)}$ the number of user data transmitted during each ΔT by node i . $D_t^{(i)}$ is an integer number and can be formulated as:

$$D_t^{(i)} = D_r^{(i)} + D_g^{(i)} \quad (3.3)$$

$P_r^{(i)}$ and $P_t^{(i)}$ are defined as:

$$P_r^{(i)} = \left\lceil \frac{D_r^{(i)}}{D_P} \right\rceil \quad P_t^{(i)} = \left\lceil \frac{D_t^{(i)}}{D_P} \right\rceil$$

where: $D_r^{(i)}$ ($D_t^{(i)}$) is the total number of received (transmitted) user data units within one ΔT and D_P is the number of user data units contained into the single packet. $\lceil \cdot \rceil$ denotes the lower integer number that is higher than its real argument (\cdot). Finally, considering (3.2) and (3.3) it follows:

$$P_r^{(i)} = \left\lceil \frac{D_r^{(i)}}{D_P} \right\rceil \quad P_t^{(i)} = \left\lceil \frac{D_r^{(i)} + D_g^{(i)}}{D_P} \right\rceil \quad (3.4)$$

The symbolism defined in this section is summarized in Table 3.1.

Packet loss model Packet collision in a random channel access scheme leads to loose information. A packet collision occurs if two or more packets overlaps in time at the FC receiver ([55]). Assuming a Poisson distribution for the average number of packets received to the FC, the probability of collision in a network is given by ([55]):

$$p_{col} = 1 - e^{-\frac{2 \cdot n_{pk} \cdot \Delta_{Tp}}{\Delta_{Tf} - \Delta_{Tp}}} \quad (3.5)$$

where: Δ_{Tp} denotes the time duration of the single packet, Δ_{Tf} the frame duration and n_{pk} is the amount of transmitted packets. Meanly speaking, p_{col} is zero if no packet has been sent within the actual frame, while it is even more near to one with m approaching to infinity.

3.2.2. Node energy model

Let assume that each sensor node is able to perform the following operations: a) AD (analogue to digital) converter acquires data from local environment, b) a low power processor elaborates information, c) a radio system transmits data over a network, d) a limited-energy battery supplies the whole system. In a network composed by n nodes, the overall energy spent by the i -th node during each z -th ΔT , $z \in \mathbb{N}$, will be indicated with $\Delta e_i^c(z)$ with $i \in [1, \dots, n]$. The apex c reminds to the reader that $\Delta e_i^c(z)$ depends also on the adopted compression and it will be differentiated among representative compression approaches described in Sec. 3.5. Defining with $e_i^c(z)$ the energy level of the i -th node with $i \in [1, \dots, n]$ at z -th ΔT , the dynamical model of the node can be formulated as:

$$e_i^c(z+1) = e_i^c(z) - \Delta e_i^c(z) \quad (3.6)$$

As in Karakus et al. ([45]), $\Delta e_i^c(z)$ is defined as: $\Delta e_i^c(z) = \phi_{OP}^{(i,c)} + \phi_{TRX}^{(i,c)}$ with:

- 1) $\phi_{OP}^{(i,c)}$ is the energy spent due to node operations and includes: the energy contributions of data acquisitions, $\phi_{ACQ}^{(i,c)}$, data elaborations, $\phi_{SP}^{(i,c)}$, and background operations, $\phi_{BCG}^{(i,c)}$, namely $\phi_{OP}^{(i,c)} = \phi_{ACQ}^{(i,c)} + \phi_{SP}^{(i,c)} + \phi_{BCG}^{(i,c)}$.
- 2) $\phi_{TRX}^{(i,c)}$ is the energy required by the node for both radio transmission $\phi_{TX}^{(i,c)}$ and reception $\phi_{RX}^{(i,c)}$ energy requirements according to: $\phi_{TRX}^{(i,c)} = \phi_{TX}^{(i,c)} + \phi_{RX}^{(i,c)}$.

By combining the given relations, it results:

$$\Delta e_i^c(z) = \phi_{OP}^{(i,c)} + \phi_{TRX}^{(i,c)} = \left(\phi_{ACQ}^{(i,c)} + \phi_{SP}^{(i,c)} + \phi_{BCG}^{(i,c)} \right) + \left(\phi_{TX}^{(i,c)} + \phi_{RX}^{(i,c)} \right) \quad (3.7)$$

Notice that $\phi_{OP}^{(i,c)}$ is function of compression adopted by the node, $\phi_{TRX}^{(i,c)}$ depends on both data traffic associated to the i -th node and data compression characteristics. Moreover, $\phi_{ACQ}^{(i,c)}$, $\phi_{SP}^{(i,c)}$, $\phi_{BCG}^{(i,c)}$, $\phi_{OP}^{(i,c)}$ depend on the adopted data compression method. The adopted definitions and the respective values have been reported in Table 3.2.

Finally, both $\phi_{RX}^{(i,c)}$ and $\phi_{TX}^{(i,c)}$ contributions take into account the node transmission activity by mean of $P_r^{(i)}$ and $P_t^{(i)}$ (equation (3.4)) and it results:

$$\begin{aligned} \phi_{RX}^{(i,c)} &= P_r^{(i)} \cdot \phi_{RX}^0 \\ \phi_{TX}^{(i,c)} &= P_t^{(i)} \cdot \phi_{TX}^0 \\ \phi_{TRX}^{(i,c)} &= \phi_{RX}^{(i,c)} + \phi_{TX}^{(i,c)} \end{aligned} \quad (3.8)$$

being ϕ_{RX}^0 and ϕ_{TX}^0 the unit energy coefficients for one transmitted or received packet, respectively (see also Table 3.2).

Unit energy parameter	Parameter meaning	Parameter unit
ϕ_{ACQ}^0	ADC mean required energy over one acquisition	2.1 nJ [Joule/acq.]
$\phi_{MRD}^0, \phi_{MWR}^0$	mean required energy over one bit memory read and write	0.26nJ , 4.3nJ [Joule/bit]
$\phi_{ADD}^0, \phi_{MUL}^0$	mean required energy over one bit addition and multiplication	3.3nJ , 9.9nJ [Joule/bit]
$\phi_{CMP}^0, \phi_{SFT}^0$	mean required energy over one bit comparison and shift operation	3.3nJ , 3.3nJ [Joule/bit]
ϕ_{BCG}^0	mean required energy in the unit of CPU operation	1.44nJ [Joule/Op]
ϕ_{RX}^0	mean required energy for received data over one packet PK	0.93mJ [Joule/PK]
ϕ_{TX}^0	required energy for transmitted data over one packet, PK .	[Joule/PK]

Table 3.2.: Unit energy coefficients for the given energy-based node model.

3.3. Performance metrics

In the following, we will define the metrics that will be considered in the performance evaluation and co-design procedure.

3.3.1. T_l metric

The node lifetime $\tau^{(i)}$ is defined as the number of ΔT that are needed to deplete the i -th node battery from the initial energy level, $e_i^c(0)$, to a threshold minimum level, namely E_{TH} , with $e_i^c(0) > E_{TH}$. From (3.6), it can be derived that:

$$e_i^c(z+1) = e_i^c(0) - \sum_{u=1}^z \Delta e_i^c(u) = e_i^c(0) - \sum_{u=1}^z \left(\phi_{OP}^{(i,c)} + \phi_{TRX}^{(i,c)} \right)$$

Then, we define the i -th node lifetime $\tau^{(i)}$ as:

$$\tau^{(i)} = \min_{z \in \mathbb{N}} : e_i^c(z+1) < E_{TH}$$

The Network Lifetime T_l is formulated as the lifetime of the node in the network that faults earlier than the others during time, namely: $T_l = \min_{i \in [1, \dots, n]} \{ \tau^{(i)} \}$.

3.3.2. Reconstruction error metrics: $MSE^{(m)}$, $MSE^{(n_Y|o)}$

Let $\mathbf{X}^{(n_Y)^*}$ be the recovered signal by a given set of n_Y measurements. The theoretical normalized L_2 -norm error $MSE^{(n_Y)}$ is defined as:

$$MSE^{(n_Y)} = \frac{\|\mathbf{X} - \mathbf{X}^{(n_Y)^*}\|_{L_2}}{\|\mathbf{X}\|_{L_2}}$$

$MSE^{(n_Y)}$ considers the sampled signal \mathbf{X} as reference to evaluate the normalized error. Although $MSE^{(n_Y)}$ represents the effective error between the recovered copy and the original signal, it is not suitable to be evaluated, as it requires the perfect knowledge of \mathbf{X} . More suitable in [53] a different metric, namely $MSE^{(n_Y|o)}$, has been considered in place of $MSE^{(n_Y)}$, that allows the on-line estimation for the recovery error. This is defined as:

$$MSE^{(n_Y|o)} = \frac{\|\mathbf{X}^{(o)} - \mathbf{X}^{(n_Y)^*}\|_{L_2}}{\|\mathbf{X}^{(o)}\|_{L_2}}$$

where now the reference is the subset $\mathbf{X}^{(o)} \in \mathbf{X}$. The choice of o trades off between power consumption and reliability of recovery estimation. Indeed, even though $o \rightarrow n_X$, $MSE^{(n_Y|o)} \rightarrow MSE^{(n_Y)}$.

3.4. WSN co-design tool

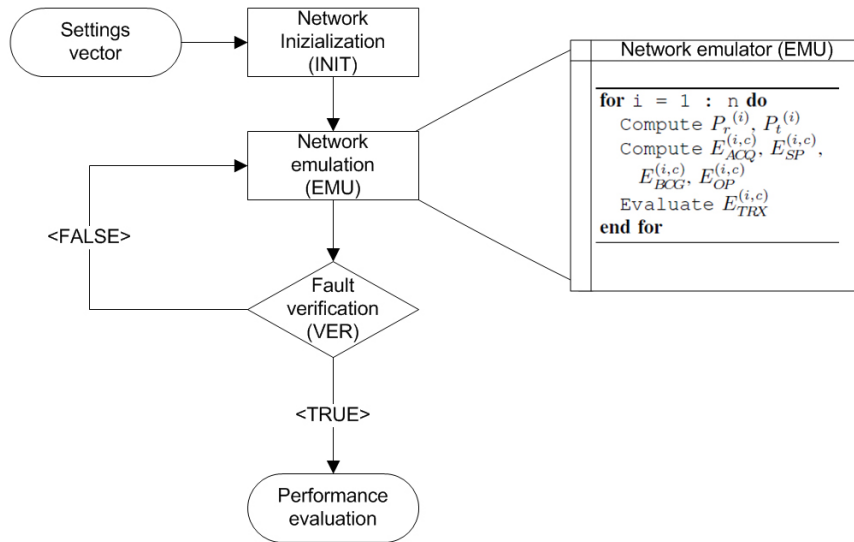


Figure 3.2.: The adopted WSN simulator tool.

We implement the proposed network model in MATLAB environment. The scheme of our simulation is reported in Fig. 3.2. The simulator sets up the network by loading the user defined input

settings (*settings vector* in figure) and then the network is simulated in discrete time. Node energy levels update according to (3.6). When at least one node depletes its battery, the simulation ends and the network performance are evaluated. Specifically, the Network simulator is composed by 3 steps: network initialization (INIT), network emulation step (EMU) and fault verification (VER). Simulation follows the block scheme in Fig. 3.2: after the initialization (INIT) and the network is emulated (EMU) for one ΔT . The fault verification over nodes (VER) is then evaluated. If VER returns "FALSE" another ΔT simulation starts: EMU and VER steps are cyclically repeated until at least one fault occurs. In that case, VER step returns "TRUE" and then the performance metrics are returned.

INIT step The network initialization step creates the network nodes and initializes them with the network model parameters, given by the settings vector. Specifically, according to the provided network model, it is made by:

- *node energy parameters*: $\{e_i^c(0)\}_{i \in [1, \dots, n]}$, E_{TH} ,
- *network parameters*: n , \mathbf{A} , β ,
- *application parameters*: B_M , o .

It moreover in this vector the values of $\phi_{ACQ}^{(i,c)}$, $\phi_{SP}^{(i,c)}$, $\phi_{BCG}^{(i,c)}$, $\phi_{OP}^{(i,c)}$ have been assigned according to the specific compression scheme adopted by the network to represents its data.

During the INIT step the following operations are performed:

- 1) n virtual nodes are generated. Their energy-based models are initialized to the compression approach defined by the user. Then Data compression and Node energy parameters are set.
- 2) By making use of given adjacency matrix \mathbf{A} , $\mathcal{U}_\Omega^{(i)} \forall i \in [1, \dots, n]$ is computed by following the definition given in Sec. (3.2). $\mathcal{U}_\Omega^{(i)}$ are then assigned to the respective nodes.
- 3) B_M and β parameters are assigned to each node.

EMU step In this step, the network is emulated for one ΔT : node activities are simulated cyclically. For each node, are computed:

- a) $P_r^{(i)}$ and $P_t^{(i)}$ by equations in (3.4),
- b) $\phi_{TRX}^{(i,c)}$ energy transmission contribution given in (3.8),
- c) $\phi_{OP}^{(i,c)}$ operative required energy as function of compression approach,

d) $\Delta e_i^c(z)$ by equation in (3.7).

Finally, $\Delta e_i^c(z)$ value is used to update the node energy level by using (3.6).

VER step In this step, the $\{e_i^c(z)\}_{i \in [1, \dots, n]}$ are scanned and are compared with the given threshold E_{TH} in order to detect at least one node fault. This step returns 'TRUE' or 'FALSE' according to:

$$\begin{cases} \text{TRUE} & \exists i \in [1, \dots, n] \mid e_i^c(z) \leq E_{TH} \\ \text{FALSE} & \text{otherwise} \end{cases}$$

being z the current simulation ΔT . If VER step returns 'FALSE', the ΔT counter is updated.

In the network parameters in *settings vector* are exhaustively swept within their ranges, we can obtain the corresponding values of the system performances. Therefore, we can use the proposed WSN simulator tool in order to find the set of parameters that allows the network performances to stand into some desired ranges. In this sense, the WSN simulator tool can be used to aid the design of a WSN monitoring system.

3.5. Case Studio: Compressive Sensing co-design

In this section, we introduce the reader to the main concepts on Compressive Sensing and we describe the different implementations of CS on WSN presented in literature.

Therefore, we provide an example of software co-design of a WSN aimed at the choice of which CS scheme to adopt (cCS, rsCS or aCS) over a representative EH-WSN in order to obtain certain given lifetime and recovery performances fixed by the application.

3.5.1. Compressive Sensing Modelling

In lack of energy constraints, the acquired raw data can be directly packed and sent to the FC. In this case, no compression operations are performed over raw data. In this case, sampled data may respect the Shannon principle.

Classically, signal compression method ([60]) relies on finding a basis (e.g. Discrete Cosine Transform (DCT), wavelets or Haar wavelet) that provides sparse signal representation. We say that a signal is sparse when its information spreads onto a limited number of basis components. Time domain data vector is then represented in a different domain.

Most recent Compressive Sensing (CS) theory ([47]) proposes a novel signal acquisition and recovery methods. This technique enables large reduction of sampling data when the signal is sparse.

Let $X(t)$ be an analogue signal of time duration T and $\mathbf{X} \subset \mathbb{R}^{n_X}$ its digital version of n_X samples with a sampling frequency f_s (f_s is chosen according to the Shannon's theorem) with $n_X = f_s \cdot T$.

Under the transform coding approach, compression operates on \mathbf{X} to produce $\mathbf{S} = \Theta_{TC}\mathbf{X}$ that is the projection of the sampled data in a certain domain with orthogonal matrix Θ_{TC} , being $\Theta_{TC} \subset \mathbb{R}^{n_X \times n_X}$. Let assume that \mathbf{X} is n_S -sparse in that domain. It means that n_S coefficients in \mathbf{S} are different by zero and the remaining $n_X - n_S$ are exactly zero. Let the sparsity factor k_f be $k_f = n_S/n_X$. The lower k_f the higher the compression level is. For a n_S -sparse signal in a certain basis, only $2k$ numbers (n_S coefficients and their respective positions) suffice to describe the signal. $2k$ measurements are packaged and sent. FC recovers \mathbf{X} from \mathbf{S} by relation $\mathbf{X} = \Theta_{TC}^{-1}\mathbf{S}$ ([61]).

Under CS approach, compression operates on the signal \mathbf{X} with a diversifying matrix $\Psi_{CS} \subset \mathbb{R}^{n_Y \times n_X}$ by relation $\mathbf{Y}_{CS} = \Psi_{CS}\mathbf{X} \subset \mathbb{R}^{n_Y}$ with $n_Y \ll n_X$. Because $\mathbf{X} = \Theta_{TC}^{-1}\mathbf{S} = \Theta_{CS}\mathbf{S}$, following equality holds:

$$\mathbf{Y}_{CS} = \Psi_{CS}\mathbf{X} = (\Psi_{CS}\Theta_{CS})\mathbf{S} = \Phi_{CS}\mathbf{S} \quad (3.9)$$

where Φ_{CS} is the sampling matrix. Raw measurements in \mathbf{X} are linearly mixed by mean of Ψ_{CS} matrix to obtain \mathbf{Y}_{CS} . Moreover, because $n_Y \ll n_X$ CS approach hugely reduces radio transmissions in respect of the transform coding approach. The recovery procedure is achieved in two steps: 1) \mathbf{S} is recovered by \mathbf{Y}_{CS} with a not-linear procedure, 2) \mathbf{X} is obtained by \mathbf{S} by relation $\mathbf{X} = \Theta_{CS}\mathbf{S}$. While the second step is equal to what performed when the transform coding approach is considered, the former is more recent and it is based on the theory of principal component analysis (PCA). It has been demonstrated ([50]) that under certain hypothesis involving Ψ_{CS} , Θ_{CS} and the numerical value of n_Y , \mathbf{S} can be recovered by \mathbf{Y}_{CS} solving the following optimization problem in L_1 -norm:

$$\begin{aligned} \mathbf{S}^* &= \underset{\mathbf{S}}{\operatorname{argmin}} \|\hat{\mathbf{S}}\|_{L_1} \\ \text{s.t.} & \\ \|\mathbf{Y}_{CS} - \Phi_{CS}\hat{\mathbf{S}}\|_{L_2} &\leq a \end{aligned} \quad (\text{P})$$

being $a \geq 0$ a relaxation parameter of the optimization problem that trades off between the recovery precision ($a = 0$) and the optimization speed ($a > 0$) ([62]).

If Ψ_{CS} matrix is populated according to one of the following rules:

- 1) n_X column vectors are sampled uniformly at random on the unit sphere of \mathbb{R}^{n_Y} or
- 2) entries are sampled from the normal distribution with zero mean and variance $1/n_Y$ or
- 3) entries are sampled from a sub-Gaussian (Gaussian, Bernoulli,..) distribution with zero mean and variance $1/n_Y$,

then with overwhelming probability the optimization problem in (P) gives the exact reconstruction provided that:

$$n_Y \geq C \cdot n_X \cdot k_f \cdot \log\left(\frac{1}{k_f}\right)$$

Here, C is some constant depending on the signal sparsity, but it can be typically less than the unit (see [62] for more details).

3.5.2. CS approaches in WSN

Inspired to the classic formulation of Ψ_{CS} , many CS schemes affordable on WSN have been proposed in literature. In what follows, we briefly describe three CS method approaches: the classic CS ([45]), the causal random sampling CS ([53]) and the random sampling CS ([54]) (refers to the related bibliography for further details).

3.5.2.1. classic CS (cCS)

Ψ_{CS} is an $n_Y \cdot n_X$ random Bernoulli matrix with ± 1 entries. The compressive sampling operation in this case consists of n_Y linear combination of the n_X samples. Because the information content of n_X measurements is spread onto n_Y data, a complete set of n_X measurements is needed in this approach ([45]).

In this case, node acquires n_X measurements as in the conventional case, but $n_Y^{(i)}$ compressive measurements can be obtained by multiplying the n_X measurements with a $n_Y^{(i)} \cdot n_X$ random Bernoulli matrix with ± 1 entries. As a consequence, the CS operations consist in $n_Y^{(i)} \cdot n_X$ additions, n_X memory access for reading and $n_Y^{(i)}$ memory writing operations. In summary, the number of performed operation is $\left(n_Y^{(i)} \cdot n_X + n_X + n_Y^{(i)}\right)$ and the node energy model results:

$$\begin{aligned} \phi_{ACQ}^{(i,cCS)} &= n_X \cdot \phi_{ACQ}^0 \\ \phi_{SP}^{(i,cCS)} &= n_Y^{(i)} \cdot n_X \cdot \phi_{ADD}^0 + n_X \cdot \phi_{MRD}^0 + n_Y^{(i)} \cdot \phi_{MWR}^0 \\ \phi_{BCG}^{(i,cCS)} &= \left(n_Y^{(i)} \cdot n_X + n_X + n_Y^{(i)}\right) \cdot \phi_{BCG}^0 \\ \phi_{OP}^{(i,cCS)} &= \phi_{ACQ}^{(i,cCS)} + \phi_{SP}^{(i,cCS)} + \phi_{BCG}^{(i,cCS)} \end{aligned} \tag{3.10}$$

where $n_Y^{(i)}$ is the (deterministic) number of data samples for each ΔT and it may be different among nodes.

3.5.2.2. random sampling CS (rsCS)

In a random sampling CS ([55]) each node of the network sends samples with a probability $\rho_s \in [0, 1]$. For each ΔT , the FC receives a number of measurements $n_Y = n_Y(\rho_s)$ that corresponds to the number of active-to-sample nodes during that ΔT . This CS implementation equals to build an $n_Y \cdot n_X$ stochastic matrix Ψ_{CS} with (0,1) entries. Meanly speaking, n_Y is a random variable and it results that the mean value of gathered measurements, namely $\bar{n}_Y(\rho_s) = \text{mean}(n_Y(\rho_s))$ in the following, is function of ρ_s . Moreover, by its definition, it results: a) $\bar{n}_Y(\rho_s) \in [0, n_X]$, b) $\rho_s \rightarrow 0$ implies $\bar{n}_Y(\rho_s) \rightarrow 0$ and c) $\rho_s \rightarrow 1$ gives $\bar{n}_Y(\rho_s) \rightarrow n_X$. Authors ([55]) show that the CS reconstruction error is a convex function of ρ_s if packet losses (due to collisions) are considered. With such indications, the parameter ρ_s may be off-line designed in order to fulfil the reconstruction error requirement.

In this case, node operations consists in $n_Y^{(i)}(\rho_s)$ measurement acquisitions, followed by $n_Y^{(i)}(\rho_s)$ accesses to memory for writing operations. No other operations are performed. In these cases, the power consumption model can be defined as:

$$\begin{aligned}
 \phi_{ACQ}^{(i,rsCS)} &= n_Y^{(i)}(\rho_s) \cdot \phi_{ACQ}^0 \\
 \phi_{SP}^{(i,rsCS)} &= n_Y^{(i)}(\rho_s) \cdot \phi_{MWR}^0 \\
 \phi_{BCG}^{(i,rsCS)} &= n_Y^{(i)}(\rho_s) \cdot \phi_{BCG}^0 \\
 \phi_{OP}^{(i,rsCS)} &= \phi_{ACQ}^{(i,rsCS)} + \phi_{SP}^{(i,rsCS)} + \phi_{BCG}^{(i,rsCS)}
 \end{aligned} \tag{3.11}$$

where $n_Y^{(i)}(\rho_s) = \{0, 1\}$ are random experiments of some stochastic variables chosen accordingly to the indication given in the original chapter (i.e. [55]). Notice that for the rsCS strategy ρ_s is off-line chosen by the designer.

3.5.2.3. adaptive CS (aCS)

In a causal random CS (see [53] and references within) samples are acquired from the arbitrary set \mathbf{T} of times t_i generated by the Markov chain:

$$\mathbf{T} = \{t_i\} \text{ where: } t_i = t_{i-1} + \alpha \lceil \gamma_i \cdot \mu \rceil \tag{3.12}$$

where γ_i is a random variable uniformly distributed between (0,1), and α is a constant. In this case, n_Y is the cardinality of \mathbf{T} . That construction equivalently means to choose Ψ_{CS} as an $n_Y \cdot n_X$ stochastic matrix with (0,1) entries, with n_Y given by the cardinality of \mathbf{t} . From (3.12) clearly results that the random sampling time interval is set by means of μ . Let in this case define $\bar{n}_Y(\mu) =$

$\text{mean}(n_Y(\mu))$, it's by the way clear that $\bar{n}_Y = \bar{n}_Y(\mu)$. From its definition it results: a) $\bar{n}_Y(\mu) \in [0, n_X]$, b) $\mu \rightarrow \infty$ implies $\bar{n}_Y(\mu) \rightarrow 0$ c) for $\mu \rightarrow 0$ it is $\bar{n}_Y(\mu) \rightarrow n_X$.

In [53] it has been noted that sparsity property of a signal can vary over time and a fixed value of n_Y produces low recovery performances. The authors propose an algorithm, named the adaptive CS (aCS in the following), that on-line sets n_Y dynamically in order to steer the reconstruction error (estimated with a procedure described below) to a desired reference value. In [53] the aCS is specifically applied on the causal random CS, so that authors control the μ parameter to dynamically set n_Y .

The main steps of the procedure can be summarized as follows: a) FC acquires n_Y measurements and also o additional reserved samples, b) the recovered signal from the n_Y measurements is compared with the o reserved samples to determine the reconstruction error estimation, c) a control law is then used to set a new value of μ that steers the estimated reconstruction error to the desired performance value. The aCS method requires a sufficient set of measurements in order get a good estimation of the reconstruction error as well as additional packets to send from the FC to the sensors to set the μ parameter. This may result in an additional amount of power consumption. In this case, node operations consists in $n_Y^{(i)}(\mu)$ measurement acquisitions, followed by $n_Y^{(i)}(\mu)$ accesses to memory for writing operations. No other operations are performed. In these cases, the energy model can be defined as:

$$\begin{aligned}
 \phi_{ACQ}^{(i,aCS)} &= n_Y^{(i)}(\mu) \cdot \phi_{ACQ}^0 \\
 \phi_{SP}^{(i,aCS)} &= n_Y^{(i)}(\mu) \cdot \phi_{MWR}^0 \\
 \phi_{BCG}^{(i,aCS)} &= n_Y^{(i)}(\mu) \cdot \phi_{BCG}^0 \\
 \phi_{OP}^{(i,aCS)} &= \phi_{ACQ}^{(i,aCS)} + \phi_{SP}^{(i,aCS)} + \phi_{BCG}^{(i,aCS)}
 \end{aligned}
 \tag{3.13}$$

where $n_Y^{(i)}(\mu) \in [0, n_X]$ are random experiments of some stochastic variables chosen accordingly to the indication given in the original chapter (i.e. [53]). We point out that μ is dynamically controlled over time.

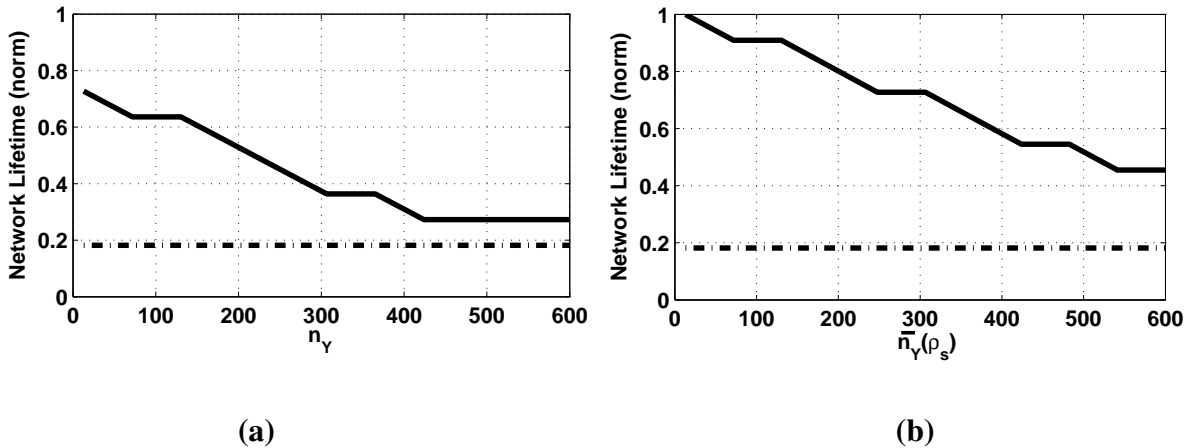
3.5.3. Co-design example of Compressive Sensing methods

In this example, we fix the network model parameters to the values reported in Table 3.3, while the packet loss model is with the following parameters: $\Delta_{tf} = 100$ sec and $\Delta_{tp} = 0.2$ sec as in [55]. To the design purpose, let assume that $MSE^{(n_Y)} \in [0.2; 0.4]$ is an acceptable reconstruction error range for the application in use.

Preliminary, a performance evaluation (in terms of network lifetime and reconstruction error) of the presented CS schemes (cCS, rsCS and aCS) in both absence and presence of packet collisions

Parameter	Value
n_X	900
o	500
$e_i^c(0)$	25kJ
E_{TH}	0.25J
n	100
B_P	1016
ϕ_{TX}^0	0.78 mJ

Table 3.3.: Simulator parameters assumed as constants in the proposed simulations.

Figure 3.3.: Network Lifetime (T_l) vs (a) n_Y for cCS (continuous line) and (b) ρ_s for rsCS (continuous line). No-compression approach (dashed lines).

is carried out. During this simulative campaign, we vary n_Y , $\bar{n}_Y(\rho_s)$ and $\bar{n}_Y(\mu)$ within their respective ranges. Consequently, a co-design example based on the simulation results is provided in order to choose the more suitable CS scheme and the related parameters that fulfils the required performances.

3.5.3.1. cCS and rsCS analysis

In this paragraph, we compare the cCS and the rsCS approaches in terms of network lifetime and reconstruction error performance.

According with the provided model, the network lifetime is function of n_Y both in cCS and rsCS methods. In Fig. 3.3.(a) and Fig. 3.3.(b) (continuous lines) we compute the lifetime of network when cCS and rsCS (respectively) methods are adopted for data representation. The simulations are carried out by varying the number of measurements (resp. n_Y and $\bar{n}_Y(\rho_s)$). In the same plots,

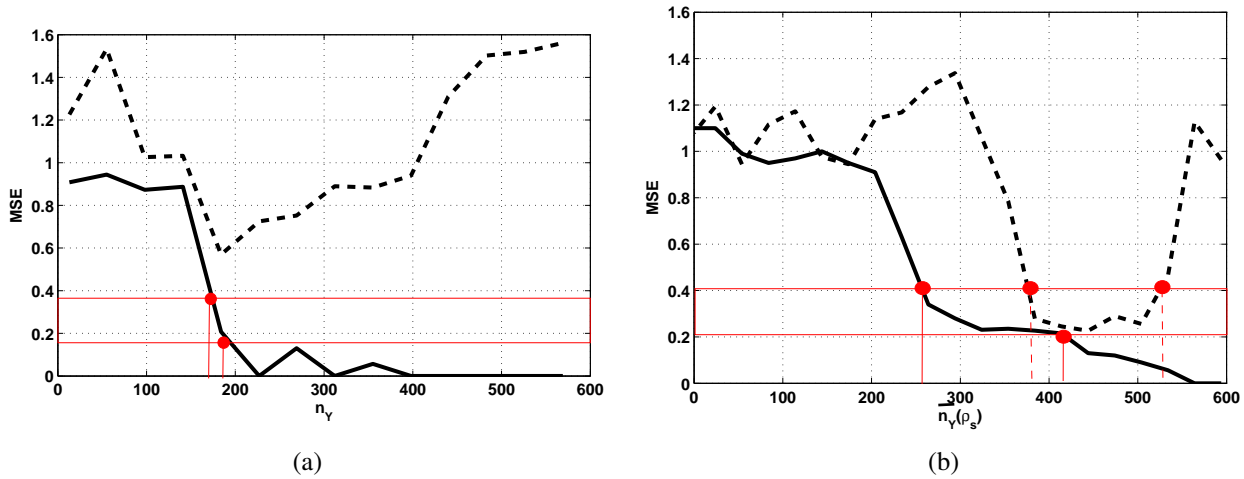


Figure 3.4.: Reconstruction error $MSE^{(n_Y)}$ for: **(a)** cCS as function of n_Y and **(b)** rsCS as function of $\bar{n}_Y(\rho_s)$, in ideal case of no-packet loss (continuous lines) and if packet collisions are considered (dashed lines).

dashed curves represent the computed normalized lifetime when any compression mechanisms is adopted and $n_X = 900$ (with $n_X > n_Y$) raw samples are sent to the FC. Curves in Fig. 3.3 have been normalized to the maximum achieved lifetime. By comparing continuous curves with dashed ones, it results that both CS approaches increase the network lifetime. Moreover, if cCS or rsCS curves are considered, an increasing of the amount of processed measurements (n_Y or $\bar{n}_Y(\rho_s)$) reduces the network lifetime. It is interesting to note that in this simulation rsCS method performs better than cCS in terms of network lifetime. According to the provided model, this is due to both a lower computation cost and a lower volume of traffic data in respect to the case when rsCS method is adopted.

About reconstruction error, simulation results are presented in Fig. 3.4 (resp. cCS strategy in Fig. 3.4.(a) and rsCS in Fig. 3.4.(b)). We conduct the simulations under the both cases of a) negligible packet collision events (continuous lines) and b) under the case where packet collisions have been taken into account (dashed lines).

Let preliminary analyse the continuous curves. For both CS strategies, the increase of n_Y and $\bar{n}_Y(\rho_s)$ respectively gives a better reconstruction performance, but however, the rsCS approach (Fig. 3.4.(b)) because the overall amount of data sent to FC is reduced.

Let consider now the reconstruction error evaluation in presence of packet collisions (dashed lines in Fig. 3.4). In a WSN communication, the presence of packet loss is a typical event, especially for centralized scheme. In presence of collision, FC is not able to receive data and for this reason

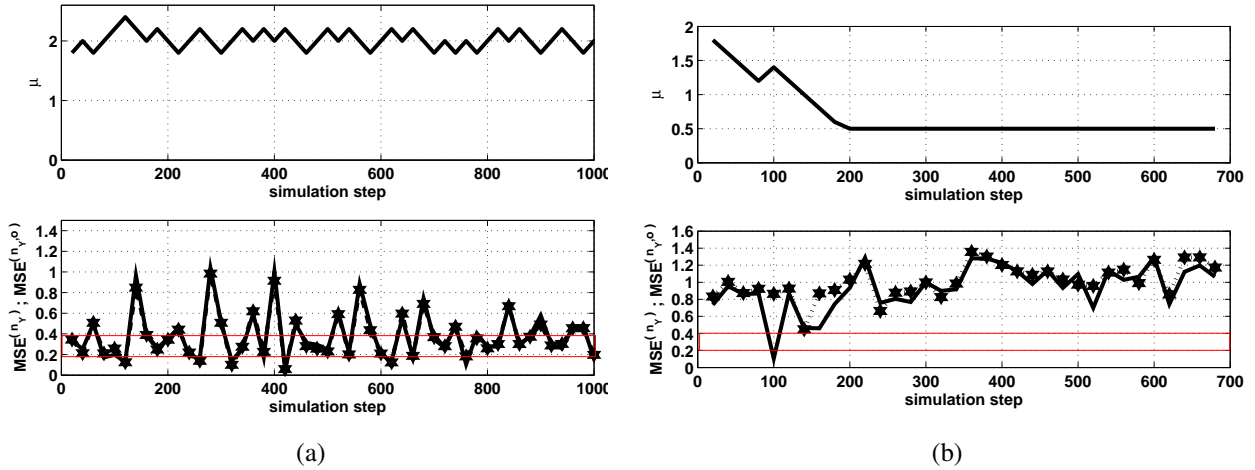


Figure 3.5.: aCS: dynamic evolution of (upper panels) μ and (lower panels) reconstruction errors $MSE^{(n_Y)}-MSE^{(n_Y|o)}$ (continuous lines - dashed lines with star markers respectively) under the case of (a) absence of packet loss and (b) presence of packet loss.

they can be considered as rejected by the communication. Such exception is typically managed in two ways by the FC: a) it sends a request back to the network until the data is obtained or b) it tries to reconstruct data from the set of the received measurements also if collisions are detected. The former does not seem to be a valid solution for WSN monitoring application because it increases the network congestion and the power consumption of communication. For this reason, we assume that FC tries to recover signal from the received set of sampled data, without any retransmission request. The simulation has been pictured in in Fig. 3.4 (dashed line). In both cases of cCS and rsCS approaches, simulation results show a worsening of performances than in the case of absence in packet loss at higher n_Y (and $\bar{n}_Y(\rho)$). Moreover, it is worth of note the presence of a band of low values of reconstruction errors in both of cases. That is because for high values of n_Y (or $\bar{n}_Y(\rho_s)$) the packet loss probability is very high ($> 90\%$) and, consequently, $MSE^{(n_Y)}$ has lower performance compared with the ideal case of absence of losses. Conversely, if low number of n_Y (or $\bar{n}_Y(\rho)$) are considered, the packet loss probability is low but the reconstruction error assumes however high values. As a result, the central bands guarantee a good trade off between a n_Y (and $\bar{n}_Y(\rho)$) and a relatively low probability of packet collision.

3.5.3.2. aCS analysis

Let in this paragraph analyse the network lifetime and the reconstruction error performances in the case of aCS approach. We choose to analyse this approach apart because in this case we cannot

set arbitrarily the value of n_Y , but we expect that the methodology is able to automatically decides on n_Y to achieve the desired reconstruction performance. In Fig. 3.5 we show the performance evaluation of aCS in absence and in presence of packet losses (resp. Fig. 3.5.(a) and Fig. 3.5.(b)). In both cases we have simulated the network until the first node faults. The simulation in Fig. 3.5.(a) shows that the aCS correctly performs the $MSE^{(n_Y|o)}$ error estimation and therefore the control action on μ parameter in order to get the desired performance. Some considerations arise from the provided performance evaluation:

- a. the packet loss makes hard to steer the reconstruction performance at the desired value. Indeed, μ decreases (i.e. the transmission rate increases accordingly) while the evaluation of the reconstruction error worsens, until it saturates to a minimum value. This is mainly due to the network collapse phenomena. Indeed, packet collision increases the reconstruction error that in turn increases the node sending rate (μ is decreased by the FC controller);
- b. the presence of packet loss also affects the $MSE^{(n_Y|o)}$ estimation. Indeed, while in Fig. 3.4.(a) $MSE^{(n_Y|o)}$ and $MSE^{(n_Y)}$ overlap or are very close one to each other, in Fig. 3.4.(b) $MSE^{(n_Y|o)}$ differs to $MSE^{(n_Y)}$ in almost all the simulation time. This implies a wrong adaptation of the control variable μ with the worsening of the network performance;
- c. a wrong control of μ parameter may affect the lifetime performance, due to the network collapse phenomenon (discussed in point a.) that increases the number of packets into the network and, so, the power consumption. This is confirmed by the simulation, producing a network lifetime $T_l > 1000$ in absence of packet collisions (3.4(a)), while $T_l = 700$ in presence of packet collisions (3.4(b)).

3.5.3.3. Discussion

The above simulation results may be used by a network designer to choose the more suitable CS scheme and its related parameters in order to fulfil the required design performances. We carry our co-design example by distinguish between two different cases: a) the channel is collision-free (packet loss is negligible), b) the channel works in presence of packet collisions.

- a) In this case, all the above CS methods (cCS, rsCS and aCS) are able to fulfil the reconstruction error requirements (Fig. 3.4 and Fig. 3.5). In particular, if cCS approach is considered (Fig. 3.4.(a)) we can tune $n_Y \in [180; 190]$. Otherwise, if rsCS approach is considered, we may set $\bar{n}_Y(\rho_s) \in [260; 410]$ (Fig. 3.4.(b)) to obtain the required performance. To the design purpose, the choice on which method is more suitable for the WSN depends on the lifetime performance. Indeed, from Fig. 3.3.(a) and Fig. 3.3.(b), it results that by cCS

approach the network lifetime is $T_l \in [0.6; 0.7]$ when $n_Y \in [180; 190]$ (Fig. 3.3.(a)), while in the case of rsCS approach, it is $T_l \in [0.6; 0.9]$ in $\bar{n}_Y(\rho_s) \in [260; 410]$ (Fig. 3.3.(b)). In conclusion, according to the above simulation results, we may choose the rsCS method with $\bar{n}_Y(\rho_s) = 260$ in order to maximize network lifetime ($T_l = 0.9$) and minimize the reconstruction error ($MSE^{(n_Y)} \sim 0.4$).

- b) Conversely, if the packet collision phenomenon is considered (with the model parameters given above), both cCS (Fig. 3.4.(a), dashed line) and aCS (Fig. 3.5.(b), dashed line) are unable to get the desired reconstruction performance, and in this case, the choice can only fall upon the rsCS method that returns $MSE^{(n_Y)} \in [0.2; 0.4]$ with $\bar{n}_Y(\rho_s) \in [380; 510]$ (Fig. 3.4.(b)). On the base of the provided simulation results in Fig. 3.3.(b) and Fig. 3.4.(b) we may choose $\bar{n}_Y(\rho_s) = 380$ that gives $T_l = 0.6$ and reconstruction error $MSE^{(n_Y)} \sim 0.4$.

3.6. Conclusion

In this chapter, we presented a software co-design tool which can aid the network designer to the optimization of the performances of a monitoring WSN. It was assumed that the WSN adopts a compression algorithm to represent information that it samples during the monitoring activity. Preliminarily, we formulated a WSN model taking into account a model of node power consumption and of a traffic model based on the concepts of graph theory and Dijkstra's routing path. Effects of packet collision phenomena (typically affecting wireless communication) were also added to the traffic model managed by each node. After having introduced two important performances for the WSN monitoring, the system autonomy and the signal error carried out by the process of compression, the provided WSN model was proposed as a tool for the software co-design of system parameters that are related to the compression method in order to fulfil given performance specifications about energy autonomy or reconstruction error. The model was particularized to the representative case where network performs Compressive Sensing schemes for data representation. In this case, we firstly analysed and compared the performances of different variants of Compressive Sensing schemes under some indicative scenarios. Consequently, one example of software co-design aimed to improve both recovery error and network autonomy has been presented.

Part II.

Control approaches for EH-WSNs

Control techniques for harvesting system energy management

4.1. Motivation

DURING last years the formulation of strategies for the harvesting system management has recently played an important role in WSN design. Wireless nodes can operate in two main modes of operation: low power mode and full operation mode. In low power mode, the wireless transmitter is switched off to save energy. In this state, the node is momentarily disconnected to the WSN and is unable to both receive data from and transmit data to the network. It should be important to implement energy management strategies that schedule node activity to prolong node lifetime.

An additional requirement for wireless node is to provide high power and high energy supply. This performance can be only partially covered by Li-Ion batteries that are subjected to life degradation phenomena when operate under impulsive current requirements. Ultracapacitor technology achieves higher power density but lower energy density than battery technology. Some Li-Ion polymer batteries reach the same power density, but at much higher prices [63]. In counterpart, ultracapacitor provides lower energy density than the battery. Additionally, ultracapacitor technology is also characterized by negligible degradation effects compared to the battery technology. To cope with these limitations, hybrid supply systems, composed of a battery and an ultracapacitor, have been recently introduced to supply wireless nodes [64]. The ideal hybrid system should ensure at the same time battery life preservation and supply autonomy.

Many hybrid schemes and control laws have been proposed in literature. A hybrid supply configuration for EH-WSN that manages the battery to maximize its life and that increases autonomy has not been proposed in literature.

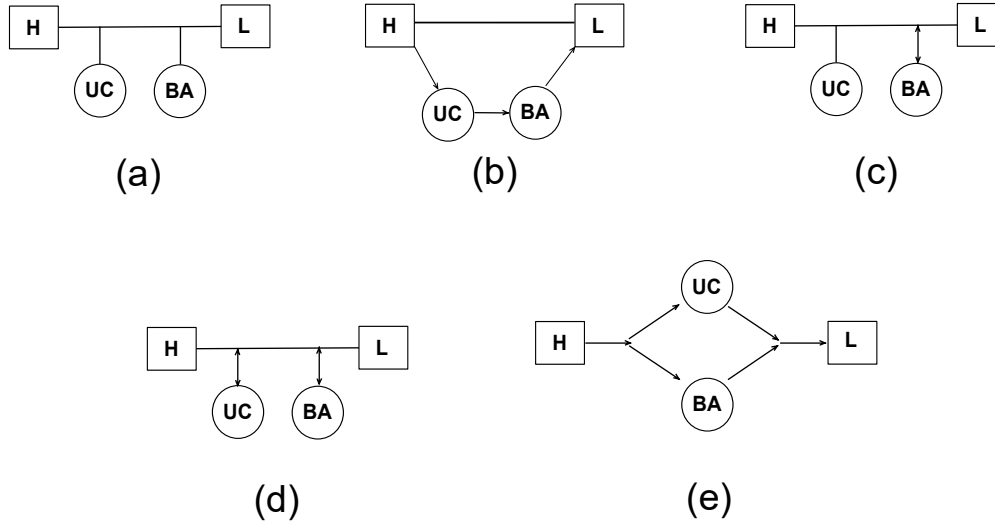


Figure 4.1.: Overview of hybrid power system topologies: (a) to (d) schemes studied in literature; (e) the proposed hybrid scheme.

In this chapter, a novel hybrid system configuration scheme including these functionalities is therefore proposed. A Model Predictive Control for the energy management of node harvesting system is formulated by taking into account: hybrid system and the battery degradation models. Motivating by the fact that predictive controllers are computationally expensive to be implemented in a micro-controller, a more suitable suboptimal *adaptive* strategy is finally proposed. Simulation tests of the proposed control laws are carried out in order to compare performances and validate their effectiveness under two realistic harvesting scenarios in comparison with a standard controller, proposed in literature.

4.2. Related works

Hybrid systems are composed of the following main components: a) harvesting conversion unit; b) battery and ultracapacitor storage devices; c) load device to be supplied (i.e wireless node). In literature, hybrid systems can be distinguished among passive ([65, 66]) and active ([67, 68, 69]) configurations. In Fig. 4.1 configurations from (a) to (d) represent the main hybrid power systems proposed in literature. In such representation, Harvesting system and Load are respectively labelled with "H" and "L", while ultracapacitor (UC) and battery (BA) devices are also represented. Direct connections between boxes are denoted with simple lines, while single and double arrowed lines connect blocks throughout a controllable logic (e.g. a dc/dc converter). In passive configurations, battery and ultracapacitor devices are connected in parallel and directly coupled to the load (Fig. 4.1.(a)). Active configurations use one or more dc/dc converters and control circuitry to manage the

recharge processes in controlled environment. They are mainly adopted in many contexts different from Wireless Sensor Networks (e.g. automotive), because their implementation typically requires high computation.

In [70] authors design and implement a hybrid system with topology configuration in Fig. 4.1.(b). The adopted scheme in this case is able to separate between ultracapacitor recharge and battery supply. Block H can directly supply the sensor node when energy is sufficient, while harvests charge into the ultracapacitor and uses independently a reservoir battery when otherwise harvesting energy is not sufficient. Nevertheless, the ultracapacitor is only used to harvest energy, but cannot be used to supply directly the load, and battery can be subject to degradation of performance.

In [71] authors implement active configuration in Fig. 4.1.(c). In this case, there is a direct power chain from block H to L. Ultracapacitor is electrically connected to the power chain, while battery is connected throughout a bi-directional dc/dc converter. Control strategy is aimed to regulate the UC voltage level in order to reduce the dc/dc converters drop out voltages of the circuits and minimize dc/dc converter losses. In this configuration, battery is used as a reservoir, but degradation effects are not taken into account.

Studies in [72] considers the hybrid system of Fig. 4.1.(d). In this case, the following strategy is implemented: when the load current is small, battery supplies node. The discharge rate of the battery is determined by the average load demand. To protect the battery, current is controlled in order to not exceed its safety limits. On the other hand, when load current is high, both the battery and the ultracapacitor supply the sensor node. By controlling the battery current at a constant value throughout this time, the battery can be kept in a safe operative area and capacity fading effect are limited. The same scheme is considered in [73], where a different management strategy is proposed. Ultracapacitor is mainly recharged by the harvester and used to supply the node. However, two conditions may cause the ultracapacitor to be disabled: over-voltage protection and excessive discharge. In both cases, battery is eligible to be recharged by the harvester or by the ultracapacitor. Load is supplied with a combination of battery and ultracapacitor. Being the battery limited in both charge and discharge, degradations are negligible.

A drawback in the above hybrid schemes is the following. They implement a direct connection from the harvesting to the load, and both battery and ultracapacitor can be used only one at time. Indeed, if the battery is used to supply the load, the ultracapacitor cannot be recharged solely from the harvesting, since the battery will also supply the ultracapacitor through the bus connection. Moreover, the supply system autonomy is a peculiar aspect neglected in the above works. In energy harvesting systems, node supply autonomy is ensured if actions are taken on the basis of future harvesting expectancy. A wireless node activity should be scheduled over a long time prediction for prolonging node autonomy.

To overcome the above drawbacks, in this chapter the active configuration in Fig. 4.1.(e) is proposed. The four independent branches allow to recharge battery while the ultracapacitor supplies the output and vice-versa. It is also possible to connect both devices to block H or to block L. Finally, a predictive controller, aimed at ensure prolonged supply autonomy is proposed. This performance is achieved throughout the proposed hybrid system in Fig. 4.1.(e). Specifically, the two output branches allow the controller to allocate the optimal amount of energy resources in order to extend supply autonomy. This performance is achieved by triggering the node duty cycle, so the energy reserve is spread out over a prolonged time. Since, however, reducing node duty cycle leads to lower communication performance of node throughout the network, the optimal allocation of both energy resources and of node duty cycle is a non trivial task because, it may outperform the physical layer specifications but without worsen too much the network communication performances.

4.2.1. Chapter contribution and outline

In the following, the main contributions of the present study are highlighted.

1. A novel hybrid system scheme in Fig. 4.1.(e) is proposed. By controlling the discharge and recharge current flows into battery and ultracapacitor, battery degradation can be reduced. Additionally, the proposed scheme is able to control the node consumption as function of the available energy resource in order to ensure prolonged lifetime.
2. A predictive control framework is formulated. Differently from other controllers typically implemented for EH-WSN, it includes two additional objectives: a) to extend energy autonomy of node; b) to preserve battery from capacity degradation. To achieve objective a) the controller takes into account a prediction of future harvested energy over a finite horizon to regulate the optimal node duty cycle and, therefore, extending node autonomy.
3. Since predictive controllers are computationally expensive and are not suitable for WSN, an adaptive control strategy is additionally proposed. Differently from classic controllers it includes both the duty cycle adaptation and a strategy to reduce battery degradation. The main functionalities can be summarized as follows: a) energy harvesting collected by the hybrid system is maximized, b) battery usage is limited in order to reduce its degradation over time, c) node duty cycle is scheduled on the basis of the energy resource expected within a finite time horizon. In particular: if harvested energy suffices, the controller regulates the node to operate at its maximum duty cycle. Whenever energy cannot satisfy node demand, the adaptive control ensures continuous node operation with reduced duty cycle. As a result, the proposed controller steers node duty cycle in order to adaptively balance the energy demand to the expected energy resource.

4. A simulation campaign validates the effectiveness of the proposed controllers compared with a threshold-based energy management strategy typically adopted in literature [73]. It is shown that the proposed adaptive algorithm outperforms the threshold-based one, despite it performs less than model predictive controller. Therefore, the proposed adaptive strategy reduces the gap between standard threshold-based approaches and the optimal predictive one.

5. Finally, an implementation of the hybrid system scheme in Fig. 4.1.(e) is provided and a prototype of the proposed scheme is designed. Details of hybrid scheme implementation are provided in Appendix B.

Chapter outline Chapter is organized as follows: in Sec. 4.3, background on Model Predictive Control is briefly introduced. In 4.4 modelling of battery and the ultracapacitor in the configuration scheme of Fig. 4.1.(e) is provided. In Sec. 4.5 three strategies are considered: the MPC-based control law, a commonly used threshold-based strategy and the proposed adaptive strategy. In Sec. 4.6 simulations validate the effectiveness of the proposed strategy, compared with the threshold-based one and the predictive controller. Finally, in Appendix B the implementation of the proposed hybrid scheme is detailed. Conclusions are made in Sec. 4.7.

4.3. Background

Model Predictive Control (MPC) is a well known control method that computes a trajectory of control variables to optimize the future behaviour of the plant. The optimization is performed within a finite time window, which time duration is the prediction horizon. Starting from the knowledge of plant state at the beginning of the time window, the MPC has the ability to anticipate future events and can take control actions accordingly. Usually, linear empirical models obtained by system identification are adopted in model predictive controllers to estimate future plant dynamics, but the control can be also extended to non linear models. Consider the following general discrete time system model:

$$\mathbf{x}(k+1) = f(k, \mathbf{x}(k), \mathbf{u}(k)) \quad (4.1)$$

where \mathbf{x} is the state vector, \mathbf{u} is the control input and f is the state function. System (4.1) is subject to state and input constraints: $\mathbf{x}(k) \in \mathfrak{X}$ and $\mathbf{u}(k) \in \mathfrak{U}$ for all k . The control objective is to minimize a cost function $J_N(\mathbf{x}(k), \mathbf{U}(k))$ defined as follows:

$$J_N(\mathbf{x}(k), \mathbf{U}(k)) = \sum_{n=k}^{k+N-1} l(\mathbf{x}(n), \mathbf{u}(n)) \quad (4.2)$$

where $\mathbf{U}(k) = [\mathbf{u}(k), \mathbf{u}(k+1), \dots, \mathbf{u}(k+N-1)]$ is a sequence of inputs within the predictive horizon N , $\mathbf{x}(n)$ is the state trajectory obtained by applying the control sequence $\mathbf{U}(k)$ to the system (4.1) starting from the initial state $\mathbf{x}(k)$ and $l(\cdot, \cdot)$ is the stage cost at each timeslot $n \in [k, k+N-1]$. At each k , solve the following finite time optimization problem:

$$\begin{aligned} \min_{\mathbf{U}_{\{k\}}} \quad & J_N(\mathbf{x}_k, \mathbf{U}_{\{k\}}) \\ \text{s.t.} \quad & \mathbf{x}_{\{n+1,k\}} = f(n, \mathbf{x}_{\{n,k\}}, \mathbf{u}_{\{n,k\}}) \in \Xi, \quad n = k, \dots, k+N-1 \\ & \mathbf{u}_{\{n,k\}} \in \Upsilon, \quad n = k, \dots, k+N-1 \\ & \mathbf{x}_{\{k,k\}} = \mathbf{x}(k) \end{aligned} \quad (4.3)$$

where: $\mathbf{u}_{\{n,k\}}$ are the future control actions for all $n \in [k, \dots, k+N-1]$; $\mathbf{x}_{\{n,k\}}$ denotes the future state vectors at time instant $n \in [k, k+N-1]$ obtained by $\mathbf{x}_{\{n+1,k\}} = f(n, \mathbf{x}_{\{n,k\}}, \mathbf{u}_{\{n,k\}})$. Denoting with $\mathbf{U}_{\{k\}}^* = [\mathbf{u}_{\{k,k\}}^*, \mathbf{u}_{\{k+1,k\}}^*, \dots, \mathbf{u}_{\{k+N-1,k\}}^*]$ the optimal control sequence over the time horizon N , only the first sample $\mathbf{u}_{\{k,k\}}^*$ will be applied to the system:

$$\mathbf{u}(k) = \mathbf{u}_{\{k,k\}}^* \quad (4.4)$$

Then, at the next sampling time $k+1$ problem above (4.3) will be solved over a shifted horizon $n \in [k+1, k+N]$, yielding to a receding horizon control strategy.

4.4. System modelling

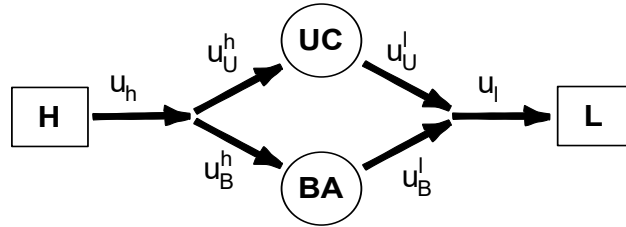


Figure 4.2.: Proposed hybrid system for WSN.

In this section, the analytical model of system scheme in Fig. 4.1(e) is formulated. In Fig. 4.2 the proposed model is reported with details on the adopted variables. Arrows represent the electrical current flowing among the hybrid system blocks. We denote with u_h and \hat{u}_h respectively the average and the maximum current generated by the harvester block H. Notice that, due to the non-constant harvesting resource, \hat{u}_h is time-varying. On the other hand, u_l and \hat{u}_l are respectively the average and the maximum current required by the node. Moreover, u_U^h and u_B^h denote the average value

of currents that recharge the ultracapacitor and the battery, respectively. Similarly, u_U^l and u_B^l are related to the average currents provided to the load from the ultracapacitor and the battery, respectively. In the proposed block scheme in Fig. 4.2, it is assumed that is possible to control harvesting flows u_U^h and u_B^h and to control load flows u_U^l and u_B^l through a dedicated control logic. We have that: $u_U = -u_U^h + u_U^l$ and $u_B = -u_B^h + u_B^l$, being u_U and u_B the net average current outgoing from the ultracapacitor and the battery, respectively. Let introduce the following variables: $\lambda_1 = \frac{u_U^h}{\hat{u}_h}$, $\lambda_2 = \frac{u_B^h}{\hat{u}_h}$, $\lambda_3 = \frac{u_U^l}{\hat{u}_l}$ and $\lambda_4 = \frac{u_B^l}{\hat{u}_l}$. By definition, $\lambda_1, \lambda_2, \lambda_3, \lambda_4 \in [0, 1]$. Moreover, we have:

$$\begin{aligned} u_h &= (\lambda_1 + \lambda_2)\hat{u}_h \\ u_l &= (\lambda_3 + \lambda_4)\hat{u}_l \end{aligned} \quad (4.5)$$

and

$$\begin{aligned} u_U &= -\lambda_1\hat{u}_h + \lambda_3\hat{u}_l \\ u_B &= -\lambda_2\hat{u}_h + \lambda_4\hat{u}_l \end{aligned} \quad (4.6)$$

Notice that: $\lambda_1 + \lambda_2 \leq 1$ and $\lambda_3 + \lambda_4 \leq 1$. Notice also that node is active for a fraction of time that is $\delta = \frac{u}{\hat{u}_l} = \lambda_3 + \lambda_4$. δ will be referred with the name of *active fraction* in the following.

4.4.1. Ultracapacitor and Battery electrical models

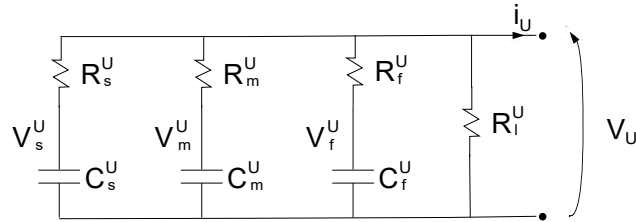


Figure 4.3.: Ultracapacitor equivalent dynamic model.

4.4.1.1. Ultracapacitor

An equivalent UC circuit model adopted in literature [74, 75] is represented in Fig. 4.3. With reference to Fig. 4.3, i_U is assumed to be positive when it flows out the UC. The ultracapacitor State-Of-Charge (SOC_U in the following) is defined as the ratio between the instantaneous charge stored into the UC ($Q_U(t)$) and the maximum charge value, Q_U^{max} , i.e. $SOC_U(t) = Q_U(t)/Q_U^{max}$. The SOC_U is given by:

$$SOC_U = \frac{1}{Q_U^{max}} \left(C_f^U \cdot V_f^U + C_m^U \cdot V_m^U + C_s^U \cdot V_s^U \right) \quad (4.7)$$

being: $Q_U^{max} = (C_f^U + C_m^U + C_s^U) \cdot V_U^{max}$ with V_U^{max} the maximum voltage of the UC. Let define the three time constants of the equivalent UC model in Fig. 4.3 as:

$$\begin{aligned}\tau_f^U &= C_f^U \cdot R_f^U \\ \tau_m^U &= C_m^U \cdot R_m^U \\ \tau_s^U &= C_s^U \cdot R_s^U\end{aligned}\tag{4.8}$$

and the equivalent resistance is $R_x^U = \left(\frac{1}{R_f^U} + \frac{1}{R_m^U} + \frac{1}{R_s^U} + \frac{1}{R_l^U}\right)^{-1}$. Let consider the following set of

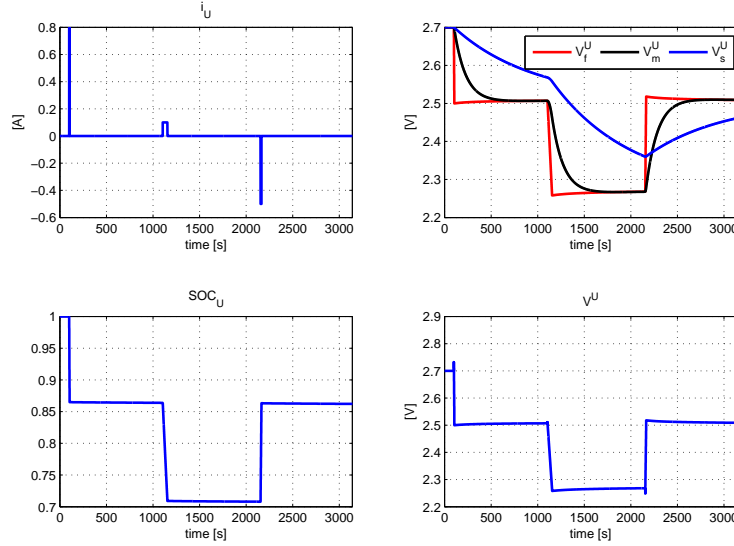


Figure 4.4.: Dynamic response of an UC model.

UC variables:

$$\begin{aligned}\mathbf{x}_U(t) &= [V_f^U(t) \quad V_m^U(t) \quad V_s^U(t)]^T \\ \mathbf{y}_U(t) &= [V^U(t) \quad SOC_U(t)]^T \\ u_U(t) &= i_U(t)\end{aligned}\tag{4.9}$$

The UC model can be written as [76, 77]:

$$\begin{aligned}\dot{\mathbf{x}}_U(t) &= \mathbf{A}_U \cdot \mathbf{x}_U(t) + \mathbf{B}_U \cdot u_U(t) \\ \mathbf{y}_U(t) &= \mathbf{C}_U \cdot \mathbf{x}_U(t)\end{aligned}\tag{4.10}$$

where:

$$\mathbf{A}_U = \begin{pmatrix} \frac{1}{\tau_f^U} \left(\frac{R_x^U}{R_f^U} - 1 \right) & \frac{1}{\tau_f^U} \frac{R_x^U}{R_m^U} & \frac{1}{\tau_f^U} \frac{R_x^U}{R_s^U} \\ \frac{1}{\tau_m^U} \frac{R_x^U}{R_f^U} & \frac{1}{\tau_m^U} \left(\frac{R_x^U}{R_m^U} - 1 \right) & \frac{1}{\tau_m^U} \frac{R_x^U}{R_s^U} \\ \frac{1}{\tau_s^U} \frac{R_x^U}{R_f^U} & \frac{1}{\tau_s^U} \frac{R_x^U}{R_m^U} & \frac{1}{\tau_s^U} \left(\frac{R_x^U}{R_s^U} - 1 \right) \end{pmatrix}\tag{4.11}$$

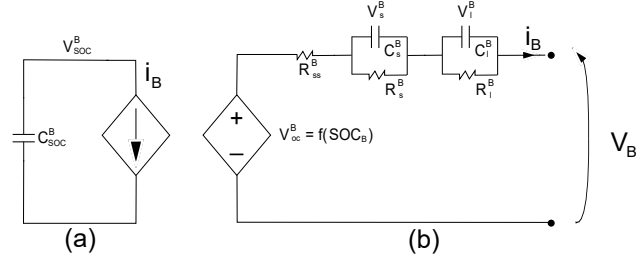


Figure 4.5.: Battery equivalent model: (a) SOC dynamics, (b) voltage dynamics.

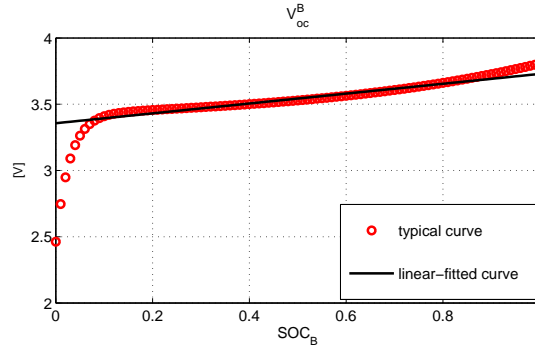


Figure 4.6.: Example of non linear and linearly approximated relation between SOC_B and V_{oc}^B .

$$\mathbf{B}_U = \begin{pmatrix} -\frac{R_x^U}{\tau_f^U} & -\frac{R_x^U}{\tau_m^U} & -\frac{R_x^U}{\tau_s^U} \end{pmatrix}^T \quad (4.12)$$

$$\mathbf{C}_U = \begin{pmatrix} \frac{R_x^U}{R_f^U} & \frac{R_x^U}{R_m^U} & \frac{R_x^U}{R_s^U} \\ \frac{C_f^U}{Q_U^{max}} & \frac{C_m^U}{Q_U^{max}} & \frac{C_s^U}{Q_U^{max}} \end{pmatrix} \quad (4.13)$$

An example of UC system respond to impulsive current profile is shown in Fig. 4.4.

4.4.1.2. Battery

Many different battery models have been proposed in literature. In this chapter, we consider the equivalent model of Fig. 4.5, [78, 79]. It is composed of two parts: part (a) models the relation between the output current and battery State-of-Charge (SOC_B in the following); part (b) models the output voltage dynamic as function of current applied and SOC_B . It takes into account a non linear relation between SOC_B and the open circuit voltage of the battery, V_{oc}^B (evaluated for $i_B = 0$).

About circuit part (a) in Fig. 4.5 the SOC_B is defined as $SOC_B(t) = Q_B(t)/Q_B^{max}$, where: $Q(t) = C_{SOC}^B V_{SOC}^B(t)$ is the current level of charge stored into the battery and Q_B^{max} the maximum battery

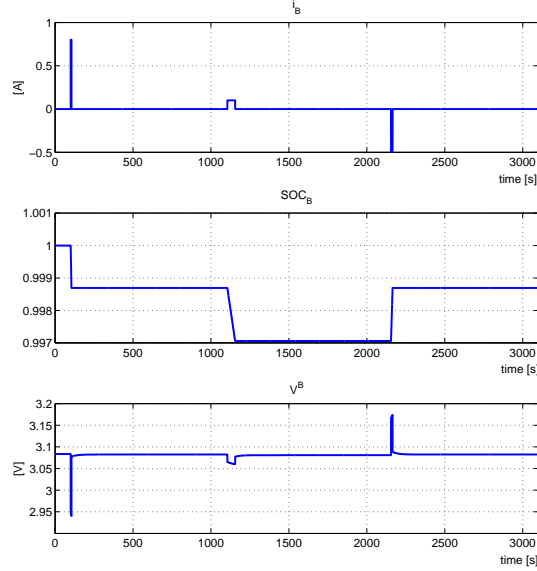


Figure 4.7.: Dynamic response of an BA model.

capacity. It results: $\frac{dV_{SOC}^B}{dt}(t) = \frac{1}{C_{SOC}^B} i_B$. Many experimental studies [41, 80, 81] consider a non linear relation between $SOC_B(t)$ and $V_{oc}^B(t)$, such as ([82]):

$$V_{oc}^B(t) = \alpha_0 + \alpha_1 SOC_B(t) + \alpha_2 SOC_B^2(t) + \alpha_3 SOC_B^3(t) + \alpha_4 e^{(\beta SOC_B(t))} \quad (4.14)$$

In Fig. 4.6 the typical V_{oc}^B - SOC_B relation for Li-Ion battery is shown. It is also shown that, despite the non linearity at low and high values of SOC_B , it is possible to fit the non linear curve with a linear one assuming $SOC_B \in [0.2; 0.8]$ (Fig. 4.6). Therefore, in the following of this work it will be assumed that:

$$V_{oc}^B(t) = \alpha_{oc} SOC_B(t) + \beta_{oc} \quad (4.15)$$

From the scheme in Fig. 4.5, let define the time constants:

$$\begin{aligned} \tau_f^B &= C_f^B \cdot R_f^B \\ \tau_s^B &= C_s^B \cdot R_s^B \end{aligned} \quad (4.16)$$

and let the battery model vectors be:

$$\begin{aligned} \mathbf{x}_B(t) &= [V_s^B(t) \quad V_f^B(t) \quad SOC_B(t)]^T \\ \mathbf{y}_B(t) &= [V^B(t) \quad SOC_B(t)]^T \\ u_B(t) &= i_B(t) \end{aligned} \quad (4.17)$$

According to the electrical equivalent model in Fig. 4.5(b), we have:

$$V^B(t) = V_{oc}^B(t) - R_{ss}^B u_B(t) - V_s^B(t) - V_f^B(t) \quad (4.18)$$

with R_{ss}^B being the series resistance in the equivalent model. From (4.15), the battery model can be recast as ([76, 77]):

$$\begin{aligned} \dot{\mathbf{x}}_B(t) &= \mathbf{A}_B \cdot \mathbf{x}_B(t) + \mathbf{B}_B \cdot u_B(t) \\ \mathbf{y}_B(t) &= \mathbf{C}_B \cdot \mathbf{x}_B(t) + \mathbf{D}_B \cdot u_B(t) + E_B \end{aligned} \quad (4.19)$$

where:

$$\mathbf{A}_B = \begin{pmatrix} -\frac{1}{\tau_s^B} & 0 & 0 \\ 0 & -\frac{1}{\tau_f^B} & 0 \\ 0 & 0 & 0 \end{pmatrix} \quad (4.20)$$

$$\mathbf{B}_B = \left(\frac{1}{C_s^B} \quad \frac{1}{C_f^B} \quad \frac{-1}{C_{SOC}^B} \right)^T \quad (4.21)$$

$$\mathbf{C}_B = \begin{pmatrix} -1 & -1 & \alpha_{oc} \\ 0 & 0 & 1 \end{pmatrix} \quad (4.22)$$

$$\mathbf{D}_B = \left(-R_{ss}^B \quad 0 \right)^T \quad (4.23)$$

$$\mathbf{E}_B = \left(\beta_{oc} \quad 0 \right)^T \quad (4.24)$$

An example of battery system respond to impulsive current profile is shown in Fig. 4.7.

4.4.1.3. State-of-Health (SOH)

SOH is a performance feature of an accumulation device and is defined as the ratio between the current battery capacity and the capacity of a fresh cell (typically provided by the manufacturer). *SOH* ranges between 0 and 1. Degradation effects are related to internal battery chemical reactions and spurious side reactions that reduce the active chemical reagents. From the electrical point of view, many causes concur to decrease *SOH*: over-voltage, over-current, over-temperature are the main important ones, but many others can be considered, such as: the number of charge-discharge

cycles, depth-of-discharge, calendar life and so on [83]. Different degradation models have been formulated for different battery types and usage.

Many experimental studies have addressed the over-voltage as the most significant cause of UC life degradation ([78, 84, 85]). At highest UC operative voltage, it has been observed that the decomposition of internal electrolyte is accelerated and more impurities undergo the nominal redox reactions inside the UC [83, 86]. This degrades the UC storage capacity and thus reduces its life. Albeit degradation effects exist, one of the most recognized property is that compared with battery technology, ultracapacitors are able to sustain several thousands of deep discharge and charge cycles without significant degradation of life, provided that they work within their operative voltage limits ([87]).

On the other hand, battery degradation phenomenon is due to a combination of side reactions on both anode and cathode surfaces of battery. Examples of side reactions include Solid Electrolyte Interfaces (SEI) formation, metallic manganese deposition, Ion Hydrogen generation and many others. SEI formation stands out the others to be the most significant cause of battery degradation. It grows between the electrode and the electrolyte solvent and leads to a gradual consumption of the lithium-based reagents and the increment of electrode impedance upon cycling. In a fresh cell, SEI layer is not yet formed, but during the utilization it can grow with a speed that depends on the cycling conditions, temperature and depth of discharge. It is almost impossible to completely revert side reactions in order to recover the battery life, thus it is important to avoid working conditions that encourage the formation of SEI formation. Numerous experiments have been conducted in the literature to investigate the associated stress factors that accelerate this phenomenon. From such studies, it has emerged that degradation effects are strictly related to test conditions (test current peak, internal heat production, time duration of current surging) and battery technology (type of reaction, initial battery age, shape and volume of the battery). As a results, different results can be extracted from the literature ([81, 82, 88, 89]). Capacity degradation can be modelled by radical or exponential equations. In [90, 91, 92, 93], battery SOH (SOH_B in the following) model is derived from the Arrhenius law that has been extended to predict capacity-loss of batteries subjected to complex current profiles.

Denoting with $\Delta SOH_B(\Delta t)$ the battery SOH variation over a timeslot Δt , we have:

$$\Delta SOH_B(\Delta t) = \frac{\Delta C_{SOC}^B}{C_{SOC}^B(0)} = A \cdot \exp\left(-C \frac{E_a^c}{R \cdot T}\right) \cdot \frac{i_B^h \cdot \Delta t}{Q_c} + B \cdot \exp\left(-D \frac{E_a^d}{R \cdot T}\right) \cdot \frac{i_B^l \cdot \Delta t}{Q_d} \quad (4.25)$$

where:

- ΔC_{SOC}^B , $C_{SOC}^B(0)$: battery capacity variation during a timeslot duration of Δt and the initial capacity;

- i_B^h, i_B^l : charging and discharging currents, respectively, such that $i_B = -i_B^h + i_B^l$;
- Q_c, Q_d : parameters related to the charging and discharging current rates;
- $R = 1.38 \cdot 10^{-23} J \cdot K^{-1}$ the Boltzmann's constant, T battery temperature in Kelvin and E_a^c, E_a^d activations energy (in Joule) of battery reactions for charging and discharging phases;
- A, B, C, D : fitting parameters.

The above equation distinguishes between charging and discharging processes and includes exponential and adjustable factors. It is assumed that charging current i_B^h and discharging current i_B^l remain constant during each timeslot Δt . Such model is able to estimate the capacity loss of the battery when is under different charge and discharge rates and thermal conditions. Parameters of (4.25) can be determined from the capacity loss data curve given by the battery manufacturers. Let $\widehat{\Delta SOH}_B$ be the maximum value of the ΔSOH_B . Assuming that i_B^h and i_B^l are upper limited by $i_B^h < \bar{i}_B^h$ and $i_B^l < \bar{i}_B^l$, SOH_B variation over time $n\Delta t$ is $\Delta SOH_B(n\Delta t) < \widehat{\Delta SOH}_B(n\Delta t)$ with $\widehat{\Delta SOH}_B(n\Delta t) = n \cdot \widehat{\Delta SOH}_B(\Delta t)$ and:

$$\begin{aligned} \widehat{\Delta SOH}_B(\Delta t) &= (\alpha_{SOH}^h \cdot \bar{i}_B^h \cdot \Delta t) + (\alpha_{SOH}^l \cdot \bar{i}_B^l \cdot \Delta t) \\ &= \widehat{\Delta SOH}_B^h(\Delta t) + \widehat{\Delta SOH}_B^l(\Delta t) \end{aligned} \quad (4.26)$$

being $\alpha_{SOH}^h = A/Q_c \cdot \exp(-C \frac{E_a^c}{R \cdot T})$ and $\alpha_{SOH}^l = B/Q_d \cdot \exp(-D \frac{E_a^d}{R \cdot T})$, being $\alpha_{SOH}^h, \alpha_{SOH}^l$ in $Coulomb^{-1}$ unit. $\widehat{\Delta SOH}_B^h(\Delta t)$ and $\widehat{\Delta SOH}_B^l(\Delta t)$ are the maximum SOH_B degradations due to a battery recharging and discharging in a timeslot Δt . Notice that in (4.26) $\bar{i}_B^h \cdot \Delta t$ and $\bar{i}_B^l \cdot \Delta t$ are the total average charge during Δt exchanged with the harvesting and the load respectively. Therefore, we define: $\bar{Q}_B^h = \bar{i}_B^h \cdot \Delta t$ and $\bar{Q}_B^l = \bar{i}_B^l \cdot \Delta t$ such quantities and from (4.26) we have: $\widehat{\Delta SOH}_B^h(\Delta t) = \alpha_{SOH}^h \cdot \bar{Q}_B^h$ and $\widehat{\Delta SOH}_B^l(\Delta t) = \alpha_{SOH}^l \cdot \bar{Q}_B^l$.

4.4.2. State-Space model

The state-space model for the system in Fig. 4.2 is composed by the above models. Specifically, let $\mathbf{x}_{sys} = [\mathbf{x}_U \quad \mathbf{x}_B]^T$, $\mathbf{y}_{sys} = [\mathbf{y}_U \quad \mathbf{y}_B]^T$ and $\mathbf{u}_{sys} = [u_U \quad u_B]^T$, from equations (4.10)-(4.19) we have:

$$\begin{aligned} \dot{\mathbf{x}}_{sys} &= \begin{pmatrix} \mathbf{A}_U & \mathbf{0}_{3 \times 3} \\ \mathbf{0}_{3 \times 3} & \mathbf{A}_B \end{pmatrix} \cdot \mathbf{x}_{sys} + \begin{pmatrix} \mathbf{B}_U & \mathbf{0}_{3 \times 1} \\ \mathbf{0}_{3 \times 1} & \mathbf{B}_B \end{pmatrix} \cdot \mathbf{u}_{sys} \\ \mathbf{y}_{sys} &= \begin{pmatrix} \mathbf{C}_U & \mathbf{0}_{2 \times 3} \\ \mathbf{0}_{2 \times 3} & \mathbf{C}_B \end{pmatrix} \cdot \mathbf{x}_{sys} + \begin{pmatrix} \mathbf{0}_{2 \times 1} & \mathbf{0}_{2 \times 1} \\ \mathbf{0}_{2 \times 1} & \mathbf{D}_B \end{pmatrix} \cdot \mathbf{u}_{sys} + \begin{pmatrix} \mathbf{0}_{2 \times 1} \\ \mathbf{E}_B \end{pmatrix} \end{aligned} \quad (4.27)$$

Then, the zero-order hold discretization of the state-space model (4.27) is calculated, resulting in the complete discrete state-space model of the system:

$$\begin{aligned} \mathbf{x}_{\text{sys}}(k+1) &= \overbrace{\begin{pmatrix} \Phi_U & \mathbf{0}_{3 \times 3} \\ \mathbf{0}_{3 \times 3} & \Phi_B \end{pmatrix}}^{\mathbf{A}_{\text{sys}}} \cdot \mathbf{x}_{\text{sys}}(k) + \overbrace{\begin{pmatrix} \Gamma_U & \mathbf{0}_{3 \times 1} \\ \mathbf{0}_{3 \times 1} & \Gamma_B \end{pmatrix}}^{\mathbf{B}_{\text{sys}}} \cdot \mathbf{u}_{\text{sys}}(k) \\ \mathbf{y}_{\text{sys}}(k) &= \overbrace{\begin{pmatrix} \mathbf{C}_U & \mathbf{0}_{2 \times 3} \\ \mathbf{0}_{2 \times 3} & \mathbf{C}_B \end{pmatrix}}^{\mathbf{C}_{\text{sys}}} \cdot \mathbf{x}_{\text{sys}}(k) + \overbrace{\begin{pmatrix} \mathbf{0}_{2 \times 1} & \mathbf{0}_{2 \times 1} \\ \mathbf{0}_{2 \times 1} & \mathbf{D}_B \end{pmatrix}}^{\mathbf{D}_{\text{sys}}} \cdot \mathbf{u}_{\text{sys}}(k) + \overbrace{\begin{pmatrix} \mathbf{0}_{2 \times 1} \\ \mathbf{E}_B \end{pmatrix}}^{\mathbf{E}_{\text{sys}}} \end{aligned} \quad (4.28)$$

In (4.28), matrices Φ_U, Φ_B, Γ_U and Γ_B are obtained from the zero-order hold discretization of the continuous state-space model (4.27).

Notice that from (4.6), control variables $\mathbf{u}_{\text{sys}}(k)$ can be written as function of $\boldsymbol{\lambda}(k) = [\lambda_1(k) \ \lambda_2(k) \ \lambda_3(k) \ \lambda_4(k)]^T$ by:

$$\mathbf{u}_{\text{sys}}(k) = \begin{pmatrix} -\hat{u}_h & 0 & \hat{u}_l & 0 \\ 0 & -\hat{u}_h & 0 & \hat{u}_l \end{pmatrix} \cdot \boldsymbol{\lambda}(k) \quad (4.29)$$

Remark With this system model formulation, a control strategy on variables $\lambda_1, \lambda_2, \lambda_3, \lambda_4$ is able to manage the recharge of the ultracapacitor and the battery from harvesting, and it is able also to control $\delta = \lambda_3 + \lambda_4$ during each timeslot.

4.5. Energy management strategies development

In this section, control strategies aimed to preserve battery from capacity degradation and to cope with load requirements will be formulated. In the discrete state-space model (4.28), control vector $\boldsymbol{\lambda}(k) = [\lambda_1(k) \ \lambda_2(k) \ \lambda_3(k) \ \lambda_4(k)]^T$ will be used.

Firstly an MPC-based control according to proposed in Sec. 4.3 is formulated. Despite of the advantages derived by its predictive behaviour, the MPC-based controller is computational demanding and this may constrain its use in EH-WSN applications. For this reason, two rule-based strategies, namely *threshold-based strategy* and *adaptive strategy*, are also proposed. Threshold-based strategy is commonly adopted in hybrid management systems (e.g. [70]). Additionally, we propose a variant of the threshold-based strategy, named *adaptive*, that manages the hybrid system energy also by using information about the estimated energy harvesting resource available in the future.

4.5.1. MPC-based energy management strategy

The following optimization cost function $J_N(k)$ is considered:

$$J_N(k) = \sum_{n=k}^{k+N-1} \left(\omega_h (u_h\{n,k\} - \widehat{u}_h(n))^2 + \omega_l (u_l\{n,k\} - \widehat{u}_l)^2 + \omega_B \Delta SOH_{B\{n,k\}}^2 \right) \quad (4.30)$$

being N the prediction horizon. The first cost term maximizes the renewable energy, harvested into the hybrid system. Notice that $u_h\{n,k\} = \widehat{u}_h(n)$ is equivalent to have $\lambda_{1\{n,k\}} + \lambda_{2\{n,k\}} = 1$. The second cost term copes with the load demand. Notice that $u_l\{n,k\} = \widehat{u}_l$ is equivalent to $\delta = \lambda_{3\{n,k\}} + \lambda_{4\{n,k\}} = 1$. Finally, the third cost term is aimed to minimize the battery SOH degradation over time. At each k the MPC-based control solves the following optimization problem:

$$\begin{aligned} \min_{\mathbf{U}_{\{k\}}} \quad & J_N(\mathbf{x}_k, \mathbf{U}_{\{k\}}) \\ \text{s.t.} \quad & \mathbf{x}_{\text{sys}\{n+1,k\}} = \mathbf{A}_{\text{sys}} \cdot \mathbf{x}_{\text{sys}\{n,k\}} + \mathbf{B}_{\text{sys}} \cdot \mathbf{u}_{\text{sys}\{n,k\}} \quad (a) \\ & \mathbf{y}_{\text{sys}\{n,k\}} = \mathbf{C}_{\text{sys}} \cdot \mathbf{x}_{\text{sys}\{n,k\}} + \mathbf{D}_{\text{sys}} \cdot \mathbf{u}_{\text{sys}\{n,k\}} + \mathbf{E}_{\text{sys}} \quad (b) \\ & u_U\{n,k\} = \lambda_{1\{n,k\}} \widehat{u}_h(n) - \lambda_{3\{n,k\}} \widehat{u}_l \quad (c) \\ & u_B\{n,k\} = \lambda_{2\{n,k\}} \widehat{u}_h(n) - \lambda_{4\{n,k\}} \widehat{u}_l \quad (d) \\ & \mathbf{y}_{\text{sys}}^{\text{inf}} \leq \mathbf{y}_{\text{sys}\{n,k\}} \leq \mathbf{y}_{\text{sys}}^{\text{sup}} \quad (e) \\ & \Delta SOH_{B\{n,k\}} \leq \widehat{\Delta SOH}_B(\Delta t) \quad (f) \\ & \lambda_{1\{n,k\}}, \lambda_{2\{n,k\}}, \lambda_{3\{n,k\}}, \lambda_{4\{n,k\}} \in [0, 1] \quad (g) \\ & \lambda_{1\{n,k\}} + \lambda_{2\{n,k\}} \leq 1 \quad (h) \\ & \lambda_{3\{n,k\}} + \lambda_{4\{n,k\}} \leq 1 \quad (i) \\ & \mathbf{x}_{\text{sys}\{k,k\}} = \mathbf{x}_{\text{sys}}(k) \quad (j) \end{aligned} \quad (4.31)$$

Constraints (4.31).(a) to (4.31).(d) refer to discrete system model of the hybrid system. (4.31).(e) constrains the output system, and in particular $\mathbf{y}_{\text{sys}}^{\text{inf}}$, $\mathbf{y}_{\text{sys}}^{\text{sup}}$ are the lower and the upper output system constraint vectors, respectively. (4.31).(f) attempts to limit battery SOH degradation at each optimization discrete time n . $\widehat{\Delta SOH}_B(\Delta t)$ is the upper limit of battery degradation over a timeslot Δt and can be selected on the basis of the desired battery lifetime. To note that Δt is the considered sample time. An example of $\widehat{\Delta SOH}_B(\Delta t)$ dimensioning will be given in Sec. 4.6. Equations from (4.31).(g) to (4.31).(i) constrain control variables. Finally (4.31).(j) is the initial condition at time slot k .

4.5.2. Threshold-based energy management strategy

Many works in literature (e.g. [70]) propose a simple strategy to control ultracapacitor and battery usage. The main actor of energy management is the ultracapacitor, while the battery is used as

reservoir that is recharged if ultracapacitor is full or is discharged when the ultracapacitor is empty. This way, the use of battery is reduced and its degradation effects are limited. Such strategy applied to the proposed hybrid system in Fig. 4.2 should be formulated for both input variables (λ_1 and λ_2) and output variables (λ_3 and λ_4). Its behaviour is hereafter summarized:

- Recharge the ultracapacitor until it is full of charge. Then, recharge the battery, until it is full of charge. If both devices are full, harvesting energy is no longer stored into the system.
- the load is principally supplied by the ultracapacitor, until it is out of charge. Then, switch to supply load with battery. If both battery and ultracapacitor are out of charge, disconnect from the output.

Algorithm 1 *Threshold-based strategy*

```

1:  $k = 1$ 
2: loop
3:   {STATE OF CHARGE EVALUATION}
4:    $Q_h(k) \leftarrow$  Provided harvesting charge
5:    $Q_l(k) \leftarrow$  Required node charge
6:    $Q_U(k) \leftarrow$  Level of charge of UC
7:    $Q_B(k) \leftarrow$  Level of charge of BA
8:    $R_U(k) = Q_U^{max} - Q_U(k) \leftarrow$  Charge required to have UC at full of charge
9:    $R_B(k) = Q_B^{max} - Q_B(k) \leftarrow$  Charge required to have BA full of charge
10:
11:   { $\lambda_1(k)$  AND  $\lambda_2(k)$  ALLOCATION}
12:    $\lambda_1(k) = \min\left(\left[\frac{R_U(k)}{Q_h(k)}, 1\right]\right)$ 
13:    $\lambda_2(k) = 1 - \lambda_1(k)$ 
14:    $\lambda_2(k) = \min\left(\left[\lambda_2(k), \frac{R_B(k)}{Q_h(k)}\right]\right)$ 
15:
16:   { $\lambda_3(k)$  AND  $\lambda_4(k)$  ALLOCATION}
17:    $\lambda_3(k) = \min\left(\left[\frac{Q_U(k)}{Q_l(k)}, 1\right]\right)$ 
18:    $\lambda_4(k) = 1 - \lambda_3(k)$ 
19:    $\lambda_4(k) = \min\left(\left[\lambda_4(k), \frac{Q_B(k)}{Q_l(k)}\right]\right)$ 
20:
21:   {APPLY  $\lambda_1(k), \lambda_2(k), \lambda_3(k), \lambda_4(k)$ }
22:    $k = k + 1$ 
23: end loop (INFINITE LOOP)

```

Pseudo-code of threshold-based strategy is summarized in Algorithm 1. At each timeslot, a set of data is preliminary collected: a. the average level of charge provided during the current timeslot $Q_h(k) = \hat{u}_h(k) \cdot \Delta t$; b. the expected charge required by the node for the next timeslot $Q_l(k) = \hat{u}_l(k) \cdot \Delta t$; c. levels of charge of battery ($Q_B(k)$) and ultracapacitor ($Q_U(k)$). At lines 8-9, $R_U(k)$ and $R_B(k)$ represent the charge required to have at full of charge the Ultracapacitor and the battery,

respectively. At line 12, it is evaluated $\lambda_1(k)$ considering that the charge to be stored is $Q_h(k)$ and cannot be greater than $R_U(k)$. Similar rules are followed to allocate $\lambda_3(k)$ and $\lambda_4(k)$. In particular, $\lambda_3(k)$ (line 17) is evaluated considering that the charge to be delivered to node is $Q_I(k)$, but cannot exceed the current ultracapacitor level of charge, $Q_U(k)$. Same consideration is applied on $\lambda_4(k)$ (line 19), provided that $\lambda_3(k) < 1$, otherwise $\lambda_4(k) = 0$.

4.5.3. Adaptive energy management strategy

The adaptive strategy manages the hybrid system energy also by using information on the expected energy harvesting resource in the future. As in the MPC-based controller case, also in this case the energy autonomy of node is prolonged by controlling the node duty cycle. Let define for each k

Algorithm 2 Adaptive strategy

```

1:  $k = 1$ 
2: loop
3:   {STATE OF CHARGE EVALUATION}
4:    $Q_h(k) \leftarrow$  Provided harvesting charge
5:    $Q_I(k) \leftarrow$  Required node charge
6:    $Q_U(k) \leftarrow$  Ultracapacitor level of charge
7:    $Q_B(k) \leftarrow$  Battery level of charge
8:    $R_U(k) = Q_U^{max} - Q_U(k) \leftarrow$  Charge required to have UC at full of charge
9:    $R_B(k) = Q_B^{max} - Q_B(k) \leftarrow$  Charge required to have BA at full of charge
10:   $\langle Q_h \rangle_k \leftarrow$  Expected mean harvesting charge over  $N$  timeslot horizon
11:
12:  {ESTIMATE DUTY CYCLE}
13:   $\delta(k) = \min\left(\left[\frac{\langle Q_h \rangle_k}{Q_I(k)}, 1\right]\right)$ 
14:
15:  { $\lambda_1(k)$  AND  $\lambda_2(k)$  ALLOCATION}
16:   $\lambda_1(k) = \min\left(\left[\frac{R_U(k)}{Q_h(k)}, 1\right]\right)$ 
17:   $\lambda_2(k) = 1 - \lambda_1(k)$ 
18:   $\lambda_2(k) = \min\left(\left[\lambda_2(k), \frac{R_B(k)}{Q_h(k)}, \frac{\bar{Q}_B^h}{Q_h(k)}\right]\right)$ 
19:
20:  { $\lambda_3(k)$  AND  $\lambda_4(k)$  ALLOCATION}
21:   $\lambda_3(k) = \min\left(\left[\frac{Q_U(k)}{Q_I(k)}, \delta(k)\right]\right)$ 
22:   $\lambda_4(k) = \delta(k) - \lambda_3(k)$ 
23:   $\lambda_4(k) = \min\left(\left[\lambda_4(k), \frac{Q_B(k)}{Q_I(k)}, \frac{\bar{Q}_B^l}{Q_I(k)}\right]\right)$ 
24:
25:  {APPLY  $\lambda_1(k), \lambda_2(k), \lambda_3(k), \lambda_4(k)$ }
26:   $k = k + 1$ 
27: end loop (INFINITE LOOP)

```

the expected average energy harvested over a receding horizon N , $\langle Q_h \rangle_k = \frac{1}{N} \sum_{n=k}^{k+N-1} Q_h(n)$. Node

rate is allocated through equation $\delta(k) = \min([\frac{\langle Q_h \rangle_k}{Q_l(k)}, 1])$. If harvesting energy is greater than the maximum load demand, $\delta = 1$). Vice-versa, δ is set such that the average node consumption ($\delta Q_l(k)$) equals the average energy harvesting $\langle Q_h \rangle_k$.

Additionally, battery current is limited in both the charge and the discharge to reduce degradation effects when battery is used. In particular, being from eq. (4.26) $\widehat{\Delta SOH}_B^h$ and $\widehat{\Delta SOH}_B^l$ the maximum SOH_B degradation due to recharge and discharge currents respectively, it can be defined with $\overline{Q}_B^h = \frac{\widehat{\Delta SOH}_B^h}{\alpha_{SOH}^h}$ and with $\overline{Q}_B^l = \frac{\widehat{\Delta SOH}_B^l}{\alpha_{SOH}^l}$ limitation on exchanged charge during time Δt . Then, one can allocate $\lambda_2(k)$ and $\lambda_4(k)$ such that $Q_B^h < \overline{Q}_B^h$ and $Q_B^l < \overline{Q}_B^l$ at each k .

Pseudo-code for the adaptive strategy is reported in Algorithm 2. As for Algorithm 1, at each timeslot the following set of data $Q_h(k), Q_l(k), Q_U(k), Q_B(k), R_U(k), R_B(k), \langle Q_h \rangle_k$ is collected (lines from 4 to 10) is collected. Duty cycle evaluation is reported on line 13. The allocation of $\lambda_1(k)$ and $\lambda_2(k)$ (lines 16 to 18) is similar to the threshold-based case, with the exception at line 18, where the usage of battery for the recharge is limited by \overline{Q}_B^h , for the battery preservation purpose. The allocation of $\lambda_3(k)$ and $\lambda_4(k)$ (lines from 21 to 23) follow the same considerations given for the threshold-based case, but with two innovative differences: a) $\lambda_3(k) \leq \delta(k)$ and $\lambda_4(k) = \delta(k) - \lambda_3(k)$; b) $\lambda_4(k)$ is allocated taking into account the hard limits on battery charge to the load \overline{Q}_B^l in order cope with the SOH degradation.

4.5.4. Controller performances

In order to validate and compare the above control strategies, in this section three performance metrics are introduced: 1) the harvesting utilization index, ρ_h , 2) the node duty cycle allocation index, ρ_l , and 3) the battery degradation index, ρ_B .

Harvesting utilization index ρ_h is the percentage of harvesting charge that has been stored into the hybrid system:

$$\rho_h = \left(\frac{u_h}{\widehat{u}_h} \cdot 100 \right) \% \quad (4.32)$$

Node allocation index Similarly, ρ_l is the node active fraction $\delta = \lambda_3 + \lambda_4$ expressed in percentage:

$$\rho_l = \left(\frac{u_l}{\widehat{u}_l} \cdot 100 \right) \% \quad (4.33)$$

Ultracapacitor model	Value	Battery model	Value
R_s^U	$1.07 \cdot 10^3 \Omega$	R_s^B	$1.07 \cdot 10^{-3} \Omega$
C_s^U	$8.2 \cdot 10^{-1} F$	C_s^B	$7.00 \cdot 10^2 F$
R_m^U	$4.01 \cdot 10^2 \Omega$	R_f^B	$1.07 \cdot 10^{-3} \Omega$
C_m^U	$3.16 \cdot 10^{-1} F$	C_f^B	$5.24 \cdot 10^{-4} F$
R_f^U	$4.5 \cdot 10^{-2} \Omega$	R_{ss}^B	$7.44 \cdot 10^{-2} \Omega$
C_f^U	$5.0 \cdot 10^1 F$	C_{SOC}^B	$3.00 \cdot 10^2 F$
R_l^U	$9.50 \cdot 10^4 \Omega$	α_{oc}	$3.72 \cdot 10^{-1} V$
		β_{oc}	$3.35 \cdot 10^0 V$
		α_{SOH}^h	$4.2 \cdot 10^{-5} V$
		α_{SOH}^l	$4.2 \cdot 10^{-5} V$

Table 4.1.: Hybrid System model parameters.

Battery degradation index ρ_B measure the overall degradation of the battery. We have:

$$\rho_B = \log(SOH_B) \quad (4.34)$$

Since at initial state $SOH_B = 1$, then $\rho_B = 0$. ρ_B is given as a logarithmic function of SOH_B , because degradation effects are typically very small in magnitude, especially if they are evaluated over short time scales.

4.6. Simulation validation

In this section, the hybrid system strategies are validated by simulative investigations. Throughout the section, it will be assumed that the harvesting block H in Fig. 4.2 is a solar source. Much literature is dedicated to model solar harvesting dynamic over hourly time scale, day of the year and geographic coordinates ([94, 95]). In particular, is used for this simulation model proposed in [96]. In particular, it is considered an ultracapacitor of 50F capacity and a Li-Ion battery of 350mAh capacity. Parameters of the ultracapacitor and the battery are given in Table 4.1 ([97]).

It is conventionally assumed both by manufacturer documentation and in literature that battery end life is when SOH_B drops below 0.8. Basing on this, $\widehat{\Delta SOH}_B(\Delta t)$ can be then designed as follows. Let τ_B be the desired battery lifetime, we have $\widehat{\Delta SOH}_B(\tau_B) = 0.2$. Battery degradation is a quasi-linear process ([97]) and therefore, it results:

$$\widehat{\Delta SOH}_B(\Delta t) = \widehat{\Delta SOH}_B(\tau) \frac{\Delta t}{\tau} = 0.2 \frac{\Delta t}{\tau} \quad (4.35)$$

For simulated scenarios we have: $\Delta t = 30$ minutes, $\tau = 10$ years and $\widehat{\Delta SOH}_B(\Delta t) = 1.16 \cdot 10^{-6}$. Simulations are carried out under Matlab environment. Moreover, MPC-based strategy is simulated with IPOPT (Interior Point OPTimizer) solver operating under YALMIP interface. The mathematical details of IPOPT can be found in several publications, such as ([98, 99]).

In what follows, the presented control strategies will be tested under two different scenarios:

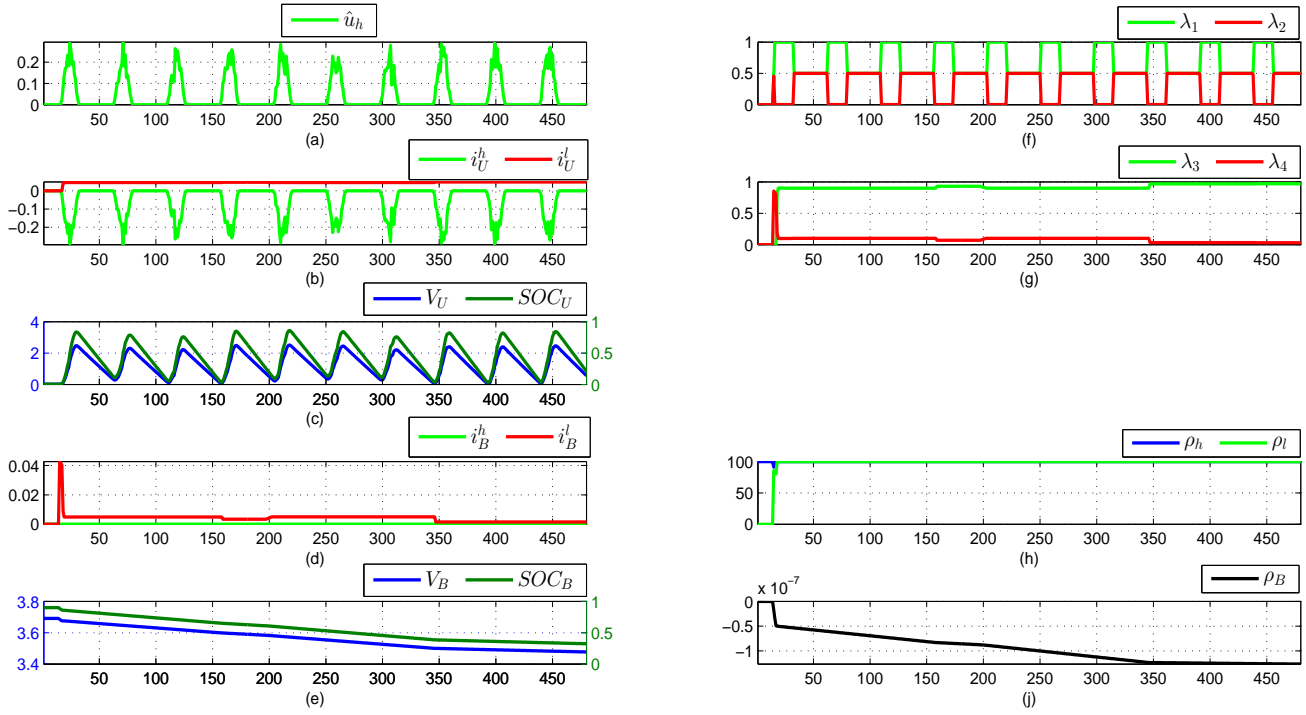


Figure 4.8.: MPC-based strategy, simulation of the first scenario: (a) solar current profile \hat{u}_h ; (f) and (g) optimal decision variables; (b) and (c) input current and outputs of ultracapacitor; (d) and (e) input current flow and outputs of battery; (h) Harvesting rate utilization index ρ_h and node allocation index ρ_l ; (j) Battery degradation index ρ_B over simulation time.

1. the energy resource is able to sustain the node in full operative mode ($\delta = 1$) for 10 days.
2. the available energy is less than the overall node requirement in full operative mode ($\delta = 1$).

Latter scenario emphasizes the effectiveness of predictive controllers to allocate present energy resources in order to guarantee continuous supply autonomy on the future.

The provided simulation plots (Figs. 4.8 - 4.9 - 4.10 - 4.11 - 4.12 - 4.13) will be organized as follows. Results are spread out onto 9 subplots, numbered from letter (a) to (j).

In subplots (a) the applied input solar profile \hat{u}_h over a time horizon of 10 days is reported.

Hybrid system variables dynamic is shown in subplots from letter (b) to (e). Specifically, inputs and outputs of ultracapacitor and of battery are provided in subplots (b)-(c) and subplots (d)-(e), respectively. In subplots (b) (resp. subplots (d)) we distinguish in green the current contributions $-i_U^h$ (resp. $-i_B^h$) from the harvesting system, and in red the load current contributions i_U^l (resp.

MPC parameters	Value	MPC constraints	Value
ω_h	20	SOC_U	$\in [0; 1]$
ω_l	1	SOC_B	$\in [0.2; 0.8]$
ω_B	$1 \cdot 10^7$	V_U	$\in [0; 2.85]V$
\hat{u}_l	$5 \cdot 10^{-2}A$	V_B	$\in [3.43; 3.69]V$
Δt	30 min	i_U	$3.00 \cdot 10^2 F$
N	144	α_{oc}	$3.72 \cdot 10^{-1}V$
		β_{oc}	$3.35 \cdot 10^0 V$
		$\widehat{\Delta SOH}_B(\Delta t)$	$1.16 \cdot 10^{-6}$

Table 4.2.: MPC setup parameters.

i_B^l). Voltage drops and the SOCs of ultracapacitor and the battery are given in subplots (d) and (e) respectively.

The optimal control sequence λ_1 - λ_2 on harvesting input and λ_3 - λ_4 on load output are respectively shown in subplots (f) and (g).

Performance indexes are subplots (h) and (j) and, in particular, in (h) the harvesting rate utilization index ρ_h and the node duty cycle allocation index ρ_l are plotted, while in (j) battery degradation index ρ_B over the simulation time period is shown.

4.6.1. MPC-based energy management strategy

For this simulation, control parameters and cost coefficients are summarized in Table 4.2. In particular, simulations cover a time period of 10 days. The selection of prediction horizon N trade-offs between elaboration time and control performance. After having carried out extensive simulation tests with different N , our choice falls into $N = 144$ that corresponds to 3 days on continuous time scale (being $\Delta t = 30$ minutes).

First scenario Simulation results of the first scenario are shown in Fig. 4.8. For this simulation, we consider the solar harvesting profile in Fig. 4.8.(a). From Fig. 4.8.(c)-(e) it appears that ultracapacitor is subject to daily charge and discharge cycles, while the battery SOC slowly changes. Indeed, optimized control profiles (Figs. 4.8.(f)-(g)) mainly recharge the ultracapacitor (green line in Fig. 4.8.(b)) while battery is not charged (green line in Fig. 4.8.(d)). The optimizer choice is justified by the fact that solar current in this scenario suffices to recharge the ultracapacitor within its voltage and SOC constraints ($V_U \in [0, 2.7]$ and $SOC_U \in [0, 1]$) even when node works at the highest $\delta = 1$). Then, any recharge operation of the battery would only reduce its SOH_B , without beneficial effects on other performances.

Moreover, let consider days 5-6-7 (corresponding to timeslots from 150 to 300). During this period solar current generation slightly reduces as it results from Fig. 4.8.(a). To fulfil the requirements of the load and to relieve the ultracapacitor working within its operative ranges, the control increases

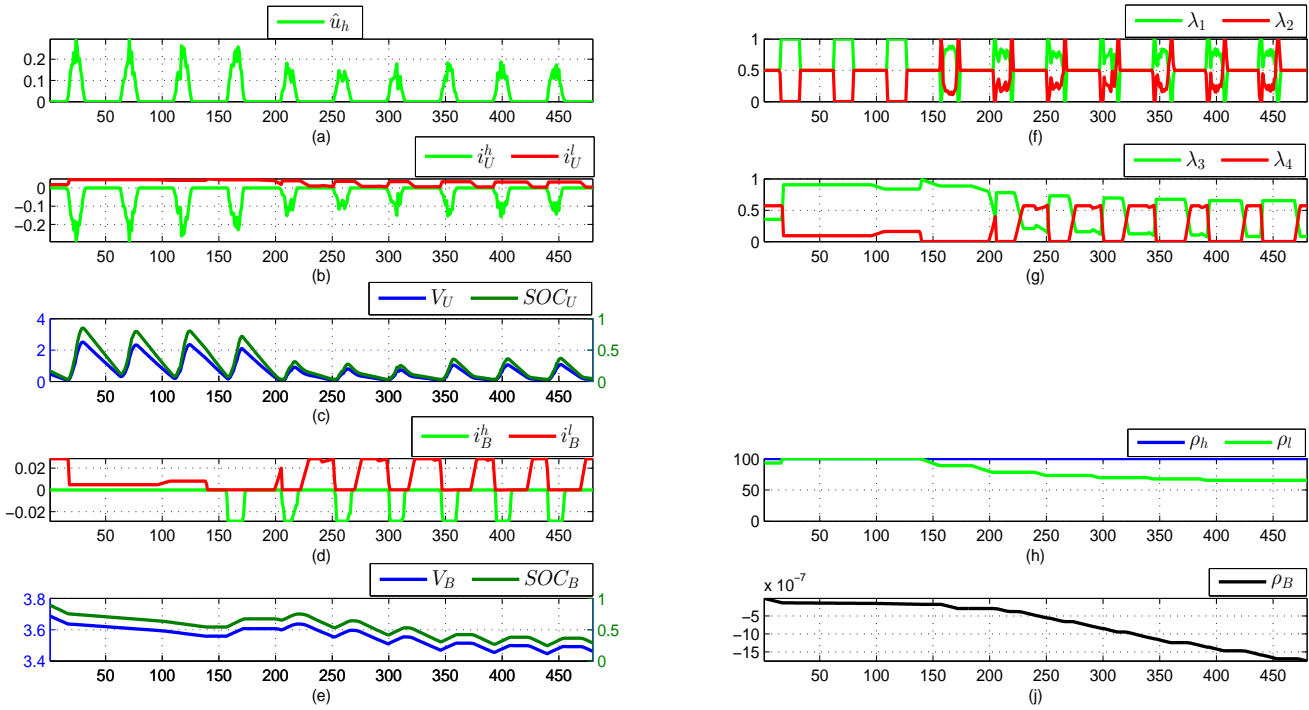


Figure 4.9.: MPC-based strategy, simulation of the second scenario.

the battery current demand (Fig. 4.8.(g)). This condition holds until harvesting current returns to be fully available to the input (timeslot 350). Notice that throughout the simulation, battery supplies the load node with a slight current flow, such that degradation effects are negligible.

Second scenario Simulation results of second scenario are shown in Fig. 4.9. In this case, a lower level of solar current generation is provided as it results from Fig. 4.9.(a). From Figs. 4.9(c) (and λ_3 from 4.9(g)), up to the fourth day (from timeslot 0 to 200) ultracapacitor is able to fully supply the node with a small aid from the battery. However, when solar current reduces (from the fifth day ahead) and the ultracapacitor voltage ripples down to zero the battery is used more frequently. Predictive control action reduces node load current on the basis of solar harvesting resource and, therefore, the related ρ_l decreases (Fig. 4.9.(h)).

Notice that, in lack of energy resource to supply node, model predictive control reduces the duty cycle in order to fulfil hard constraints on system feasibility. Green curve in Fig. 4.9.(g) is obtained by taking into account that in future timeslots the duty cycle should also be maximized.

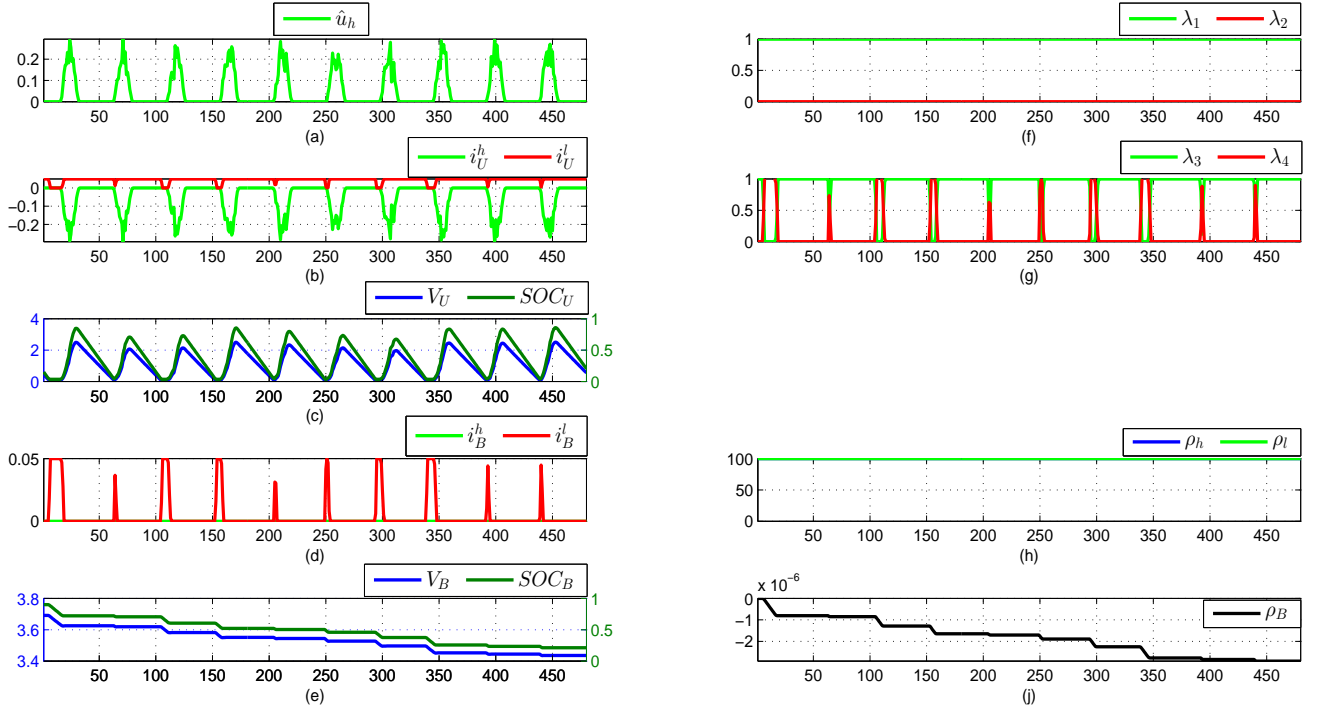


Figure 4.10.: Threshold-based energy management strategy: simulation of first scenario.

4.6.2. Threshold-based energy management strategy

In this section, the simulation results under the threshold-based strategy will be simulated.

First scenario Simulation results of the first scenario are shown in Fig. 4.10. From Fig. 4.10.(c) and (e) we can note that ultracapacitor is mainly used both for charging and discharging, while battery usage is limited to few periods of time, and in particular when (Fig. 4.10.(d)) the ultracapacitor is fully discharged. However, since battery SOH is not taken into account by this strategy, the node is at full operation mode ($\delta = 1$, i.e. $\hat{u}_l = 50mA$) also when battery is used, resulting that battery is subjected to relevant degradation effects when used. Surprisingly, the SOH_B is not well preserved (ρ_B in Fig. 4.10.(j)) compared with 4.8.(j)).

Second scenario In this simulation scenario, we consider the same solar harvesting profile (Fig. 4.9.(a)) and the same initial conditions on battery and ultracapacitor of the previous simulations. After that both the ultracapacitor and the battery have exhausted their energy (from timeslot 280 ahead in Fig. 4.11.(e)), the hybrid system is not able to supply the node. Therefore, $\rho_l = 0$ (i.e.

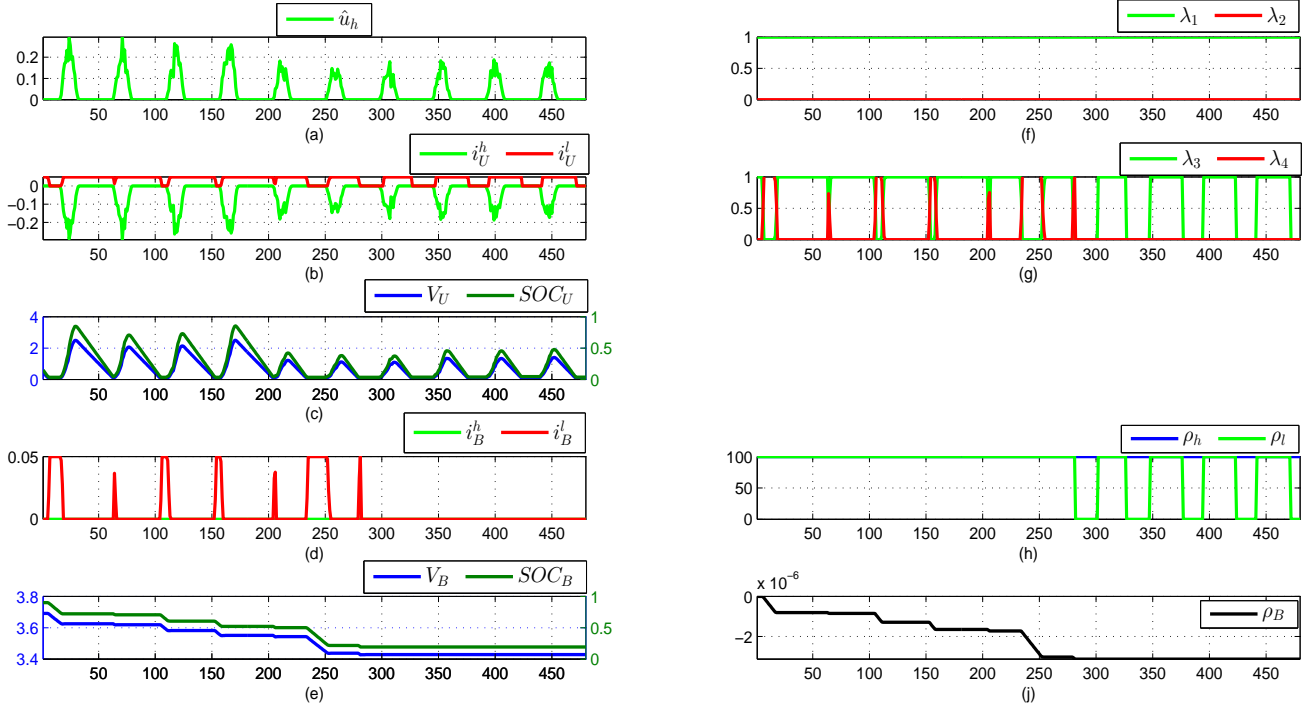


Figure 4.11.: Threshold-based energy management strategy: simulation of second scenario.

$\delta = 0$) during many dark hours to turn back to $\rho_l = 1$ when harvesting current partially recharges the ultracapacitor, as shown in Fig. 4.11.(h) (green line). Consequently, node is continuously switched off for many hours before to start working again, resulting that ρ_l performance is low. Moreover, battery performances are degrades due to repetitive and relatively deep current peaks, resulting in a lower battery SOH. Finally, it is worth noting that battery is completely discharged after six days of operations.

4.6.3. Adaptive energy management strategy

In the following, we will present the simulation results from the adaptive strategy. For this simulation, we set $N = 144$ timeslots, $\bar{Q}_B^h = 0.3$ and $\bar{Q}_B^l = 0.5571$. Comments to simulations are hereafter given.

First scenario Simulation results of first scenario are shown in Fig. 4.12. Also in this case, simulation shows that the ultracapacitor is mainly used, while battery is used to supply the load only when ultracapacitor is fully discharged, as shown in Fig. 4.12.(d). However, to fulfil the

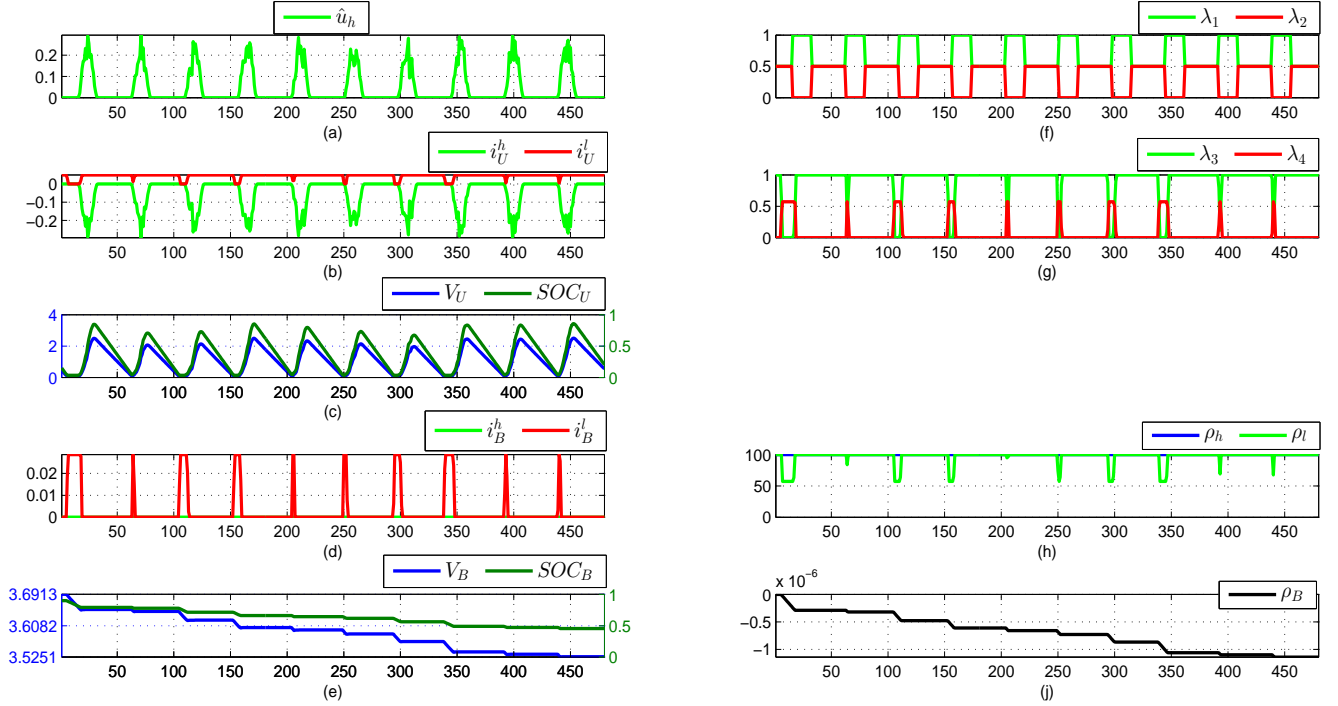


Figure 4.12.: Adaptive energy management: simulation of the first scenario.

hard limitation related to SOH_B (\bar{Q}_B^l), i_B^l is limited, as it results from the comparison between Fig. 4.12.(d) and Fig. 4.10.(d). In accordance with current battery limitations, when battery is used, node duty cycle index ρ_l decreases (Fig. 4.12.(h)). Notice that maximum peak current in Fig. 4.10.(d) equals in magnitude the peak current from the MPC-based, as shown in Fig. 4.9.(d).

Second scenario Simulation results of second scenario are shown in Fig. 4.13. In this case, the effect of δ regulation is emphasized. Indeed, when energy harvesting is low, ρ_l reduces to 61% (Fig. 4.13.(h)), that is similar to the value reached by ρ_l under the MPC-based strategy (Fig. 4.9.(h)). Notice that being ρ_l reduced, the energy autonomy of node is extended in respect to the threshold-based strategy. Indeed, at the end of simulation, the battery is not fully discharged (Fig. 4.13.(e)) and node is supplied continuously with $\delta > 0$ (Fig. 4.13.(h)) differently by the threshold-based case (Figs. 4.11.(e) and 4.11.(h)).

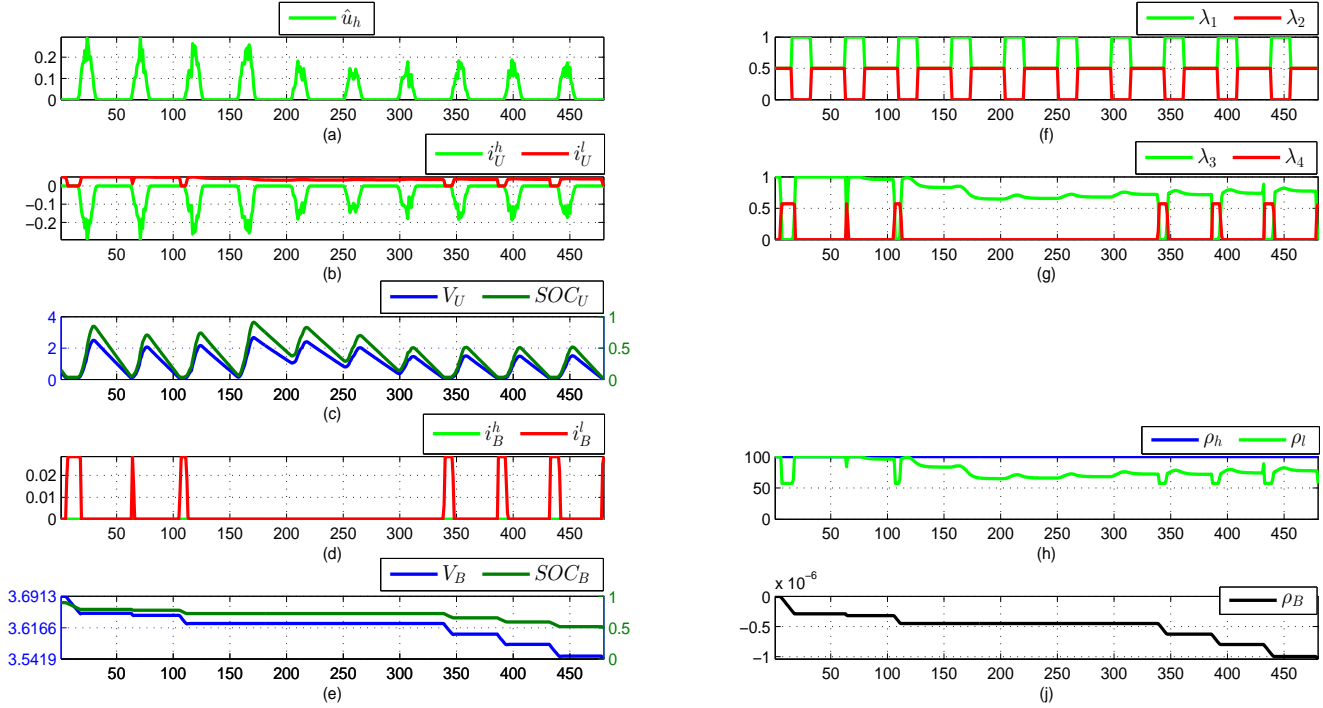


Figure 4.13.: Adaptive energy management: simulation of the second scenario.

4.6.4. Performance comparison and remarks

In Table 4.3 a performance comparison of the above simulations of both the first (a) and the second (b) scenarios is given. We have shown the average value of ρ_h and ρ_l , shortly $ave(\rho_h)$ and $ave(\rho_l)$, and the final battery SOH degradation, namely ρ_{B_∞} .

The following comments can be given:

- MPC-based controller outperforms the other controllers. Notice that in the first scenario, the threshold-based strategy obviously achieves the maximum node duty cycle ($ave(\rho_l) = 100\%$), outperforming the related MPC-based approach performance. However, final SOH_B is in magnitude one order greater than the MPC. Additionally, note that for the second scenario, higher final SOH_B is obtained with the adaptive strategy, rather than the MPC-based approach. However, this happens because in the first case duty cycle allocation is lower than the MPC one.
- Surprisingly, the threshold-based strategy, that should reduce battery degradation, performs the worst final SOH_B . This happens because battery is not upper limited in current usage,

	MPC-based strategy	Threshold-based strategy	Adaptive strategy
$\text{ave}(\rho_h)$	89.49%	89.49%	89.49%
$\text{ave}(\rho_l)$	96.97%	100%	96.63%
ρ_{B_∞}	$-1.26 \cdot 10^{-7}$	$-2.9 \cdot 10^{-6}$	$-1.19 \cdot 10^{-6}$

(a)

	MPC-based strategy	Threshold-based strategy	Adaptive strategy
$\text{ave}(\rho_h)$	89.46%	89.46%	89.45%
$\text{ave}(\rho_l)$	80.69%	82.02%	77.83%
ρ_{B_∞}	$-1.75 \cdot 10^{-6}$	$-3.12 \cdot 10^{-6}$	$-1.1 \cdot 10^{-6}$

(b)

Table 4.3.: Performances comparison of MPC-based, adaptive and threshold-based control strategies for: (a) the first simulation scenario, (b) the second simulation scenario. It is reported: the average values of ρ_h and ρ_l , namely $\text{ave}(\rho_h)$ and $\text{ave}(\rho_l)$, and the final value of SOH_B degradation, ρ_{B_∞} .

but only in time duration usage.

- The proposed adaptive strategy outperforms the threshold-based one, and approximates to the MPC-based strategy in both of the two extreme simulated scenarios.

4.7. Conclusion

In this chapter, the study of a hybrid harvesting supply system for EH-WSN has been proposed. The optimal control of the proposed system is formulated to cope with node supply requirement and battery life preservation. The hybrid system models and the battery degradation model have been taken into account in the MPC controller formulation. Motivated by the fact that MPC controllers may be computationally demanding to be implemented by a micro-controller, a more suitable suboptimal *adaptive* strategy has been devised. Simulation tests of the proposed control laws are carried out in order to compare performances and validate their effectiveness under two realistic harvesting scenarios in comparison with standard threshold-based controller.

Distributed flow control in EH-WSN

5.1. Motivation

IN this chapter, a distributed control law to avoid queue congestion and reduce network power consumption is proposed. Let consider a EH-WSN based monitoring system, consisting of one elaboration node, or *FC*, and a certain number of *leaf nodes* that communicate sensed data to the FC. Multi-hop communication among leaf nodes is adopted to deliver data to FC. Nodes can generate packets and at the same time can route information to the FC node.

If a node is meant to operate indefinitely, node cannot consume in the average more power than the harvesting source can provided. The balance between the average power consumption and the average harvested power is known as the 'energy neutrality condition' ([100], [101]). Power consumption of one node i depends not only on the transmitted data rate but also on the received data rate. Therefore, the neutrality condition at node i is achieved not only by regulating the local generation rate, but also by regulating the generation of such nodes that send information through node i . The communication rate is constrained by channel bandwidth, i.e. the maximum transmission rate at which the receiver is able to correctly decode the symbols. When network is composed of a large number of nodes, and/or under intense traffic scenario, packet loss occurs, leading to dramatically decrease of network throughput [102].

Therefore, it is clear that a flow control procedure not only can relieve the network for queue congestion and packet loss, but it also can guarantee under certain conditions energy neutrality.

In this work, we formulate distributed control taking into account both congestion and power consumption features. The main aim is to avoid congestion and guarantee energy neutrality condition at each node.

5.1.1. Related works

The general formulation of the flow control problem is as follows: find the optimal generation data rate vector \mathbf{g} that maximizes a network utility function $\mathcal{U}(\mathbf{g})$ and ensures that node's incoming data \mathbf{R} not exceeds the available queue capacity \mathbf{c} ([103],[104]). To this aim, it is formulated the following problem:

$$\begin{aligned} \max_{\mathbf{g}} \quad & \mathcal{U}(\mathbf{g}) \\ \text{s.t.} \quad & \mathbf{R} \leq \mathbf{c} \end{aligned} \tag{5.1}$$

In the past decade, much of the research was focused to formulate distributed congestion avoidance controls that dynamically steer the generation rate to converge to optimal solution of the primal problem in (5.1). Such algorithms are widely adopted as congestion control mechanisms in large scale networks ([2],[105]). Example of distributed congestion mechanisms currently adopted on the Internet are Vegas [106] or Reno [107]. Despite of the large amount of such algorithms proposed in literature, the main idea consists on the decomposition of the optimization problem in (5.1) into a primal-dual problem which involves two cooperative mechanisms: a) one dynamic law acting on transport layer that computes a penalty index on the basis of the traffic congestion on node's path; b) one source rate regulation law that sets the transmission rate of source nodes on the basis of the evaluated penalty index.

Although distributed flow control has been formerly used as control algorithm for wired and wireless communication (e.g. the Internet), is recent in literature the study of this distributed control law also in WSN involving power consumption feature.

In [108] the power consumption of wireless node is reduced by distributively choosing the proper routing path in order to balance the power consumptions of nodes. To this aim, the authors adopt a flow optimization problem with constraints on channel capacity and power budget. To distributively implement the proposed optimization problem, a suboptimal solution is considered which divides the WSN into a set of independent sub-networks to significantly reduce the topological complexity.

In [109], the problem of transmission rate limitation due to the electromagnetic channel capacity is addressed in order to maximize the network throughput. Two optimization variables are considered: the generation rate and the transmission power at each node. Node's generation rate is limited by the channel capacity. Since capacity can be increased by using higher transmission power, one can increase the generation rate allocating more transmission power. In counterpart, this may lead to reduce the channel capacity other nodes into the network. To this aim, the author proposes a distributed non linear control algorithm based on Lagrangian dual decomposition technique and channel capacity formula. Robustness of the proposed algorithm in presence of packet

loss and inaccurate estimation of local channel capacity is also pointed out. In [110] authors consider both the flow control at the transport layer and the link scheduling at the MAC layer. The aim is to optimize the throughput subject to rate constraints in presence of stochastic perturbations, due to communication noise. Using the Lagrangian dual decomposition method, they devise a distributed primal-dual algorithm and a convergence analysis is provided in both of deterministic and stochastic environment.

5.1.2. Contribution and chapter outline

In this chapter we propose a flow control law in order to cope with congestion phenomena and energy efficiency in EH-WSN. In particular, a primal optimization problem maximizing data sampling rate and subject to the energy and congestion constraints is formulated. Based on the primal-dual Lagrangian decomposition method, we devise a rate control law that takes into account rate and power consumption variables. For the proposed distributed control law we derive convergence and global asymptotic stability analysis. Specifically, the convergence analysis is based on the primal-dual Lagrangian decomposition, while the global asymptotic stability is demonstrated by Lyapunov arguments, inspired by demonstration carried out in [111]. In our formulation the penalty at each node is given as function of both queue congestion and power consumption.

To prove the effectiveness of the proposed control law, a WSN model is provided and the distributed traffic protocol is implemented over the network. Simulation is carried out by assuming that harvesting conditions change over time. In this chapter we explicitly take into account the energy neutrality condition to cope with EH-WSN autonomy. Differently from [109], we relate the power consumption to the communication rate of node. Additionally, the proposed control law regulates the transmission rate of each node, instead of control the routing path, as it is done in [108].

Another important contribution of this work is the experimental validation on a real small EH-WSN that corroborates the effectiveness of the proposed control law. In this case, data transmission is subject to non-ideal factors, such as delays, dynamic law update delay, packet loss and reduce machine precision of numerical representation. We show that under different energy harvesting levels the experimental steady-state rates will approximate the theoretical equilibrium ones. This validates the stability analysis of the proposed law and its capability to adaptively regulate traffic rate also as function of harvesting energy availability.

The chapter outline is given. In Sec. 5.2 the energy and data traffic WSN model is provided. In Sec. 5.3 the proposed optimal flow control is defined firstly as primal problem, than using the Lagrangian decomposition, the dual model is derived. In Sec. 5.4 a distributed dynamic algorithm is proposed. The convergence and the global asymptotic stability analyses of are presented in Sec.

5.5. Sec. 5.6 shows a simulative scenario where the proposed law is tested under varying solar conditions and finally an experimental test over a small network composed of 5 nodes is carried out in Sec. 5.7. In this section the experimental setup is also detailed. Finally, conclusions are provided in Sec. 5.8.

5.2. Wireless Network definition

5.2.1. Data traffic model

Let \mathcal{G} be a connected and undirected network graph composed of n sensor nodes. Let $i \in N$ with $N = \{1, \dots, n\}$, denotes the generic node of the network. Node i sends data to the FC by a preassigned path of relay nodes denoted with $\Omega(i)$. The routing matrix $\mathbf{L} = \{l(j, i)\} \subset \mathbb{R}^{n \times n}$ will be defined as:

$$l(j, i) = \begin{cases} 1 & \text{if } j \in \Omega(i) \\ 1 & \text{if } j \equiv i \\ 0 & \text{otherwise} \end{cases} \quad (5.2)$$

We will assume in the following of this paper that \mathbf{L} is a full row rank matrix. Let denote with ΔT a small observation time and with k the generic discrete time referred to period $t = [(k-1)\Delta T, k\Delta T]$, with $k \in \mathbb{N}$ and \mathbb{N} being the set of natural numbers. During t , node i generates an average number of sampled data that will be denoted with $g_i(k)$ and referred to as *generation rate*. At the same time, node is also a relay of information for other network nodes, so that the overall average data that it processes over time t is $r_i(t) = \sum_{j \in N} l(i, j)g_j(t)$. $r_i(t)$ is named *aggregate rate* of node i in the following. Notice that $r_i(t)$ is the sum of the incoming packet rate and the generation rate. Additionally, at each node are defined also a positive scalar penalty function $\rho_i(t)$ and an *aggregate price* $q_i(t) = \sum_{j \in N} l(j, i)\rho_j(t)$. In compact form it can be written as:

$$\begin{aligned} \mathbf{R}(t) &= \mathbf{L} \cdot \mathbf{g}(t) \\ \mathbf{q}(t) &= \mathbf{L}^T \cdot \boldsymbol{\rho}(t) \end{aligned} \quad (5.3)$$

where $\mathbf{R}(t) = [r_1(t), \dots, r_n(t)]^T$ and $\mathbf{q}(t) = [q_1(t), \dots, q_n(t)]^T$ for all $i \in N$ are the aggregate rate vector and the aggregate price vector, respectively, while $\mathbf{g}(t) = [g_1(t), \dots, g_n(t)]^T$ and $\boldsymbol{\rho}(t) = [\rho_1(t), \dots, \rho_n(t)]^T$ are the source vector and the penalty vector, respectively. Notice that $\mathbf{g}(t)$ and $\boldsymbol{\rho}(t)$ are non-negative valued. Flow control algorithms are typically used in TCP protocols to dynamically set $\mathbf{g}(t)$ based on the aggregated prices $\mathbf{q}(t)$ and the aggregate rates $\mathbf{R}(t)$. $\mathbf{q}(t)$ and

$\mathbf{R}(t)$ are dynamically coupled by the following equation system:

$$\begin{aligned}\dot{\mathbf{g}}(t) &= \mathbf{F}(\mathbf{g}(t), \mathbf{q}(t)) \\ \dot{\boldsymbol{\rho}}(t) &= \mathbf{\Gamma}(\boldsymbol{\rho}(t), \mathbf{R}(t))\end{aligned}\tag{5.4}$$

In (5.4) \mathbf{F} is a set of functions $\mathbf{F} = [F_i(g_i(t), q_i(t))]$ associated to the generation rate dynamic and $\mathbf{\Gamma}$ is a set of functions $\mathbf{\Gamma} = [\gamma_i(\rho_i(t), r_i(t))]$ related to the penalty function. Therein, let assume that F_i is continuously differentiable and $\frac{\delta F_i}{\delta q_i} \neq 0$ in $\mathbf{D} = \{(g_i(t), q_i) | g_i(t) > 0, q_i > 0\}$. Let consider points $(g_i(t), q_i) \in \mathbf{D}$ such that $F_i(g_i(t), q_i(t)) = 0$. With the assumptions made on F_i , the implicit function theorem ensures that there exists a unique continuously differentiable function f_i such that:

$$F_i(g_i(t), f_i(g_i(t))) = 0\tag{5.5}$$

5.2.2. Battery model

Wireless node performs the following three main operations: 1) data acquisition and elaboration, 2) radio reception and 3) radio transmission. In our framework, the dynamic evolution of the battery energy $e_i(t)$ is modelled by:

$$\dot{e}_i(t) = h_i(t) - p_i(t)\tag{5.6}$$

where $h_i(t)$ is the power harvested at time t and $p_i(t)$ is the power consumed by node i over time t . The harvesting source $h_i(t)$ in (5.6) is assumed to be slowly time-varying with respect to the system dynamic. It has been observed that the average power consumption $p_i(t)$ is mainly due to the communication activity, [45]. Therefore, the amount of power consumed by node for wireless activity is: $p_i(t) = \phi r_i(t)$, where ϕ is in Watt/Packet and takes into account the consumption both in reception and in transmission. In this model, we are assuming that static consumption of the logic is negligible in respect of power consumed by the RF module.

5.3. Optimal flow control in EH-WSN

5.3.1. Primal Problem formulation

In this section, we formulate the optimization problem (5.7) also including the energy neutrality condition: at each time $p_i(t) = \phi r_i(t) \leq h_i$, so that battery dynamic is theoretically never discharged and autonomy is preserved. Constraints that avoid queue congestion are additionally considered. At each node i we impose that $r_i(t) \leq c_i$ being c_i the link capacity. Many factors dictate on c_i , such as the node data buffer capacity, the signal-to-noise ratio at that node, etc.

Let $N_e = \{i \in N | \min(c_i, h_i/\phi) = h_i/\phi\}$ and let $N_q = \{i \in N | \min(c_i, h_i/\phi) = c_i\}$. In case exist a node j such that $c_j = h_j/\phi$, we assume $j \in N_q$, so that $N_q \cap N_e \equiv \emptyset$, being \emptyset the empty set. By definition, $N_q \cup N_e \equiv N$.

Let define the following notation: a) $\mathbf{P}_e = \{p_i(t)\}$ and $\mathbf{H}_e = \{h_i\}$ for all $i \in N_e$. and b) $\mathbf{R}_q = \{r_i\}$ and $\mathbf{C}_q = \{c_i\}$ for all $i \in N_q$.

With the definitions made, the above energy and queue constraints can be written in compact form: $\mathbf{P}_e \leq \mathbf{H}_e$ and $\mathbf{R}_q \leq \mathbf{C}_q$, respectively.

Remark. *FC node ($i = 1$) usually doesn't present autonomy neither data capacity limitations, differently by network nodes that are typically characterized by reduced energy and capacity availability. However, we assume that constraints on the FC node ($r_1(t) \leq c_1$) is also included into the optimization problem. FC node gathers the overall aggregate rate of the network ($r_1(t) = \sum_{i \in N} g_i(t)$), since all routing paths have FC as destination node. Therefore, by setting value of c_1 , FC can set the maximum throughput of the network according to the application requirement.*

We are interested in allocate the node generation rate \mathbf{g} that solves the following optimization problem:

$$\begin{aligned} \max_{\mathbf{g} \geq \mathbf{0}} \quad & \mathcal{U}(\mathbf{g}) = \sum_{s=1}^n U_s(g_s) & (5.7) \\ \text{s.t.} \quad & \mathbf{P}_e \leq \mathbf{H}_e \\ & \mathbf{R}_q \leq \mathbf{C}_q \end{aligned}$$

being $U_s(g_s)$ the source utility functions, assumed strictly concave. In the following of this paper, the optimal source rates set solution of the primal problem will be denoted with $\mathbf{g}^* = [g_1^*, \dots, g_n^*]^T$, and $\mathcal{U}^* = \mathcal{U}(\mathbf{g}^*)$ will indicate the optimal value of the utility function.

5.3.2. Lagrangian Dual Approach

In this section, we formulate the dual of primal problem (5.7) and we show that it is possible to solve primal problem by cooperatively solving n local sub-problems. The Lagrangian function of the primal problem (5.7) is:

$$\mathcal{L}(\mathbf{g}, \boldsymbol{\mu}, \boldsymbol{\theta}) = \sum_{i \in N} U_i(g_i) + \sum_{j \in N_e} \theta_j (h_j - p_j) + \sum_{j \in N_q} \mu_j (c_j - r_j) \quad (5.8)$$

where $\boldsymbol{\mu} = [\mu_j]$, $\boldsymbol{\theta} = [\theta_j]$ vectors of Lagrangian multipliers. To note that last two terms can be arranged into a single one since index j spans into two disjointed sets: N_e and N_q . We have:

$$\mathcal{L}(\mathbf{g}, \boldsymbol{\rho}) = \sum_{i \in N} U_i(g_i) + \sum_{j \in N} \rho_j (d_j - r_j) \quad (5.9)$$

where $\boldsymbol{\rho} = [\rho_j]$ with ρ_j being:

$$\rho_j = \begin{cases} \phi \theta_j & \text{if } j \in N_e \\ \mu_j & \text{if } j \in N_q \end{cases} \quad (5.10)$$

and:

$$d_j = \begin{cases} h_j/\phi & \text{if } j \in N_e \\ c_j & \text{if } j \in N_q \end{cases} \quad (5.11)$$

Let $\mathcal{Q}(\boldsymbol{\rho}) = \max_{\mathbf{g} \geq \mathbf{0}} \mathcal{L}(\mathbf{g}, \boldsymbol{\rho})$, we have:

$$\mathcal{Q}(\boldsymbol{\rho}) = \max_{\mathbf{g} \geq \mathbf{0}} \left[\sum_{i \in N} U_i(g_i) + \sum_{j \in N} \rho_j (d_j - r_j) \right] = \sum_{i \in N} \max_{g_i \geq 0} \left[U_i(g_i) - g_i \cdot \sum_{j \in N} l(i, j) \rho_j \right] + \sum_{j \in N} \rho_j d_j \quad (5.12)$$

Finally, the dual problem of the primal problem (5.7) is then formulated as a follows: $\min_{\boldsymbol{\rho} \geq \mathbf{0}} \mathcal{Q}(\boldsymbol{\rho})$.

5.3.3. Distributed optimization

Decomposition of the dual utility function $\mathcal{Q}(\boldsymbol{\rho})$ into two distinct contributions, one in \mathbf{g} and the second in $\boldsymbol{\rho}$ (equation (5.12)) is adopted to solve the original optimization problem with a dynamic algorithm. A sketch of the dynamic algorithm procedure at node i is given:

1. For a fixed aggregate price $q_i = \sum_{j \in N} l(j, i) \rho_j$ solve locally the following optimization problem:

$$\max_{g_i \geq 0} \left[U_i(g_i) - g_i \cdot q_i \right] \quad (5.13)$$

2. Update the backlog cost (penalty terms) ρ_i in order to accomplish the existing constraints over the aggregate rate $r_i = \sum_{j \in N} l(i, j) g_j$.

To note that with the hypothesis on concavity of $U_i(g_i)$, the optimal solution of local problem (5.13) is given by:

$$\frac{d}{dg_i} U_i(g_i^*) - q_i = 0 \quad (5.14)$$

being g_i^* the value of g_i that maximizes function in (5.13). Moreover in (5.14) q_i is given and g_i^* depends on q_i . We can therefore define a function $z_i(q_i)$

$$z_i(q_i) : q_i \rightarrow g_i^*, \text{ so that } \frac{d}{dg_i} U_i(g_i^*) = q_i, \quad (5.15)$$

$z_i(q_i)$ is the optimal solution of local problem (5.13). Notice that since $U_i(g_i)$ is strictly concave, $z_i(q_i)$ is a strictly decreasing function of q_i .

Let in the following denote with $\mathbf{z}(\mathbf{q}) = \text{diag}\{z_i(q_i)\}$ a diagonal matrix with $z_i(q_i)$ defined in (5.15) as elements on its main diagonal. Notice that by definition made in (5.3) and (5.15), one can write:

$$\mathbf{R} = \mathbf{L} \cdot \mathbf{z}(\mathbf{q}).$$

5.4. Distributed flow control law formulation

In this section a dynamic system in the form (5.3)-(5.4) is proposed and an equilibrium analysis is carried out.

5.4.1. Penalty function Γ

At each node the following local constraints should be satisfied:

- (a) $p_i(t) = \phi r_i(t) \leq h_i$
- (b) $r_i(t) \leq c_i$

For any node $i \in N_e$, $h_i/\phi < c_i$, then constraint (b) is achieved if (a) is fulfilled. For node $i \in N_e$ the following coupled dynamic $(\eta_i(t), \rho_i(t))$ will be considered:

$$\begin{aligned} \dot{\eta}_i(t) &= \begin{cases} (\phi r_i(t) - h_i) & \eta_i > 0 \\ [\phi r_i(t) - h_i]^+ & \eta_i = 0 \end{cases} \\ \dot{\rho}_i(t) &= \begin{cases} \beta_1(\alpha_1 \eta_i(t) + \phi r_i(t) - h_i) & \rho_i > 0 \\ [\beta_1(\alpha_1 \eta_i(t) + \phi r_i(t) - h_i)]^+ & \rho_i = 0 \end{cases} \end{aligned} \quad (5.16)$$

where $[a]^+ = a$ if $a > 0$, otherwise $[a]^+ = 0$. In (5.16) η_i is an increasing function of node utilization, while ρ_i is the penalty function and $\alpha_1, \beta_1 > 0$ are positive constants. Notice that $\rho_i(t)$ is a positive variable, and therefore we have that $\rho_i(t) = [\rho_i(t)]^+$.

Equilibrium analysis: let $(\bar{\eta}_i, \bar{\rho}_i)$ be an equilibrium point for (5.16). We note that $\bar{\eta}_i$ cannot be positive. Indeed, if $\bar{\eta}_i > 0$ we have $\bar{r}_i = \frac{h_i}{\phi}$, but from the $\rho_i(t)$ dynamic $\dot{\bar{\rho}}_i = 0$ means $\bar{\eta}_i = 0$, which is in contrast with the hypothesis on $\bar{\eta}_i$. On the other hand, if $\bar{\eta}_i = 0$, we have $\bar{r}_i \leq \frac{h_i}{\phi}$ and from dynamic on $\rho_i(t)$ it results: 1) $\bar{\rho}_i = 0$ if $\bar{r}_i < \frac{h_i}{\phi}$ or 2) $\bar{\rho}_i > 0$ if $\bar{r}_i = \frac{h_i}{\phi}$. Then, the slackness property on ρ_i is verified. We can conclude that the unique equilibrium point here is $\bar{\eta}_i = 0$ and $\bar{\rho}_i \geq 0$, with $\bar{\rho}_i > 0$ for saturated links.

On the other hand, for any node $i \in N_q$ the coupled dynamic $(\omega_i(t), \rho_i(t))$ will be adopted:

$$\begin{aligned} \dot{\omega}_i(t) &= \begin{cases} (r_i(t) - c_i) & \omega_i > 0 \\ [r_i(t) - c_i]^+ & \omega_i = 0 \end{cases} \\ \dot{\rho}_i(t) &= \begin{cases} \beta_2(\alpha_2 \omega_i(t) + r_i(t) - c_i) & \rho_i > 0 \\ [\beta_2(\alpha_2 \omega_i(t) + r_i(t) - c_i)]^+ & \rho_i = 0 \end{cases} \end{aligned} \quad (5.17)$$

with $\alpha_2, \beta_2 > 0$ being positive constants.

Equilibrium analysis: let $(\bar{\omega}_i, \bar{\rho}_i)$ be an equilibrium point for (5.17). Similarly to the previous analysis, problem (5.17) has a unique equilibrium point $\bar{\omega}_i = 0$ and $\bar{\rho}_i \geq 0$ with $\bar{\rho}_i > 0$ for saturated links.

5.4.2. Generation rate control F

Generation rate at each node is dynamically set according to the following law:

$$\dot{g}_i(t) = F_i(g_i(t), q_i(t)) = \frac{1}{a} \left(1 - q_i(t) - \phi \right) - b \left(q_i(t) + \phi \right) g_i^2 \quad (5.18)$$

being a, b control law gains. Notice that $g_i(t)$ is a positive variable, and therefore we have that $g_i(t) = [g_i(t)]^+$ for each t . Equilibrium points (\bar{g}_i, \bar{q}_i) of F_i are given by:

$$\begin{aligned} \frac{1}{a} (1 - \bar{q}_i - \phi) - b (\bar{q}_i + \phi) \bar{g}_i^2 &= 0 \\ \rightarrow \dots \rightarrow \bar{q}_i &= \frac{1}{1 + a \cdot b \cdot \bar{g}_i^2} - \phi \end{aligned} \quad (5.19)$$

From definition of f_i (equation (5.5)) particularized to the selected function F_i (5.18) it follows:

$$f_i(g_i) = \frac{1}{1 + a \cdot b \cdot g_i^2} - \phi \quad (5.20)$$

In order to have $f_i(g_i)$ non-negative, it has to result:

$$0 \leq g_i \leq \sqrt{\frac{1}{a \cdot b} \left(\frac{1}{\phi} - 1 \right)} \quad (5.21)$$

and $0 \leq \phi \leq 1$.

5.5. Convergence and stability analysis

In this section, the dynamic properties of the proposed distributed control law are analysed. We provide a convergence theorem that shows that the proposed dynamic law converges to a point that coincides to the optimal solution of the primal problem. Additionally, a stability theorem is provided. In particular, we provide a suitable Lyapunov function and we can demonstrate the global asymptotic stability of the proposed control law by making use of the LaSalle invariance principle.

5.5.1. Convergence analysis

Theorem 1. *The steady-state rate of the proposed dynamic system (5.16)-(5.17)-(5.18) equals the optimal rate of the primal problem (5.7) with utility function $U_i(g_i)$ given by:*

$$U_i(g_i) = \int f_i(g_i) dg_i = \frac{1}{\sqrt{a \cdot b}} \cdot \arctan(\sqrt{a \cdot b} \cdot g_i) - \phi \cdot g_i \quad (5.22)$$

with $f_i(g_i)$ given in (5.20).

Proof. It is known that the optimal solution of the dual problem coincides with the \mathbf{g}^* without duality gap if and only if (Proposition 5.1.5 in [112]) the *Karush-Kuhn-Tucker* (KKT) conditions are met. In [107] authors show that for the problem in the form (5.1) KKT conditions are met for a dynamic system in the form (5.4) provided that certain conditions are met. For the sake of clearness, such result (Theorem A) has been reported in the Appendix C. To demonstrate that the proposed dynamic system (5.16)-(5.17)-(5.18) converges to the optimal solution of given problem (5.7), we only have to show that hypotheses of Theorem A hold.

Hypothesis (C1) of Theorem A holds since equilibrium points of (5.16)-(5.17)-(5.18) exist as previously demonstrated and ρ_i, g_i are positive state variables. Hypotheses (C2) and (C4) of Theorem A hold as well. Indeed, function F_i in (5.18) is continuously differentiable and $\frac{\delta F_i}{\delta q_i} \neq 0$ for all $(g_i, q_i) \in \mathbf{D}$. Moreover, f_i in (5.20) is a strictly decreasing function since

$$\frac{df_i}{dg_i} = -\frac{2a \cdot b \cdot g_i}{(1 + a \cdot b \cdot g_i^2)^2} < 0$$

for each $g_i > 0$. Consequently, U_i defined in (5.22) is strictly concave. Finally, since hypothesis (C3) of Theorem A holds as above stated, we conclude that all the hypotheses of Theorem A are verified and result follows. \square

5.5.2. Stability analysis

In this section, an analysis of stability for the proposed control is studied. Inspired by the stability analysis provided in [111], the proof is composed of two parts: 1) firstly, we show that the proposed dynamic system is stable in the Lyapunov sense; 2) secondly, under the assumption that \mathbf{L} is a full row rank matrix, the global asymptotic stability is demonstrated through the LaSalle invariance principle.

Let preliminary define the following non negative integral function $\Phi_i(q_i)$ for all node i :

$$\Phi_i(q_i) = \int_{\bar{q}_i}^{q_i} (\bar{g}_i - z_i(\sigma)) d\sigma \quad (5.23)$$

where \bar{g}_i is the steady-state rate at node i , while $z_i(q_i)$ is defined in (5.15) and is a decreasing function of q_i . $\Phi_i(q_i)$ is then non negative for all q_i and $\Phi_i(q_i) = 0$ if and only if $q_i = \bar{q}_i$.

Let study the derivative over time of function $\sum_i \Phi_i(q_i)$:

$$\frac{d}{dq_i} \left(\sum_{i=1}^n \Phi_i(q_i) \right) = \sum_{i=1}^n \left(\bar{g}_i - z_i(q_i) \right) \dot{q}_i = \sum_{i=1}^n \left(\bar{g}_i - z_i(q_i) \right) \dot{q}_i = \left(\bar{\mathbf{g}} - \mathbf{g} \right)^T \cdot \dot{\mathbf{q}}$$

being T the transpose of its argument and where the definition $g_i = z_i(q_i)$ is used. From (5.3) it follows:

$$\begin{aligned} \frac{d}{dq_i} \left(\sum_{i=1}^n \Phi_i(q_i) \right) &= \left(\bar{\mathbf{g}} - \mathbf{g} \right)^T \cdot \dot{\mathbf{q}} = \left(\bar{\mathbf{g}} - \mathbf{g} \right)^T \cdot \mathbf{L}^T \dot{\boldsymbol{\rho}} = \\ &= \left(\bar{\mathbf{R}} - \mathbf{R} \right)^T \cdot \dot{\boldsymbol{\rho}} = \sum_{j \in N_e} (\bar{r}_j - r_j) \dot{\rho}_j + \sum_{j \in N_q} (\bar{r}_j - r_j) \dot{\rho}_j \end{aligned} \quad (5.24)$$

Now we are ready to prove the following result:

Theorem 2. *The (unique) equilibrium point of system with dynamic (5.16)-(5.17)-(5.18) is stable in the Lyapunov sense. Moreover, if the routing matrix \mathbf{L} is a full row rank matrix, then the dynamic system is globally asymptotically stable.*

Proof. Proof is based on the Lyapunov stability theorem and is similar to demonstration provided in [111]. In particular we are interested to find a suitable Lyapunov function for the dynamic system (5.16)-(5.17)-(5.18). A candidate function we propose is:

$$\begin{aligned} \mathcal{V}(\boldsymbol{\eta}, \boldsymbol{\omega}, \boldsymbol{\rho}) &= \sum_{j \in N_e} \left(\beta_1 \alpha_1 \frac{\eta_j^2}{2} + (h_j - \phi \bar{r}_j) \rho_j \right) \\ &+ \phi \sum_{j \in N_q} \left(\beta_2 \alpha_2 \frac{\omega_j^2}{2} + (c_j - \bar{r}_j) \rho_j \right) \\ &+ \phi \sum_{i=1}^n \Phi_i(q_i) \end{aligned} \quad (5.25)$$

\mathcal{V} is function of variables η_j , ω_j , ρ_j and is a non negative function, since it is the sum of non negative terms. Moreover, $\mathcal{V}(\boldsymbol{\eta}, \boldsymbol{\omega}, \boldsymbol{\rho}) = 0$ at equilibrium $(\boldsymbol{\eta}, \boldsymbol{\omega}, \boldsymbol{\rho}) = (\bar{\boldsymbol{\eta}}, \bar{\boldsymbol{\omega}}, \bar{\boldsymbol{\rho}})$ since as above demonstrated: a) $\bar{\eta}_j = 0$, $\bar{\rho}_j \geq 0$, with $\bar{\rho}_j > 0$ for energy-saturated nodes (i.e. $h_j - \phi \bar{r}_j = 0$); b) $\bar{\omega}_j = 0$, $\bar{\rho}_j \geq 0$, with $\bar{\rho}_j > 0$ for rate-saturated nodes (i.e. $c_j - \bar{r}_j = 0$); c) $\Phi_i(\bar{q}_i) = 0$. Additionally, \mathcal{V} is radially unbounded, since for each $(\boldsymbol{\eta}, \boldsymbol{\omega}, \boldsymbol{\rho})$ such that $\|(\boldsymbol{\eta}, \boldsymbol{\omega}, \boldsymbol{\rho})\| \rightarrow +\infty$, $\mathcal{V} \rightarrow +\infty$. Finally, \mathcal{V} is a non increasing function of time. To show that, let derive \mathcal{V} in respect to the time. We have:

$$\begin{aligned} \dot{\mathcal{V}} &= \sum_{j \in N_e} \left(\beta_1 \alpha_1 \eta_j \dot{\eta}_j + (h_j - \phi \bar{r}_j) \dot{\rho}_j \right) + \phi \sum_{j \in N_q} \left(\beta_2 \alpha_2 \omega_j \dot{\omega}_j + (c_j - \bar{r}_j) \dot{\rho}_j \right) \\ &+ \phi \left(\sum_{j \in N_e} (\bar{r}_j - r_j) \cdot \dot{\rho}_j + \sum_{j \in N_q} (\bar{r}_j - r_j) \cdot \dot{\rho}_j \right) \end{aligned}$$

where for the derivative of $\sum_{i=1}^n \Phi_i(q_i)$ we have used the result in (5.24). It follows:

$$\begin{aligned} \dot{\mathcal{V}} &= \sum_{j \in N_e} \left(\beta_1 \alpha_1 \eta_j \dot{\eta}_j + (h_j - \phi r_j) \dot{\rho}_j \right) + \sum_{j \in N_q} \phi \left(\beta_2 \alpha_2 \omega_j \dot{\omega}_j + (c_j - r_j) \dot{\rho}_j \right) \\ &= \sum_{j \in N_e} v_{e(j)} + \sum_{j \in N_q} v_{q(j)} \end{aligned} \quad (5.26)$$

Now we show that $v_{e(j)}$ for all $j \in N_e$ and $v_{q(j)}$ for all $j \in N_q$ as well are non positive functions. Let analyse $v_{e(j)}$ by dividing its domain of definition (η_j, ρ_j) into four separated semi-planes. We have:

1. $(\eta_j = 0 \wedge \rho_j > 0)$ According to model (5.16) it results:

$$v_{e(j)} = (h_j - \phi r_j) \beta_1 (\phi r_j - h_j) < 0$$

2. $(\eta_j = 0 \wedge \rho_j = 0)$

$$v_{e(j)} = (h_j - \phi r_j) \beta_1 \max\{0, (\phi r_j - h_j)\}$$

In this case if $\phi r_j < h_j$ then $v_{e(j)} = 0$. On the other hand, if $\phi r_j > h_j$ it results $v_{e(j)} = -\beta_1 (h_j - \phi r_j)^2 < 0$.

3. $(\eta_j > 0 \wedge \rho_j > 0)$ According to the dynamic model (5.16) we obtain:

$$v_{e(j)} = \beta_1 \alpha_1 \eta_j \dot{\eta}_j + (h_j - \phi r_j) \beta_1 (\alpha_1 \eta_j + \phi r_j - h_j) = \dots = -\beta_1 (h_j - \phi r_j)^2 < 0$$

4. $(\eta_j > 0 \wedge \rho_j = 0)$

$$v_{e(j)} = \beta_1 \alpha_1 \eta_j \dot{\eta}_j + (h_j - \phi r_j) \beta_1 \max\{0, (\alpha_1 \eta_j + \phi r_j - h_j)\}$$

Now, if $\alpha_1 \eta_j + \phi r_j - h_j \leq 0$ (i.e. $\eta_j \leq \frac{h_j - \phi r_j}{\alpha_1}$) it results:

$$v_{e(j)} = \beta_1 \alpha_1 \eta_j (\phi r_j - h_j) \leq -\beta_1 (h_j - \phi r_j)^2 < 0$$

On the other hand, if $\alpha_1 \eta_j + \phi r_j - h_j < 0$ we have:

$$v_{e(j)} = \beta_1 \alpha_1 \eta_j (\phi r_j - h_j) + (h_j - \phi r_j) \beta_1 (\alpha_1 \eta_j + \phi r_j - h_j) = -\beta_1 (h_j - \phi r_j)^2 \leq 0$$

A similar analysis can be carried out for $v_{q(j)}$ and it will be omitted for brevity.

In conclusion, $v_{e(j)}$ and $v_{q(j)}$ are non positive definite $\forall j$ and this proves that the provided system is stable in Lyapunov sense.

To prove the global asymptotic stability of the system, we will invoke the LaSalle invariance principle ([111, 113]), reported in Appendix C. To this aim, let define with $\mathcal{E} = \{(\eta_j, \omega_j, \rho_j) : \dot{\mathcal{V}} = 0\}$ the set where the derivative of Lyapunov function is zero. Moreover, let define $\mathcal{E}_e = \{(\eta_j, \rho_j), j \in N_e : v_{e(j)} = 0\}$ and $\mathcal{E}_q = \{(\omega_j, \rho_j), j \in N_q : v_{q(j)} = 0\}$. Since $\dot{\mathcal{V}}$ can be decomposed as in (5.26), we have that $\mathcal{E} = \mathcal{E}_e \cup \mathcal{E}_q$. To show the global asymptotic stability of the system, we have to show that the largest invariant set \mathcal{S} contained in the set \mathcal{E} coincides with the equilibrium point of system (5.16)-(5.17), or equivalently that no solution of system can stay identically in \mathcal{E} other than the equilibrium point of system (5.16)-(5.17).

Let $\omega = [\omega_j(t)]$, $\eta = [\eta_j(t)]$, $\rho = [\rho_j(t)]$ for all $j \in N$ so that $(\omega, \eta, \rho) \in \mathcal{E}$. Additionally be $\eta^0 = \eta(0)$, and $\rho^0 = \rho(0)$. At the same time, define $\eta_e(t) = [\eta_j(t)]$ and $\rho_e = [\rho_j(t)]$ with $j \in N_e$ vectors of initial system states so that $(\eta_e, \rho_e) \in \mathcal{E}_e$. Let additionally be $\eta_e^0 = \eta_e(0)$, and $\rho_e^0 = \rho_e(0)$. Finally, let denote with $\omega_q(t) = [\omega_j(t)]$, $\rho_q(t) = [\rho_j(t)]$ with $j \in N_q$ vectors of initial system states so that $(\eta_q, \rho_q) \in \mathcal{E}_q$. Additionally $\eta_q^0 = \eta_q(0)$, and $\rho_q^0 = \rho_q(0)$.

Let preliminary consider a trajectory that is fully inside the set \mathcal{E}_e .

In this case, the evolution of dynamics related to the condition $v_{e(j)} = 0$ with $j \in N_e$ can be:

$$\begin{aligned} (a) \quad r_j &= \frac{h_j}{\phi} \quad \text{or} \\ (b) \quad r_j &< \frac{h_j}{\phi} \wedge \rho_j = \eta_j = 0 \end{aligned} \tag{5.27}$$

for all $j \in N_e$. It can be shown that the system state space belonging to \mathcal{E}_e eventually evolves by following a trajectory given by: $\eta_e = \eta_e^0$ and $\rho_e = \rho_e^0 + \rho'_e \cdot t$, where $\rho'_e = \beta_1 \alpha_1 \cdot [\eta_j(0)]$ for all $j \in N_e$. Indeed for each j we have:

1. if $\eta_j(0) = 0$ then $\eta_j(t) = 0$ and $\rho_j(t) = \rho_j(0)$. Indeed if initially $\eta_j(0) = 0$, it remains indefinitely in this state, from (5.27) and being $r_j(t) \leq h_j/\phi$. Moreover, from system equation (5.16) it results $\dot{\rho}_j(t) = 0$ for all time t , and $\rho_j(t) = \rho_j(0)$ is constant.
2. if $\eta_j(0) > 0$ then $\eta_j(t) = \eta_j(0)$ and $\rho_j = \rho_j(0) + \beta_1 \alpha_1 \eta_j(0) \cdot t$. Indeed, with $\eta_j(0) > 0$, we are initially in case (a) of (5.27) and thus $\eta_j(t)$ remains constant due to (5.16), while $\rho_j(t)$ grows linearly with rate $\rho'_j = \beta_1 \alpha_1 \eta_j(0)$ and it stays in this case indefinitely.

Consider now \mathcal{E}_q . Condition $v_{q(j)} = 0$ occurs when:

$$\begin{aligned} (a) \quad r_j &= c_j \\ (b) \quad r_j &< c_j \wedge \rho_j = \omega_j = 0 \end{aligned} \tag{5.28}$$

for all $j \in N_q$. By similar considerations given above for the set \mathcal{E}_q , it can be concluded that: $\omega_q = \omega_q^0$ and $\rho_q = \rho_q^0 + \rho'_q \cdot t$, where $\rho'_q = \beta_2 \alpha_2 \cdot \omega_q^0$ for all $j \in N_q$.

Finally, consider from (5.26) that $\dot{\mathcal{V}} = 0$ implies $v_{e(j)} = 0$ for all $j \in N_e$ and $v_{q(j)} = 0$ for all $j \in N_q$. Therefore, the state space $(\omega, \eta, \rho) \in \mathcal{E}$ evolves from the initial state $(\omega^0, \eta^0, \rho^0)$ with a trajectory remaining inside \mathcal{E} that is given by:

$$\begin{cases} \omega &= \omega^0 \\ \eta &= \eta^0 \\ \rho &= \rho^0 + \rho' \cdot t \end{cases} \tag{5.29}$$

where in this case $\rho' = [\rho'_j]$ is a column vector of n angular coefficients given by:

$$\rho'_j = \begin{cases} \beta_1 \alpha_1 \cdot \eta_j(0) & \text{if } j \in N_e \\ \beta_2 \alpha_2 \cdot \omega_j(0) & \text{if } j \in N_q \end{cases} \tag{5.30}$$

With the definition made, we have:

$$\begin{aligned} \mathbf{q}(t) &= \mathbf{L}^T (\rho^0 + \rho' \cdot t) \\ \mathbf{g}(t) &= \mathbf{z} \left(\mathbf{L}^T (\rho^0 + \rho' \cdot t) \right) \\ \mathbf{R}(t) &= \mathbf{L} \cdot \mathbf{z} \left(\mathbf{L}^T (\rho^0 + \rho' \cdot t) \right) \end{aligned} \tag{5.31}$$

where $\mathbf{z} = \text{diag}\{z_i(q_i(t))\}$ as in (5.15). Now consider the product:

$$\left(\rho' \right)^T \cdot \dot{\mathbf{R}}(t) = \sum_{j \in N} \rho'_j \dot{r}_j(t) = 0 \tag{5.32}$$

for all time t . Indeed if $\rho'_j > 0$, $r_j(t)$ is constant since for all $j \in N_e$ condition (5.27).(a) holds and for all $j \in N_q$ condition (5.28).(a) holds as well.

Substituting the above positions (5.31) in (5.32) we have:

$$\left(\rho' \right)^T \cdot \dot{\mathbf{R}}(\rho) = \left(\rho' \right)^T \cdot \mathbf{L} \cdot \dot{\mathbf{z}} \left(\mathbf{L}^T (\rho^0 + \rho' \cdot t) \right) \cdot \mathbf{L}^T \rho' = 0 \tag{5.33}$$

Noting that $\dot{\mathbf{z}} = \text{diag}\{\dot{z}_i(q_i(t))\}$ is strictly negative for all of its components and the above equation holds if and only if $\mathbf{L}^T \rho' = 0$, or, invoking the hypothesis of full rank on \mathbf{L} , $\rho' = 0$. This implies

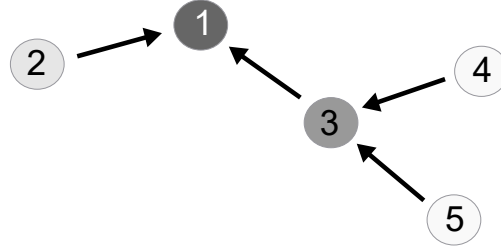


Figure 5.1.: Network topology considered for the simulation validation scenario of Sec. 5.6.

	d_1	d_2	d_3	d_4	d_5
$t \in (0, 200)$	50	30	30	30	30
$t \in [200, 500)$	50	30	20	30	30
$t \in [500, 900]$	50	30	10	30	30

Table 5.1.: Simulation parameters for d_j in (5.11): values in black are if $d_j = c_j$, while values in red correspond to the case $d_j = \frac{h_j}{\phi}$.

that for all $j \in N_e$ $\eta_j(t) = 0$, $j \in N_q$ $\omega_j(t) = 0$ and for all $j \in N$ $\rho_j(t) = \rho_j(0)$. In other terms, we have shown that the largest invariant set \mathcal{I} contained in \mathcal{E} is composed of just one point, $(\boldsymbol{\eta}, \boldsymbol{\omega}, \boldsymbol{\rho}) = (\bar{\boldsymbol{\eta}}, \bar{\boldsymbol{\omega}}, \bar{\boldsymbol{\rho}})$ that also coincides with the equilibrium point of system (5.17) - (5.16).

Recalling that \mathcal{V} is radially unbounded, from the LaSalle invariance principle it derives that system (5.17) - (5.16) is globally asymptotically stable. \square

5.6. Simulation Validation

In this section, the proposed control law (5.16)-(5.17)-(5.18) is tested. Simulation are carried out considering the network topology in Fig. 5.1 and dynamic parameters in Table 5.1 and assuming $\phi = 3.75mW/\text{packet}$ and $n = 5$.

In order to evaluate the effectiveness of the proposed distributed flow control law to satisfy harvesting and queue constraints, we consider the scenario where the harvesting availability at node 3 in Fig. 5.1 slightly reduces over time. As reported in Table 5.1, simulation can be analysed into three periods of time.

During the first part of simulation ($t \in (0, 200)$) $d_3 = c_3 = 30$, since the energy harvesting h_3 is sufficiently high so that Node 3 belongs to N_q . In this period of time, node rates are upper limited by the FC application requirement (i.e. $c_1 = 50$) and we have $g_5 = g_4 = g_3 = 10$ and $g_2 = 20$ (Fig. 5.2), that yield to have $r_4 = r_5 = 10$, $r_3 = 30$, $r_2 = 20$ and $r_1 = 50$.

In the next simulation period ($t \in [200, 500)$), $d_3 = h_3/\phi = 20$. In this case node 3 may limit the generation of Nodes 4 and 5 in order to fulfil rate constraint on Node 3. Moreover, we expect that

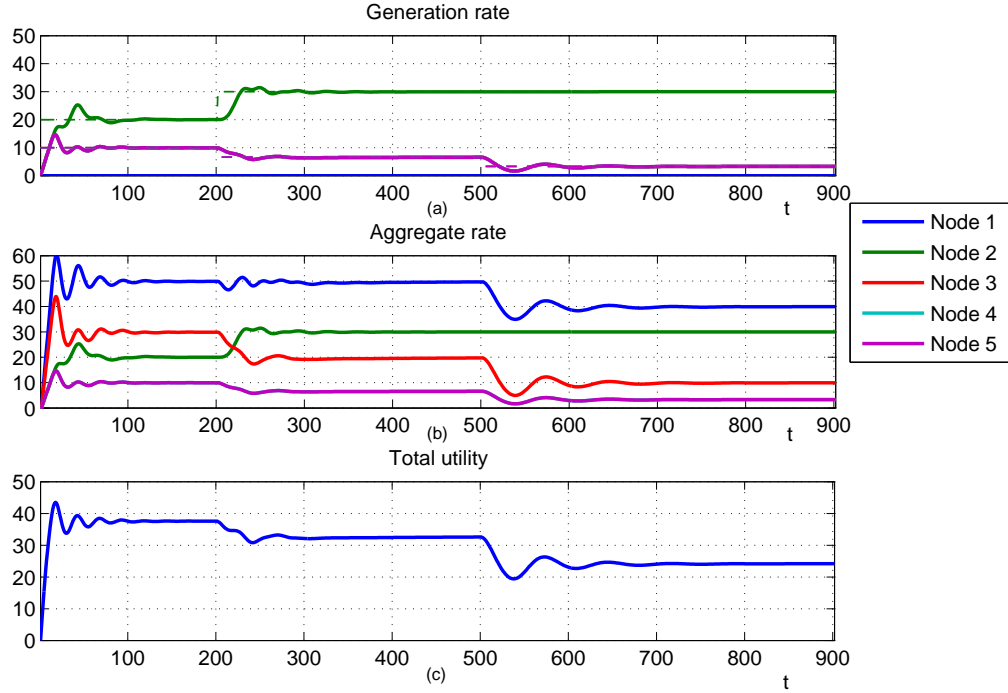


Figure 5.2.: Dynamic evolution of the proposed simulation scenario.

node 2 increases its rate in order to maximize the aggregate rate to node 1. Results in Fig. 5.2 confirm the expected behaviour. In particular, at steady-state we have $g_3 = g_4 = g_5 = 6.66$ (so that $r_3 = 19.98 \sim 20$), while $g_2 = 30$, so that $r_2 = 30 = d_2$ and $r_1 = 39.98 \sim 40$.

Finally, in the third period of simulation time ($t \in [500, 900)$), harvesting availability further reduces and we have $d_3 = h_3/\phi = 10$. In this case, however, the decreasing of the upper limit of r_3 to d_3 cannot be compensated by a further increment of r_2 to fulfil load requirements since in the previous period of time r_2 was still at its maximum rate. Consequently, we expect that the overall delivered rate to the FC (r_1) is no longer at the required value, $d_1 = 50$. Simulation in Fig. 5.2 confirms the above consideration, yielding to $g_5 = g_4 = g_3 = 3.33$, $r_2 = 30 = d_2$, that hence is $r_5 = r_4 = 3.33$, $r_3 = 9.99$, $r_2 = 30$ and $r_1 = 39.99$.

5.7. Experimental validation

In this section, we experimentally validate the proposed distributed rate control over a prototyping WSN. Specifically, the WSN has been built up with Wireless Sensor Node named "Medimote" produced by Medinok Spa, shown in Fig. 5.3. In this section, we preliminary describe the flow

control protocol implemented into the prototyped WSN. The experimental setup is therefore described. Finally, experimental results are analysed.

5.7.1. Flow control protocol implementation

Flow control law in (5.16)-(5.17) is distributively implemented over a small wireless network. It is composed of two competitive mechanisms that involve the generation rate g_i and the aggregation price q_i . In particular, equation (5.18) increases the generation rates g_i . As feedback from father nodes, i receives backlogs ρ_i that are summed up in the aggregate price q_i . A $q_i > 0$ notifies to i to reduce its generation rate g_i , as follows from equation (5.18). Consequently, positive backlogs ρ_i will reduce through one of (5.16)-(5.17) and causes q_i to reduce as well. Equilibrium between g_i and q_i is reached when the optimal rate is allocated.

Therefore, to achieve the flow control, the integrated wireless network is developed with a structure composed of an application layer and a transport layer. At the former layer, a generic stream of data is generated with rate g_i and is sent through preassigned paths to FC node. Since each node is both a generator and a router of information, it also receives packet data from its child nodes and redirects them towards the FC. Meantly speaking, each node will send data (generated and rerouted packets) at the average rate r_i . Underneath, the transport layer implements the traffic of backlogs to child nodes, evaluates its own backlog according to equations (5.17) and (5.16), computes the aggregate price q_i and regulates dynamically g_i through (5.18).

5.7.2. Setup overview

A small network composed of 5 wireless nodes has been built for this experimental validation. Each node is assembled with: 1) a transceiver module belonging of the Series 1 XBee DigiMesh; 2) a low power micro-controller belonging to the Microchip family; 3) few micro-sensors, such as temperature, humidity and light sensors.

The network in Fig. 5.1 implements a Monitoring WSN and thus a stream of data is communicated to the FC node along with the traffic of backlogs. In addition, a measurement wireless system, composed of a gateway node and the network nodes themselves, gathers the required information from the experimental setup and visualizes it on a PC. Details of the measurement system are provided hereafter in this section.

Wireless network description The adopted Wireless transmitters for this experiment belong to the Series 1 of XBee DigiMesh RF modules. Transmitters operate at 2.4 GHz carriage according to the 802.15.4 standard and have a nominal 250kbps transmission rate, despite it is widely acknowledged an effective 80kbps rate. These radios can perform both point-to-point and point-

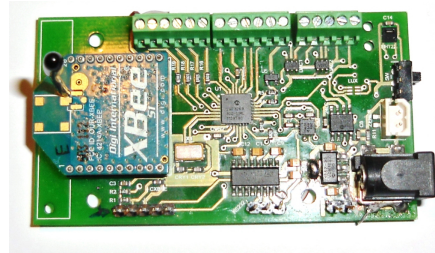


Figure 5.3.: A Wireless Sensor Node, named "Medimote" (photo by courtesy of Medinok Spa.) used in the experimental validation section.

to-multipoint networking. Mesh topology (such as the topology in Fig. 5.1) is a type of network where each node must not only capture and disseminate its own data, but also may serve as a relay for other nodes, that is, it must collaborate to propagate the data in the network. From the user side, XBee module communicates through a serial UART data interface. It supports two modes of operation, namely AT mode and API mode. In AT (transparent) mode, the XBee radio simply relays serial data to the receiving XBee, as identified by a 64-bits address. In API mode, the communication with the radio is achieved by sending and receiving formatted packets and represents the most practical way to use the functionalities of DigiMesh protocol as a whole, including data redundancy and communication robustness. Another important feature of XBee transceiver is the embedded sleep protocol. Despite XBee modules consume 50 mA in transmission state, they can fall in a sleep state when they do not transmit data. In this case, module current requirement is less than $50\mu\text{A}$. Additionally, it is fully implemented into the XBee stack the cyclic sleep mode function where XBee modules cyclically wake up and sleep synchronously. A so called sleep coordinator sends out a sleep synchronization packet to everyone in the network during each wake cycle which overwrites whatever sleep settings the XBee might have previously had. These features make XBee technology attractive for being used in low power applications.

Wireless measurement system The measurement system should not introduce perturbation of system equilibrium, while the experiment is running on. Indeed, if measurement traffic overlaps with 'ordinary' traffic, the rate control equilibria is spoiled. A viable solution is to build a supporting network composed of one gateway node connected through a star topology with the Wireless Network under test. Gateway node is visible to each network node in order to reduce the overhead due to data communication with the measurement system (Fig. 5.4.(a)). This is possible via the versatile XBee transceiver protocol that is able to communicate in a point-to-point mode with visible nodes. Gateway node is then connected by a serial port with a PC that show the received information. Although raw serial data can be easily read by many software on the Internet (HyperTerminal, Termit, RealTerm, and so on), they show data packets as they reach the

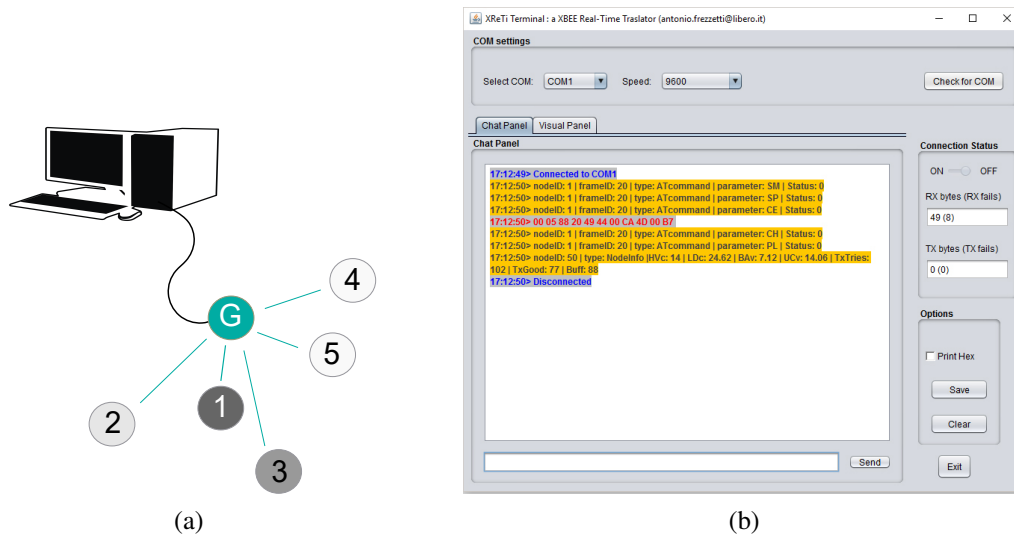


Figure 5.4.: Setup description: (a) Measurement setup; (b) User-friendly serial interface terminal: XReTi Translator.

PC (typically in Hexadecimal or ASCII code), making difficult to read information that the packet contains. Moreover, the most of serial interfaces cannot save data in a viable form to be easily read out by graphical programs, e.g. the Matlab. Motivated by these limitations, I have implemented an user-friendly RS232 interface Terminal, named XReTi (XBee Real-Time) Translator (a snapshot is given in Fig. 5.4.(b)). XReTi is written in Java language and uses the Java AWT for the user interface. After having connected it to the serial COM with the desired baud rate, it periodically polls the serial buffer to read incoming data. When buffer is flushed, data bytes are grouped into packets (recognizable through the initial $0x7E$ delimiter). For each identified packet, the program recognizes the source, the type of packet and the payload content throughout a customizable field. After the packet translation, the interpreted packet is printed on a frontal Panel, for a real time assessment of the monitored system. Additionally, the acquired data can be saved in a suitable text file, to be easily read and plotted for example in the Matlab environment.

Firmware description On each wireless node, an on-board micro-controller is programmed to implement both the application and the transport layers described above, and therefore to orchestrate the distributed traffic regulation. A sketch of the implemented embedded firmware is explained in this section. In Fig. 5.5 a flowchart synthetically represents the program flow. An event-driven finite state machine (FSM) is implemented. In particular, the state machine, namely 'nextTask' in the flowchart, can assume 6 different states (**IDLE**, **PRIOR**, **USERCOMM**, **COMM**, **SENDMEAS** and **ELAB**) on the basis of mainly two Interrupt Service Routines, namely

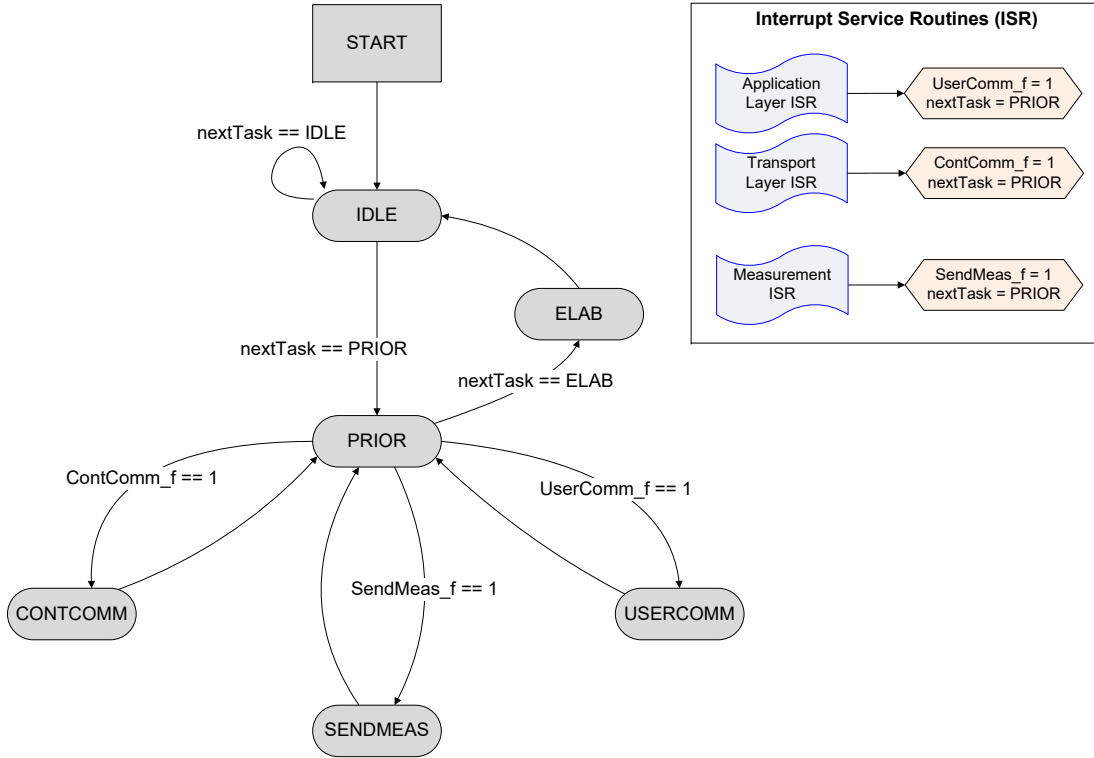


Figure 5.5.: Flowchart description of the micro-controller firmware implemented for the experimental validation section.

the *Application Layer ISR* and the *Transport Layer ISR*. In particular, the *Application Layer ISR* executes when packets are received or when it is time to communicate data to the FC. Transport Layer ISR is carried out at each backlog reception or if is the time to communicate the own backlog to child nodes. Additionally, another ISR is added to the program flow, that is the *Measurement ISR*, that is a timer-driven interrupt, periodically advising the state machine that it should communicate the node’s states to the gateway node for the measurement system. When one ISR occurs, a specific flag ($UserComm_f$, $ContComm_f$, $SendMeas_f$) is set depending on the ISR occurred.

Three main states are important for the implementation of the monitoring and the transport layers: **USERCOMM**, **CONTCOMM** and **ELAB**. In **USERCOMM** generated and received packets are transmitted with rate r_i . In **CONTCOMM** received and own backlogs are communicated to child nodes. In **ELAB** state, the micro-controller elaborates its backlog ρ_i on the basis of the estimated received data rate, and also elaborates g_i basing on the aggregate price q_i .

On the other hand, **PRIOR** state is useful to drive the state machine on the basis of the occurred events. Finally, **SENDMEAS** builds and sends the measurement packet to the gateway for the application testing. Ordinary, $nextTask$ is in **IDLE** state, doing nothing than waiting for at least

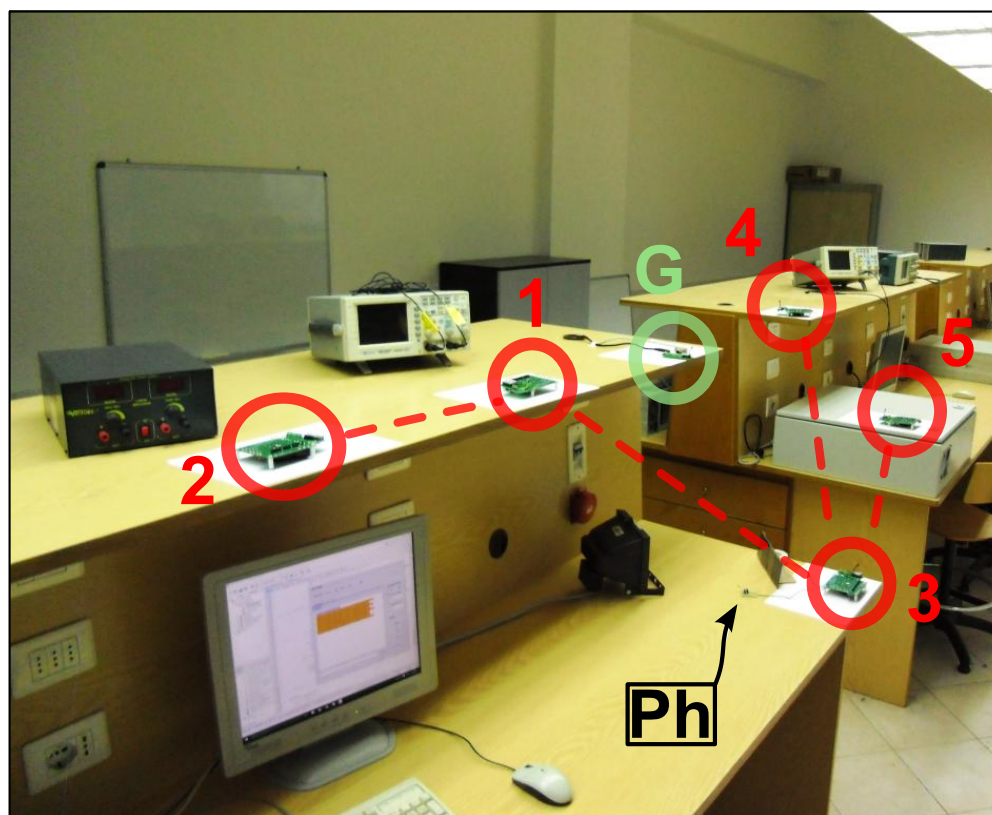


Figure 5.6.: Picture of the experiment carried out at the Embedded System Laboratory, University Federico II of Naples. Particulars are highlighted: sensor nodes (from 1 to 5), gateway (G), photo-resistor (Ph).

one interrupt to occur. When at least one ISR happens, nextTask is event-driven to the **PRIOR** state (nextTask=PRIOR). **PRIOR** state implements a prioritizer which on the basis of current flag settings (UserComm_f, ContComm_f, SendMeas_f) drives the state machine to execute one state among **USERCOMM**, **CONTCOMM** or **SENDMEAS**. **USERCOMM** has the highest priority, it follows **CONTCOMM** and finally **SENDMEAS**. If any flag is unset or each set flag has been still served, the machine state switches to **ELAB** and finally comes back to be **IDLE**.

5.7.3. Experimental results

The effectiveness of the above flow control law is proved in this section. A WSN configured as in Fig. 5.1 is designed. A controlled indoor test has been carried out at the Embedded System Laboratory, University Federico II of Naples (Fig. 5.6). Wireless nodes are battery-supplied, while Node 3 is additionally supplied by four Sanyo AM-5907 solar harvesting cells (250mW @ 5V) that are exposed under a controllable source of light. Wireless nodes are fully operative when

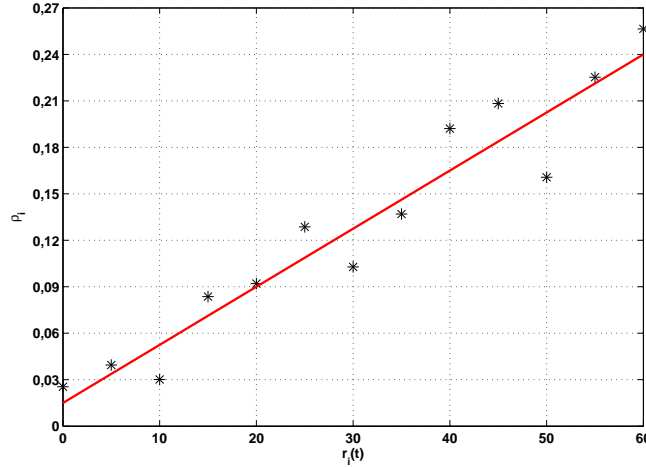


Figure 5.7.: Characterization of node consumption p_i (in Watt) as function of $r_i(t)$ (in $packet/\Delta T$): experimental data (black), linear fitting curve (red).

they transmit data, while their consumption decreases when they are in reception mode or in idle mode. The embedded XBee low power communication protocol is used for this experiment. To tune parameters of our controller, i.e. d_i in (5.11), the average power consumption p_i of a sensor node operating inside the WSN of our setup has been characterized with a step-by-step changing in $packets/\Delta T$, Fig. 5.7. Experimental data are therefore linearly fitted to obtain $p_i(t) = \phi r_i(t) + \varepsilon$, being $\phi = 3.75mW/packet$ and $\varepsilon = 15mW$. ε is the average static consumption of the logic. So far, we assumed that $\varepsilon = 0$. The assumption continues to hold if $\phi r_i(t) \gg \varepsilon$. When this condition is not verified, the only way to achieve the energy neutrality condition is that the harvesting source has to cover at least the static consumption of the logic. In this experiment, the energy resource h_3 is measured through a photo-resistor, as shown in Fig. 5.6 (Ph). During the indoor experimentation, the energy resource is changed three times: from the beginning to 70 minutes test light is at highest level and $h_3 \sim 60mW$; from 70 to 130 minutes light is slightly lowered to achieve $h_3 = 30mW$ and from 130 to the end of the experiment, light produces $h_3 = 20mW$. We assume that under highest level of light $c_3 = 50$ and $h_3/\phi \sim 60$ so that Node 3 rate is limited by capacity rate and we have $d_3 = 50$. Under lower light expositions the energy harvesting limits the aggregate rate and d_3 decreases to $d_3 = 30$ when $h_3 = 30mW$ and to $d_3 = 10$ when $h_3 = 20mW$. The experimental setup configuration is summarized in Table 5.2. The given values of d_j and c_j in this experimentation equal the values of simulation (Table 5.1). Therefore, regime values of generation rates in the experimental validation are similar to those chosen in the simulation validation section. The measurement system, described above, provides data from each node with an average rate of 1 sample for each 25 seconds. A discrete version of the control law with a discrete step of $\Delta T = 8$

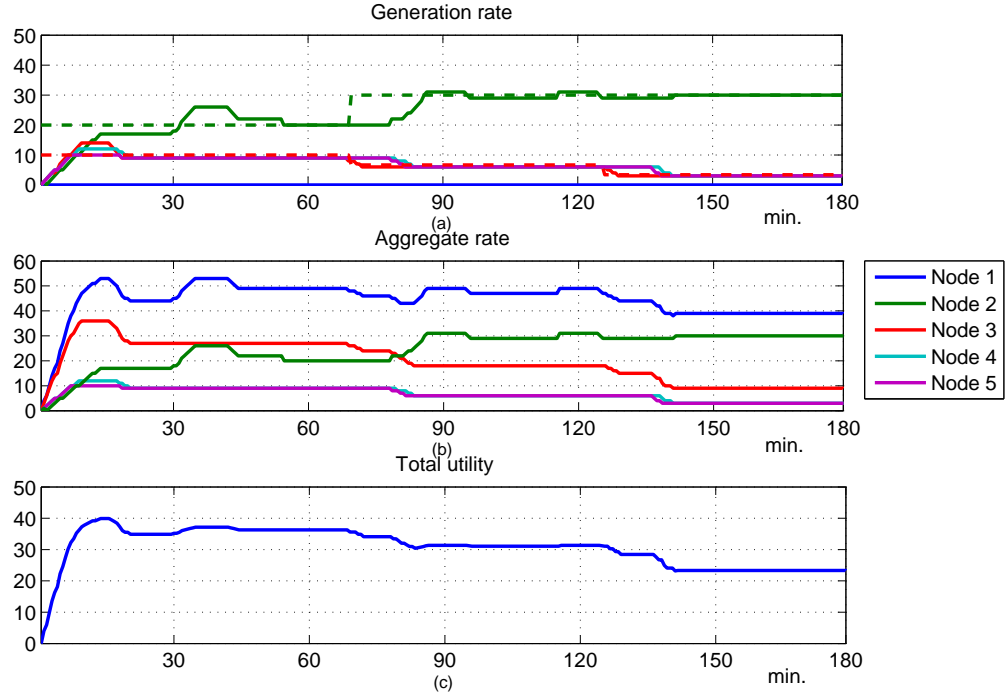


Figure 5.8.: Experimental results: (a) generation rates $\mathbf{g}(t)$ (continuous lines) and the respective optimal solutions of the primal problem (dashed lines), (b) aggregate rate $\mathbf{R}(t)$ and (c) the total network utility $\mathcal{U}(\mathbf{g})$.

sec. is implemented into the micro-controller. In Fig. 5.8 the network dynamics collected by the measurement system are shown. We can distinguish: in Fig. 5.8.(a) the dynamic evolution of generation rates $\mathbf{g}(t)$ (continuous lines) and respective optimal values (dashed lines) in packets/ ΔT , the aggregate rate $\mathbf{R}(t)$ in packets/ ΔT (Fig. 5.8.(b)) and the total utility $\mathcal{U}(\mathbf{g})$ (Fig. 5.8.(c)). As can be seen, the aggregate rate on Node 1 is maximized both under highest and middle light intensity levels. When, however, h_3 is at its lowest value, Node 3 rate reduces and Nodes 4 and 5 do the same, while Node 2 is still at its maximum rate. Therefore, the aggregate rate at Node 1 can no longer be to 50, but it reduces down to 40.

5.8. Conclusion

In this chapter an optimal control law to cope with both queue congestion and energy neutrality condition in EH-WSN has been proposed. Starting by a primal optimal problem formulation and by making use of the well established theory of primal-dual Lagrange decomposition, we devised a distributed control algorithm that assess the optimal solution of the primal problem. In

	d_1	d_2	d_3	d_4	d_5
$t \in (0, 70)min.$	50	30	30	30	30
$t \in [70, 130)min.$	50	30	20	30	30
$t \in [130, 180]min.$	50	30	10	30	30

Table 5.2.: Experimental parameters for d_j in (5.11): values in black are if $d_j = c_j$, while values in red correspond to the case $d_j = \frac{h_j}{\phi}$.

this formulation, the equilibrium point is function of the energy harvesting level and changes the allocated rate of each node accordingly. In particular, when the energy harvesting is low, the allocated incoming rate should be regulated in order that the energy neutrality condition is achieved. Convergence and global asymptotic stability of the proposed control law are demonstrated. A simulation validation of the proposed control law confirms the behaviour of the proposed controller to set dynamically the rate allocation also under variable harvesting conditions. Therefore, an experimental validation is carried out to verify the effectiveness of the procedure with a real EH-WSN scenario.

Double Layer control for EH-WSN

6.1. Motivation

THE main issues required by a WSN monitoring system are to guarantee: i) that sampled information from the field is opportunely collected and sent to the FC where the signal is efficiently reconstructed; ii) network operability by preventing node failures when the battery runs out of energy. Compressive Sensing (CS) is a sampling paradigm which exploits the compressibility of signals in order to reduce the number of data required for data compression and reconstruction, [48, 62]. The main aim is to achieve low values of the Mean Square Error (MSE) between the recovered signal and the original one (*reconstruction error* in the following). Recently, it has been introduced Random Sampling CS (rsCS) ([114]) that is more suitable than the standard CS algorithm for the WSN scenario ([115, 116, 117]) as the number of measurements required for the signal reconstruction is lower than the number of sensors nodes. Therefore, rsCS improves network lifetime but degrades the reconstruction error than the CS method. In this respect, it is of interest to devise a control strategy in order to guarantee good performances in terms of both the reconstruction error and network lifetime.

6.1.1. Related Works and chapter Contribution

In the literature, reconstruction error and network lifetime performances are typically controlled apart. A scheme widely adopted to control the reconstruction error is depicted in Fig. 6.1 ([116, 119, 120]). It consists of a centralized controller that sets a control variable (p_{FC} in Fig. 6.1) in order to obtain a desired level of signal reconstruction error (\overline{MSE} in Fig. 6.1). Specifically, in this scheme the reconstruction error MSE is evaluated by the FC on the base of the received compressed data from the network $\mathbf{R}_g = [\mathbf{R}_g^{(i)}]$. The compressed information generated at each

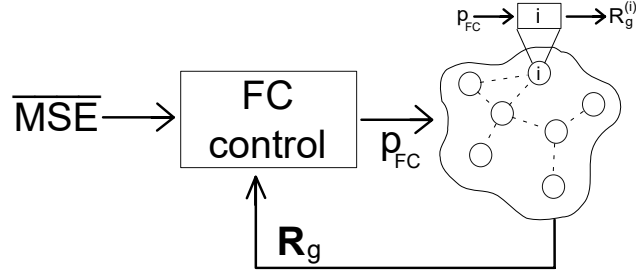


Figure 6.1.: General scheme of rsCS consisting of a centralized FC controller and a network of sampling nodes. On the base of incoming rate R_g the FC sets the control parameter p_{FC} in order to achieve the desired \overline{MSE} .

node $R_g^{(i)}$ depends on the node sampling probability $p^{(i)}$ that in turns is function of the FC control variable p_{FC} . On the basis of \overline{MSE} and a measured MSE , the FC control evaluates p_{FC} in order to steer the MSE close to the desired one \overline{MSE} . Authors in [120] present a controller able to ensure the desired reconstruction error, while the network lifetime is not taken into account.

In [121] authors propose an energy saving rsCS scheme to improve network lifetime by reducing the sampling rate of nodes with low energy. Although this scheme reduces power consumption, many disadvantages arise. Firstly, it is assumed that the power consumption in the WSNs is dominated by the sensing operations, while typically the most part of power consumption is due to wireless communication ([23, 45]). Secondly, there is not an explicit controller that regulates the reconstruction error to a desired value. This degrades the signal reconstruction performance as the network approaches to the end of its life. This chapter proposes a two-layer controller that is able to simultaneously assess the desired reconstruction error and improve network lifetime. It is developed on two layers: a global controller at the FC layer and local controllers at sensor node layer. The global controller (*FC control* block in Fig. 6.1) is implemented at FC level aimed to regulate the reconstruction error to a desired value, given as set point. On the other hand, local controllers (atomic i block in Fig. 6.1), tries to limit the power consumption at the node by controlling both the sampling probability and incoming traffic route.

6.1.2. Chapter Organization and Notation

The rest of the chapter is organized as follows. In Sec. II, the background of CS and rsCS is briefly introduced. The EH-WSN model used in the chapter is presented in Sec. III. In Sec. IV performance metrics are defined. In Sec. V the proposed two-layer controller scheme is described. In Sec. VI a simulation validation and a performance evaluation comparison with two main rsCS schemes in the literature are carried out. Conclusions are given in Sec. VII. The following notation will be use in the chapter. We indicate with $X^{(i)}$ the i -th component of vector \mathbf{X} , namely $\mathbf{X} = [X^{(i)}]$.

To distinguish between vectors and matrices, capital Greek letters in bold, e.g. Θ , will denote matrices. The following operators on vectors are defined. L_1 and L_2 norms on vector \mathbf{X} will be indicated with $\|\mathbf{X}\|_{L_1}$ and $\|\mathbf{X}\|_{L_2}$, respectively. $|\cdot|$ indicates the absolute value of its argument (\cdot) . $\mathbb{E}(\mathbf{X})$ refers to the arithmetic mean on \mathbf{X} 's elements, i.e. $\mathbb{E}(\mathbf{X}) = 1/n \sum_{i=1}^n X^{(i)}$, being n the vector size. Let s represents a stochastic variable, we indicate with $\langle s \rangle$ and with $var(s)$ the average and the variance of s , respectively.

6.2. Random Sampling Compressive Sensing in EH-WSN

So far, in Chapter 3.5 we have analysed three different type of CS proposed in literature and applied on WSN: standard CS (sCS), random sampling CS (rsCS) and adaptive CS (aCS). In that chapter we have compared the three compression methods together with classic technique of compression and we find out that the rsCS performs better than the others in terms of Network Lifetime and Reconstruction Error. Therefore, in this work we formulate a controller system to dynamically regulate the performance of a WSN operating with the rsCS compression scheme. We recall that Random sampling CS (rsCS) ([116, 121]) adopts the CS scheme (P), while the compression algorithm (3.9) operates with a binary matrix Ψ_{CS} with only one non-zero per each row. This implies that the network nodes have to sample at each period of time ΔT a number of measurements n_Y from different nodes, thus potentially reducing the power consumption than the standard CS.

Let denote with ΔT the discrete time step and with $k \cdot \Delta T$ (in the following k for brevity) the generic discrete time, with $k \in \mathbb{N}$ and \mathbb{N} being the set of natural numbers. During the generic time period $[(k-1)\Delta T, k\Delta T]$, node i generates an average number of sampled data that will be denoted with $g_i(k)$ and referred to as *generation rate*. In this chapter we assume, for the sake of simplicity, that each packet contains only one sensed data. Let define $p^{(i)}(k)$ the average sampling probability of node i in the period $[(k-1)\Delta T, k\Delta T]$, it results:

$$g_i(k) = \bar{R} \cdot p^{(i)}(k) \tag{6.1}$$

being \bar{R} the maximum generation rate. From (6.1) it results that $g_i(k) = 0$ if $p^{(i)}(k) = 0$ and $g_i(k) = \bar{R}$ if $p^{(i)}(k) = 1$. Moreover, a wireless node is also characterized by a flow of packets coming from the rest of network. Let $r_i(k)$ denotes the average value of the *incoming rate* in the period $[(k-1)\Delta T, k\Delta T]$, the average number of transmitted packets (*outgoing rate*) $t_i(k)$ is given by:

$$t_i(k) = g_i(k) + r_i(k) \tag{6.2}$$

Notice that:

$$r_i(k) = \sum_{j \in \mathcal{U}_\Omega^{(i)}} g_j(k) \quad (6.3)$$

such that $r_i(k)$ depends on upstream tree $\mathcal{U}_\Omega^{(i)}$. Node consumption can be related to the rsCS as shown in Chapter 5.6. In this context, we consider the dynamic evolution of the battery energy in its discrete form

$$e_i(k+1) = e_i(k) + h_i(k) - \Delta e_i(k) \quad (6.4)$$

as in equ. (3.6), with the only difference that in this case we have added the term $h_i(k)$ that is the harvested energy and $\Delta e_i(k)$ is the energy spent by node i in the time period $[(k-1)\Delta T, k\Delta T]$. Notice that differently by (3.6), in (6.4) we omit apex on $e_i(k)$ since it is implicitly refers to the rsCS compression scheme. Let for sake of compactness, define $\mathbf{E}_b(k) = [e_i(k)]^T$ for all i . The harvesting source $h_i(k)$ in (6.4) is a single realization of a stochastic process $\mathbf{E}_h^{(i)}$ at node i modelled as a i.i.d. Gaussian distribution with average $\langle \mathbf{E}_h^{(i)} \rangle$ and variance $\text{var}(\mathbf{E}_h^{(i)})$. The node power consumption $\Delta e_i(k)$ can be expressed as [45]:

$$\begin{aligned} \Delta e_i(k) &= g_i(k)(\phi_{ACQ}^0 + \phi_{TX}^0) + r_i(k)(\phi_{RX}^0 + \phi_{TX}^0) \\ &= g_i(k)(\phi_{ACQ}^0 + \phi_{TX}^0) + \sum_{j \in \mathcal{U}_\Omega^{(i)}} g_j(k)(\phi_{RX}^0 + \phi_{TX}^0) \end{aligned} \quad (6.5)$$

Notice that the proposed battery dynamic model takes into account both the network traffic (by means of $\mathcal{U}_\Omega^{(i)}$) and the sampling probability $p^{(i)}$ (by means of $g_i(k)$, as it results from (2)).

6.3. Network Performances

In what follows, we consider as network performances the network lifetime, namely T_l , defined in Sec. 3.3.1 and the reconstruction error, namely MSE, defined in Sec. 3.3.2. For easiness of reading, we recall their definitions.

Network Lifetime T_l is defined as the lifetime of the node in the network that firstly depletes its energy, i.e.: $T_l = \min_{i \in [1, \dots, n]} [\tau^{(i)}]$.

MSE measures the error between the recovered signal $\mathbf{X}^{(ny)}$ and the original one \mathbf{X} and it is defined as:

$$\text{MSE} = \frac{\|\mathbf{X} - \mathbf{X}^{(ny)}\|_{L_2}}{\|\mathbf{X}\|_{L_2}} \quad (6.6)$$

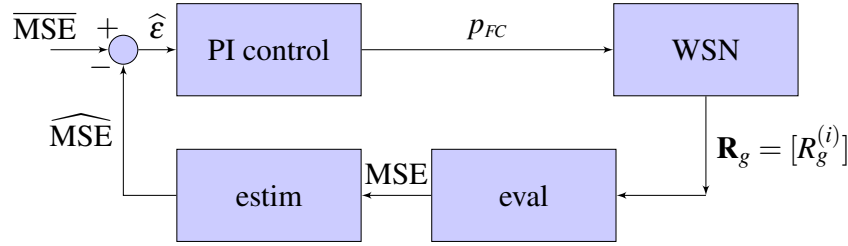


Figure 6.2.: Global controller at the FC layer.

6.4. The two-layer controller scheme

In order to regulate the trade-off of the two network performances defined above, in this chapter we propose a two-layer controller composed of: a global controller implemented at the FC and a local controller performed by each sensor node. In the following, the proposed schemes ([118]) will be detailed.

6.4.1. Global controller

The proposed FC controller evaluates the control variable p_{FC} according to the standard Proportional-Integral control law ([122]):

$$p_{FC}(k \cdot M') = K_p \cdot \varepsilon(k \cdot M') + K_i \Delta T \sum_{j=1}^{k \cdot M'} \varepsilon(j) \quad (6.7)$$

where K_p and K_i are the proportional and integral gain and $\varepsilon(j)$ is the difference between the set point $\overline{\text{MSE}}$ and the measured one.

Notice that the evaluation of the MSE cannot be performed continuously on time as it requires the sampling of \mathbf{X} and $\mathbf{X}^{(ny)}$ to evaluate (7), with an additional amount of power consumption. It is then necessary to compute the MSE less frequently than each time step k . In the following of the chapter, we assume that MSE is evaluated at time $k \cdot M$, with $1 \ll M \ll M'$. In order to have a value of MSE also when it has not been computed, we will consider its estimation $\widehat{\text{MSE}}$ given by:

$$\widehat{\text{MSE}}(j) = \alpha \widehat{\text{MSE}}(j-1) + (1 - \alpha) \text{MSE}(k \cdot M) \quad (6.8)$$

for $j \in [k \cdot M, (k+1) \cdot M)$. In (6.8), α is the oblivion parameter and $\text{MSE}(k \cdot M)$ is the measured value of the MSE at time $k \cdot M$. This moving average estimator is denoted by *estim* block in Fig. 6.2.

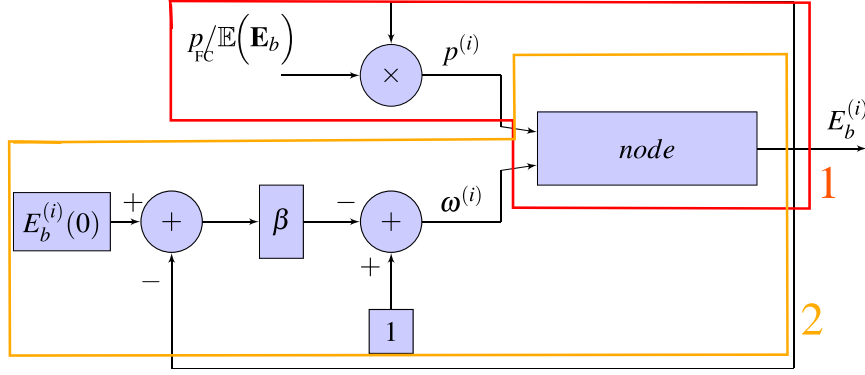


Figure 6.3.: Local controllers implemented at each node i -th: box 1) controller of node sampling probability $p^{(i)}$; box 2) routing energy-aware controller of node weight $\omega^{(i)}$.

Therefore, in the control law (6.7) an estimation $\widehat{\varepsilon}(j) = \overline{\text{MSE}} - \widehat{\text{MSE}}(j)$ will be used in place of $\varepsilon(j) = \overline{\text{MSE}} - \text{MSE}(j)$. The final global controller at the FC results:

$$p_{FC}(k \cdot M') = K_p \cdot \widehat{\varepsilon}(k \cdot M') + K_i \Delta T \sum_{j=1}^{k \cdot M'} \widehat{\varepsilon}(j) \quad (6.9)$$

and it is depicted in Fig. 6.2. The periodic evaluation of the reconstruction error $\text{MSE}(k \cdot M)$ in (6.8) is carried out by a specific procedure that we name *MSE evaluation phase*.

During this phase, the FC receives from the network both \mathbf{X} and \mathbf{Y}_{CS} vectors. Once $\mathbf{X}^{(ny)}$ is computed from vector \mathbf{Y}_{CS} by means of the procedure described in Sec. II, FC uses \mathbf{X} and $\mathbf{X}^{(ny)}$ to compute MSE according to (6.6). This operation is represented in Fig. 6.2 by the *MSE eval* block. At time $k \cdot M'$, the FC evaluates $p_{FC}(k \cdot M')$ in (6.9) and uses the estimation $\widehat{\text{MSE}}$ also to compute the integral term $\sum_{j=1}^{k \cdot M'} \widehat{\varepsilon}(j)$. Then the FC communicates p_{FC} to network nodes that update their generation rates $g_i(k \cdot M')$ according to the local control law (detailed in the next subsection).

6.4.2. Local controllers

In the following, we will introduce two local controllers that respectively leverage on the $g_i(k)$ and $r_i(k)$ to bound the power consumption (according equation (6.5)) while it is guaranteed the

requirement on the reconstruction error $\overline{\text{MSE}}$. The two controllers have been depicted in Fig. 6.3 and are highlighted by box 1 and box 2.

The first local controller (box 1 in Fig. 6.3) acts on the node sampling probability $p^{(i)}(j)$ to regulate $g_i(j)$ according to (6.1) and to reduce the power consumption. Specifically, we propose for node i to update its own sampling probability $p^{(i)}(j)$ for $j \in [k \cdot M', (k+1) \cdot M')$ according to the following energy-aware law:

$$p^{(i)}(j) = p_{FC}(k \cdot M') \times \frac{e_i(j)}{\mathbb{E}(\mathbf{E}_b(k \cdot M'))} \quad (6.10)$$

where: $p_{FC}(k \cdot M')$ is the global feed-forward term generated by the global controller at time $k \cdot M'$, $\mathbf{E}_b(k \cdot M')$ is the vector of battery energies and $\mathbb{E}(\mathbf{E}_b(k \cdot M')) = 1/n \sum_{z=1}^n e_z(k \cdot M')$ is the average battery energy over the network at time $k \cdot M'$. Equation (6.10) ensures that the local sampling probabilities $p^{(i)}(j)$ are distributed around the control variable p_{FC} according to their residual energy $e_i(j)$. Notice that, at time $j = k \cdot M'$ it results:

$$\mathbb{E}(\mathbf{p}(k \cdot M')) = \frac{1}{n} \sum_{i=1}^n p_{FC}(k \cdot M') \frac{e_i(k \cdot M')}{\mathbb{E}(\mathbf{E}_b(k \cdot M'))} = p_{FC}(k \cdot M')$$

such that in the average network nodes generate packets to guarantee the desired $\overline{\text{MSE}}$. Additionally, nodes with higher available energy $e_i(j)$ have their sampling probability $p^{(i)}(j)$ greater than node with lower energy.

In order to further improve the energy efficiency, we consider an additional control law (box 2 in Fig. 6.3) so that weights in the Dijkstra's paths are fixed on the basis of node residual energy. In this way, by equation (4) we control r_i to bound the power consumption, according equation (6). The local control law sets node Dijkstra's weight at time $k \cdot M''$, with $M'' > M'$, according to the following energy-aware routing law:

$$\omega^{(i)}(k \cdot M'') = 1 + \bar{\beta} \left(1 - \frac{e_i(k \cdot M'')}{e_i(0)} \right) = 1 + \beta (e_i(0) - e_i(k \cdot M'')) \quad (6.11)$$

where $\beta = \frac{\bar{\beta}}{e_i(0)}$ and $\bar{\beta} > 0$. The proposed law assigns an higher value to $\omega^{(i)}$ of such nodes that have lower residual energies. In particular, $\omega^{(i)}(k \cdot M'') \in [1, 1 + \beta]$, with $\omega^{(i)}(k \cdot M'') = 1$ if node's battery is full ($e_i(k \cdot M'') = e_i(0)$) and $\omega^{(i)}(k \cdot M'') = 1 + \beta$ when node battery is empty (i.e. $e_i(k \cdot M'') = 0$). The unit term in (6.11) only avoids $\omega^{(i)}(k \cdot M'')$ to be zero if $e_i(0) = e_i(k \cdot M'')$. The main aim of the control law (6.11) is to reduce the cardinality of the upstream tree set $\mathcal{U}_\Omega^{(\cdot)}$ of those nodes that have a lower residual energy, thus reducing their incoming rate.

Remark Notice that the local controllers at the network nodes act significantly faster than the global controller located at the FC. Indeed, the global control variable $p_{FC}(k \cdot M')$ (equation 6.9) and the local control variables $p^{(i)}(k)$ (equation (6.10)) and $\omega^{(i)}(k \cdot M'')$ (equation (6.11)) are updated respectively at time $k \cdot M'$, k , $k \cdot M''$, with $1 \ll M' < M''$.

6.4.3. The two-layer controller implementation

According to the proposed local control law (6.10), each node has to locally compute the same factor gain $1/\mathbb{E}(\mathbf{E}_b(k \cdot M'))$. Although $\mathbb{E}(\mathbf{E}_b(k \cdot M'))$ can be distributively estimated in runtime through some cooperative algorithms (e.g. the average consensus [123, 124, 125]), this implies an additional consumption of energy. Therefore, we adopt the scheme such that the FC evaluates $\mathbb{E}(\mathbf{E}_b(k \cdot M'))$ to finally compute:

$$\bar{p}_{FC}(k \cdot M') = \frac{p_{FC}(k \cdot M')}{\mathbb{E}(\mathbf{E}_b(k \cdot M'))}, \quad (6.12)$$

with p_{FC} given by (10). Then the FC sends the computed \bar{p}_{FC} to all network nodes. Consequently, the local control law at node (6.10) can be implemented by:

$$p^{(i)}(j) = \bar{p}_{FC}(k \cdot M') \cdot e_i(j). \quad (6.13)$$

$\mathbf{E}_b(k \cdot M')$ may be obtained by the FC from the network during the last MSE evaluation phase. Indeed, while the FC receives \mathbf{X} from the WSN, $\mathbf{E}_b(k \cdot M')$ can be piled up into packets containing \mathbf{X} . In this way, no additional energy consumption is required.

6.5. Simulation validation

In this section we will validate the network performances achieved by the proposed two-layer controller. Simulations have been carried out under the MATLAB environment, such that the power consumption of the WSN is simulated by means of the provided model. The rsCS compression schemes are applied over a representative thermal profile characterized by compressible signal in Discrete Cosine Transform (DCT) domain with $n_S = 30$. We use the L1-magic tool [126] running under MATLAB in order to achieve the reconstruction algorithm (P). Results will be compared with the following other two rsCS techniques existing in literature:

1) **Standard rsCS** (shortly S-rsCS, [121, 127]). In this case, it is assumed that

$$p^{(i)} = p \quad (6.14)$$

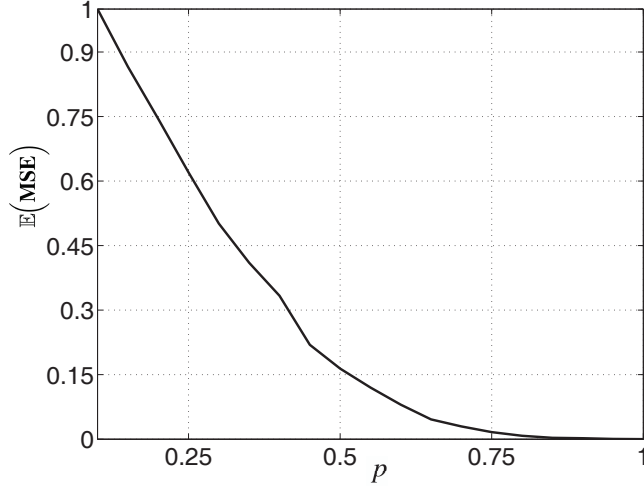


Figure 6.4.: $\mathbb{E}(\mathbf{MSE})$ performance achieved with the S-rsCS strategy under rsCS with $p^{(i)} = p \forall i$, $p \in (0, 1]$.

where $p \in [0, 1]$. This scheme is also referred to Uniform rsCS. The performance of the S-rsCS scheme is reported in Fig. 6.4, where for each fixed $p \in (0, 1]$ we report the mean performance $\mathbb{E}(\mathbf{MSE})$ over the set \mathbf{MSE} of 5000 MSE measurements (i.e. $\mathbf{MSE} = [\mathbf{MSE}^{(i)}] i = 1..5000$). Notice that as p increases the $\mathbb{E}(\mathbf{MSE})$ reduces. By this analysis we find out that $\mathbb{E}(\mathbf{MSE}) \sim 0.15$ is achieved at $p = 0.5$, while $\mathbb{E}(\mathbf{MSE}) \sim 0.1$ is with $p = 0.57$. Therefore, the results in Fig. 6.4 may be used to design the value of p to get the desired $\overline{\mathbf{MSE}}$.

2) **Energy Aware rsCS** (shortly EA-rsCS [121]). In this case, the sampling probability $p^{(i)}$ is no longer kept uniform among nodes, but it is assigned the following sampling probability:

$$p^{(i)}(j) = \frac{n_Y}{nT} \frac{e_i(j)}{\mathbb{E}(\mathbf{E}_b(j))} \quad (6.15)$$

By the control law (6.15) a lower generation rate is assigned to those of nodes with lower residual energy and, on the other hand, an higher generation rate to such nodes with higher residual energy. In Table 6.1 we summarize the values of model parameters that will be adopted in the following simulations.

6.5.1. Nominal scenario

Firstly, we compare the S-rsCS and EA-rsCS with the proposed Two-Layer rsCS (later called TL-rsCS) assuming $e_i(0) = 100J \forall i$, $\overline{\mathbf{MSE}} = 0.15$ and absence of harvesting sources (i.e. $h_i(k) =$

WSN model parameters	Control parameters
$n = 100$ nodes	$K_p = 0.1$
$E_{TH} = 0.1J$	$K_i = 0.5$
$\phi_{ACQ}^0 = 7.97\mu J$	$\alpha = 100$
$\phi_{RX}^0 = 10\mu J$	$\bar{\beta} = 100$
$\phi_{TX}^0 = 0.1mJ$	$M = 100$
$\langle E_h^{(i)} \rangle = 1\mu J \forall i$	$M' = 1000$
$var(E_h^{(i)}) = 1\mu J \forall i$	$M'' = 5000$

Table 6.1.: EH-WSN model and control parameters considered in the simulation validation.

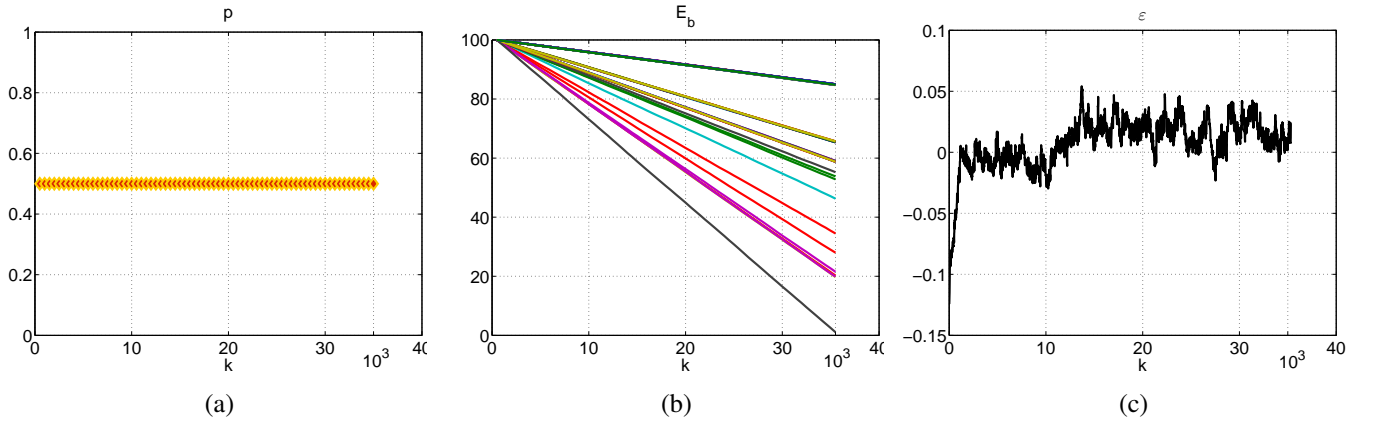


Figure 6.5.: S-rsCS strategy: (a) Uniform sampling probability $p^{(i)} = p = 0.5 \forall i$; (b) Dynamic evolution of energy levels $e_i(k)$; (c) Dynamic evolution of $\epsilon = \overline{\text{MSE}} - \text{MSE}$ with $\overline{\text{MSE}} = 0.15$.

$0 \forall i, k$). Simulation results are depicted in Figs. 6.6-6.7 where it is shown the dynamic evolution of $p^{(i)}$, $E_b(k)$ and the error $\epsilon(j)$.

According with the S-rsCS scheme (Fig. 6.5), nodes transmits with a sampling probability $p^{(i)} = p \forall i$ (Fig. 6.5(a)) with $p = 0.5$ which provides $\mathbb{E}(\text{MSE}) \sim 0.15$, according to the performance analysis of Fig. 6.4. In Fig. 6.5(c) the time evolution of $\epsilon(j)$ is depicted. As in this case node traffic is meanly constant over time, $e_i(k)$ evolves with a constant discharge rate (Fig. 6.5(b)). We evaluate the network lifetime T_l that is presented in Table 6.2. Additionally, in order to evaluate the effectiveness of each strategy to regulate the MSE to the set point value $\overline{\text{MSE}}$, we compute the steady state value (after the initial transient period) of the absolute mean error $\mathbb{E}(|\epsilon(j)|)$, with $|\epsilon(j)| = |\overline{\text{MSE}} - \text{MSE}(j)|$. This index is denoted with $\bar{\epsilon}$ in Table 6.2. In this scenario, for the S-rsCS it results $T_l = 35 \cdot 10^3$ and $\bar{\epsilon} = 0.0159$.

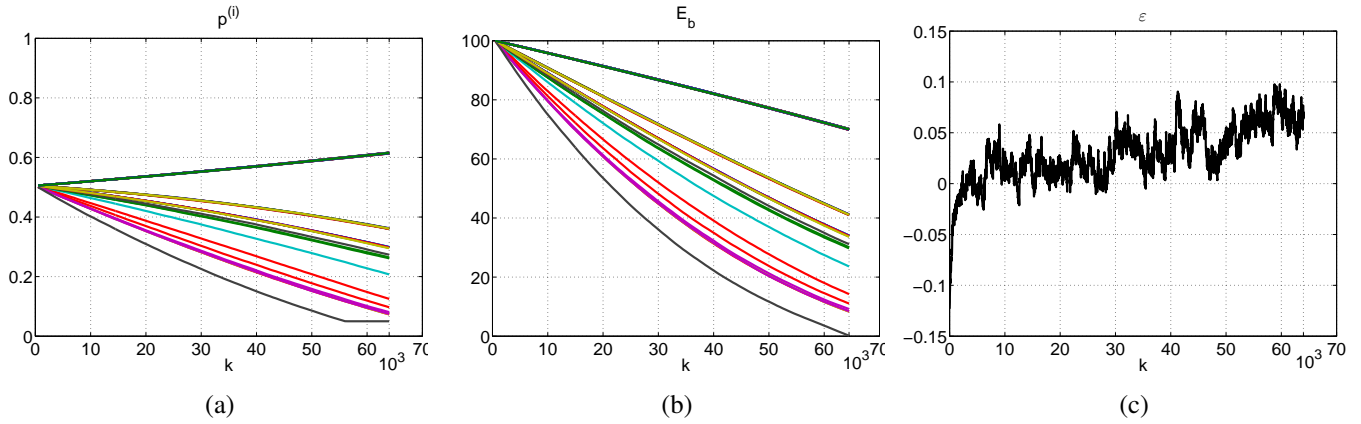


Figure 6.6.: EA-rsCS strategy: (a) Sampling probability $p^{(i)}$ (continuous line); (b) Dynamic evolution of energy levels $e_i(k)$; (c) Dynamic evolution of $\varepsilon = \overline{\text{MSE}} - \text{MSE}$ with $\overline{\text{MSE}} = 0.15$.

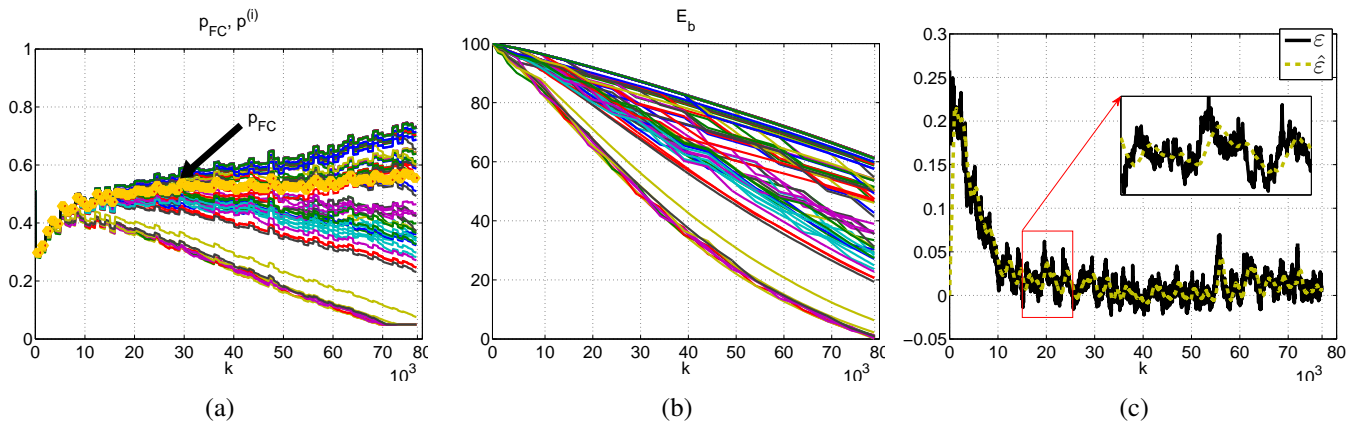


Figure 6.7.: TL-rsCS strategy: (a) Sampling probability $p^{(i)}$ (continuous line), sampling reference p_{FC} (thick line); (b) Dynamic evolution of energy levels $e_i(k)$; (c) Dynamic evolution of $\varepsilon = \overline{\text{MSE}} - \text{MSE}$ (continuous line) and $\hat{\varepsilon} = \overline{\text{MSE}} - \overline{\text{MSE}}$ (dashed line) with $\overline{\text{MSE}} = 0.15$.

In Fig. 6.6 simulation results under the EA-rsCS strategy implemented by equation (6.15) are shown. The parameters are fixed according to the indications given in the original reference ([121]) in order to assess the set point reconstruction error, $\overline{\text{MSE}} = 0.15$. Dynamic evolution of the sampling rate probabilities and the battery energy dynamics are pictured in Fig. 6.6(a) and Fig. 6.6(b), respectively. According to (6.15), nodes locally set their own value of $p^{(i)}(k)$ on the basis of their dynamic energy battery: the lower is node's energy, the lower the value of $p^{(i)}(k)$. Differently from the S-rsCS under the EA-rsCS case we note that the network lifetime grows up to $T_l = 64 \cdot 10^3$ (Table 6.2). The reconstruction error continuously degrades over time, as shown in Fig. 6.6(c),

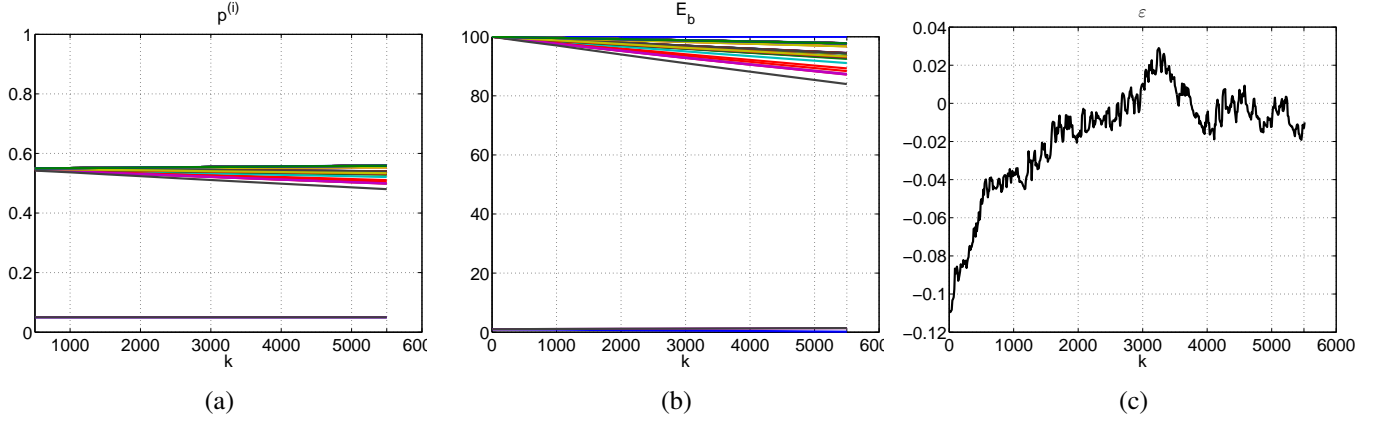


Figure 6.8.: EA-rsCS in the presence of non uniform initial battery energies and Energy Harvesting: (a) Sampling probability $p^{(i)}$; (b) Dynamic evolution of energy levels $e_i(k)$; (c) Dynamic evolution of $\varepsilon = \overline{\text{MSE}} - \text{MSE}$ with $\overline{\text{MSE}} = 0.15$.

where controller error increases during time as nodes with less energy send packets at lower rate. In this case it results $\bar{\varepsilon} = 0.0393$. The proposed TL-rsCS technique tries to stabilize the reconstruction error, also minimizing the power consumption. In Fig. 6.7 simulation results are presented for initial conditions $e_i(0) = 100J$ and $p^{(i)}(0) = p_{FC} = 0.5 \forall i$. Moreover, we assume that the MSE estimator in (9) is initialized to $\widehat{\text{MSE}}(0) = 0.15$, so that $\widehat{\varepsilon}(0) = \overline{\text{MSE}} - \widehat{\text{MSE}}(0) = 0$. By comparing Fig. 6.6(b) and Fig. 6.7(b) we note that under the proposed scheme energies spread more uniformly and, consequently, the network lifetime is extended up to $T_l = 78 \cdot 10^3$ time steps (with an increment of +22% than the Energy Aware rsCS). In addition, the FC global controller has a good regulation performance with ε controlled close to zero (continuous line in Fig. 6.7(c)). This is confirmed by the steady state reconstruction error index that is $\bar{\varepsilon} = 0.0091$ (Table 6.2).

Additionally, in Fig. 6.7(c) the dynamic evolution of the estimation error $\widehat{\varepsilon}$ (dashed line) is depicted. Notice that the estimation $\widehat{\varepsilon}$ is close to the real value ε , thus confirming the good estimation capability of (6.8) (see subplot in Fig. 6.7(c)).

	T_l	$\bar{\varepsilon}$
S-rsCS	$35 \cdot 10^3$	0.0159
EA-rsCS	$64 \cdot 10^3$	0.0393
TL-rsCS	$78 \cdot 10^3$	0.0091

Table 6.2.: Network lifetime and steady state mean error performance evaluation: nominal scenario.

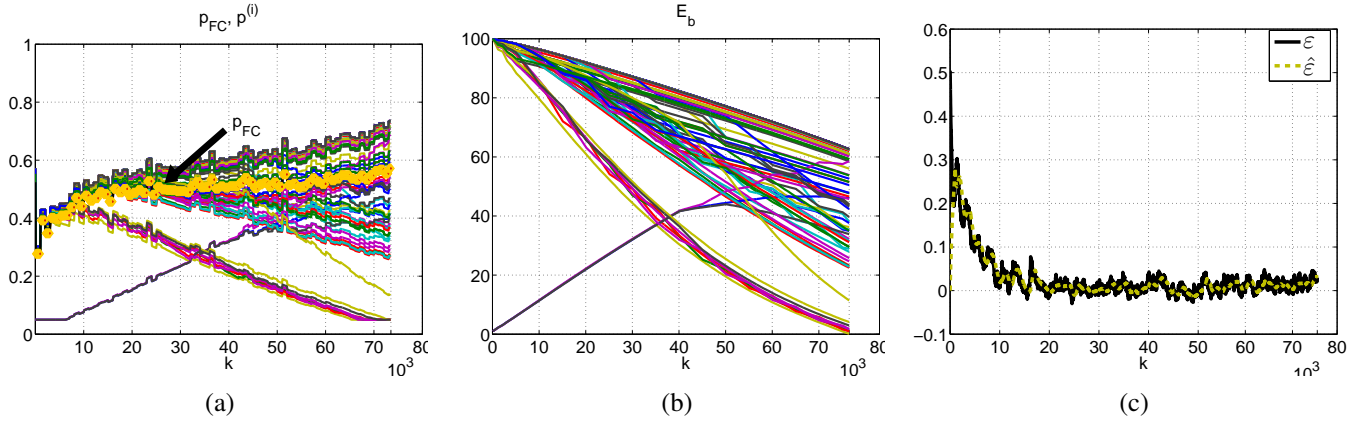


Figure 6.9.: TL-rsCS in the presence of non uniform initial battery energies and Energy Harvesting: (a) Sampling probability p^i (continuous line), sampling reference p_{FC} (thick line); (b) Dynamic evolution of energy levels $e_i(k)$; (c) Dynamic evolution of $\varepsilon = \overline{\text{MSE}} - \text{MSE}$ (continuous line) and $\hat{\varepsilon} = \overline{\text{MSE}} - \overline{\text{MSE}}$ (dashed line) with $\overline{\text{MSE}} = 0.15$.

6.5.2. Presence of Energy Harvesting process

Now, we compare the network lifetime of the proposed TL-rsCS strategy with the EA-rsCS strategy in presence of energy harvesting with $h_i(k)$, modelled as a Uniform distribution in the range $[10^{-3}, 10^{-1}]J$. To stress the effectiveness of the proposed approach, we consider the 5% of the network nodes having initial battery energy of $1J$ (i.e. much lower than the rest of nodes with initial energies of $100J$). Simulation results under the EA-rsCS and the proposed TL-rsCS strategies are respectively presented in Fig. 6.8 and Fig. 6.9. Initially the assigned sampling probabilities assume a low value for the discharged nodes (see Fig. 6.8(a) and Fig. 6.9(a)), in accordance with both $p^i(k)$ formulations (6.10) for TL-rsCS and (6.15) for EA-rsCS. Notice that under the EA-rsCS scheme nodes with low battery level may spend energy to route packets from the nodes of its upstream tree. Consequently, the resulting network lifetime may be low mainly in this scenario of energy harvesting where the available energy can be different among the network nodes. Indeed, the network lifetime results: $T_l = 6 \cdot 10^3$.

Differently, the proposed control law dynamically changes the Dijkstra's routing path according to the local controller (6.11). In this case, the network can be divided into two groups of nodes: the first one is characterized by nodes with high value of $e_i(0)$ and thus with a decreasing dynamic of the battery energy (Fig. 6.9(b)). On the other hand, the second group is composed of nodes with low $e_i(0)$ and with an increasing dynamic of battery energy. This is due to the local routing control law (6.11) that efficiently reduces the incoming rate $r_i(k)$ of nodes of the second group, thus allowing them to recharge their battery by means of the on-board harvesting system (Fig.

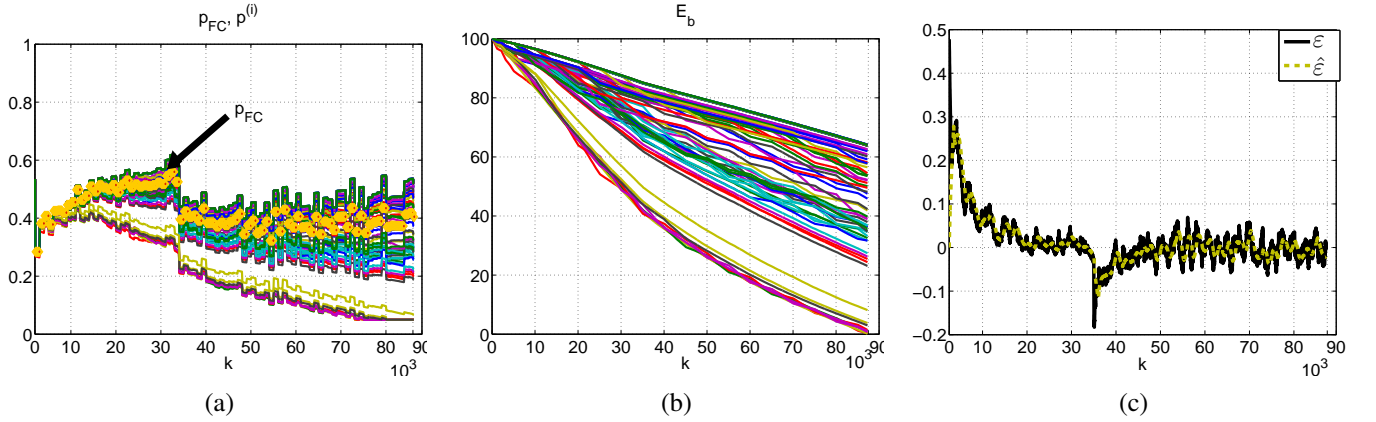


Figure 6.10.: Tracking performance of the TL-rsCS strategy: (a) Sampling probability $p^{(i)}$ and reference p_{FC} (thick line); (b) Dynamic evolution of energy levels $e_i(k)$; (c) Dynamic evolution of $\varepsilon = \overline{\text{MSE}} - \widehat{\text{MSE}}$ (continuous line) and $\widehat{\varepsilon} = \overline{\text{MSE}} - \widehat{\text{MSE}}$ (dashed line) with $\overline{\text{MSE}} = 0.15$.

6.9(b)). This strongly improves the network lifetime ($T_l = 75 \cdot 10^3$) than the EA-rsCS strategy.

Moreover, the proposed TL-rsCS strategy outperforms the EA-rsCS in terms of reconstruction error regulation, as it appears from Fig. 6.8(c) and Fig. 6.9(c). In order to point out the benefit in adopting the control law (6.11), we have carried out the simulation in the previous scenario when the control law (6.11) is not adopted. In this case, the network lifetime strongly reduces to $2.7 \cdot 10^3$ (much lower than $75 \cdot 10^3$).

6.5.3. Controller tracking performance

In this section, we validate the effectiveness of the proposed TL-rsCS scheme in the MSE regulation. Specifically, we assume that the required $\overline{\text{MSE}}$ varies from $\overline{\text{MSE}} = 0.1$ to $\overline{\text{MSE}} = 0.15$ at $k = 30 \cdot 10^3$. The global control law regulates p_{FC} (Fig. 6.10(a)) in order to steer the controller error ε close to zero (6.10(c)) despite of $\overline{\text{MSE}}$ variation. In accordance with the proposed network model, the node power consumption decreases its rate as shown in Fig. 6.10(b) because a higher $\overline{\text{MSE}}$ is required for $k \geq 30 \cdot 10^3$. This WSN monitoring system feature of dynamically adjusting the desired $\overline{\text{MSE}}$ can be very useful for example when in lack of residual energy the FC can increase the required reconstruction error in order to reduce the node consumption and in turn elongate the network lifetime.

6.6. Conclusion

In this chapter, a two-layer controller based on the Random Sampling Compressive Sensing (rsCS) has been presented. The control scheme is articulated on two levels: 1) a global controller acting at the FC level; 2) two decentralized local controllers that locally act at each node level. Specifically, the global controller is aimed to dynamically steer the CS reconstruction error to a desired value. On the other hand, two decentralized local laws have been considered to save battery energy: the first one reduces the power consumption of nodes by decreasing the local sampling rate proportionally to the residual battery energy, the second one dynamically reduces the incoming data traffic of those nodes that are in lack of residual energy by changing the Dijkstra's routing path weights. As a result, the proposed two-layer controller is able to both ensure the desired reconstruction error and extend the network lifetime.

We compared the proposed Two-Layer rsCS with other two strategies existing in literature: the Standard rsCS and the Energy Aware rsCS. The former ensures stable reconstruction error over time, but penalizes the network lifetime. Oppositely, the latter strategy increases the network lifetime but the reconstruction error degrades over time. Simulation results show that the proposed two-layer controller outperforms the above rsCS strategies, providing both higher network lifetime and good reconstruction error regulation.

Conclusions

In this dissertation, design methodology and management policies are proposed to improve EH-WSN performances in terms of traffic congestion and energy efficiency. The first part of this Thesis is focused on procedures to co-design the main EH-WSN hardware and software parameters that affect the energy efficiency of a sensor node, while in the second part dynamic control strategies have been proposed to improve EH-WSNs dynamic performances. The proposed control strategies operate at three different levels of WSN: the physical layer, the transport layer and the application layer. At the physical layer, it is proposed a hybrid supply system, composed of a battery and an ultracapacitor, to preserve battery life and prolong node energy efficiency. To this aim, a model predictive control framework based on a novel hybrid supply configuration has been formulated and studied. The second control strategy is proposed to avoid traffic congestion and extend energy efficiency of node. The control law is formulated as a convex min problem and a distributed strategy is derived by the theory of primal-dual Lagrangian decomposition. The third control law acts at the application layer to dynamically regulate the reconstruction error of a representative compression algorithm (compressive sensing) to fulfil both user requirements and the network lifetime. The controller is developed at two levels: a global controller at the FC level (application layer) and local controllers at each sensor node level (transport layer).

Besides, an additional feature that runs through the dissertation is the implementation-oriented approach. In this respect, the co-design of a EH-WSN is proposed to tune hardware and software components to achieve desired performances. In Chapter 4 a novel theoretical scheme of hybrid harvesting system is devised and a novel control strategy suitable to be practically implemented on micro-controllers is proposed. Additionally, it is also provided a hybrid harvesting demo board that, through an on-board micro-controller, gives the opportunity to test the desired control strategies (Appendix B). In Chapter 5, a control network traffic in order to avoid queue congestion and node energy fault has been proposed. A distributed algorithm is validated by an experimental test

over a small EH-WSN. The written firmware on node micro-controller, implemented in C and structured as a state machine with interrupt management, has been described. Additionally, the XReTi software that collects and shows the XBee messages in a user-friendly Java AWT interface is provided.

Appendix to Chapter 2

1. I-V model approximations

In Sec. 2.5 we have considered the Taylor approximation of $f(v_{CIN}) = \frac{1}{i_{CIN}(v_{CIN})}$ that we report for brevity:

$$f(v_{CIN}) \sim f(V_{MPP}) + f'(V_{MPP})(v_{CIN} - V_{MPP}) + \frac{f''(V_{MPP})}{2}(v_{CIN} - V_{MPP})^2$$

In fact, the considered MPPT method constrains the PV cell voltage to assume values in a short interval around the V_{MPP} value. We use the ideal PV model in the following of this paper, although a faithful PV cell model formulation can be considered ([37]). Now we derive the analytical formulation for the first and the second derivative of $f(v_{CIN})$ for $v_{CIN} = V_{MPP}$. About $f'(v_{CIN})$ it results:

$$f'(v_{CIN}) = \frac{\frac{I_0}{n_t V_t} \cdot e^{\left(\frac{v_{CIN}}{n_t V_t}\right)}}{i_{CIN}^2(v_{CIN})} = \frac{1}{n_t V_t} \frac{I_{PV} - i_{CIN}(v_{CIN})}{i_{CIN}^2(v_{CIN})} = \frac{1}{n_t V_t} \left[\frac{I_{PV}}{i_{CIN}^2(v_{CIN})} - \frac{1}{i_{CIN}(v_{CIN})} \right]$$

Similarly, $f''(v_{CIN})$ is

$$\begin{aligned} f''(v_{CIN}) &= -\frac{1}{n_t V_t} \left[\frac{2I_{PV} \cdot i_{CIN}(v_{CIN}) \cdot i'_{CIN}(v_{CIN})}{i_{CIN}^4(v_{CIN})} + f'(v_{CIN}) \right] = \left(\frac{1}{n_t V_t} \right)^2 \cdot \frac{1}{i_{CIN}(v_{CIN})} \left[\frac{2I_{PV}(I_{PV} - i_{CIN}(v_{CIN}))}{i_{CIN}^2(v_{CIN})} \right] \\ &+ \left(\frac{1}{n_t V_t} \right)^2 \left[\frac{1}{i_{CIN}(v_{CIN})} - \frac{I_{PV}}{i_{CIN}^2(v_{CIN})} \right] = \frac{1}{(n_t V_t)^2 \cdot i_{CIN}(v_{CIN})} \left[1 + \frac{2I_{PV} \cdot (I_{PV} - i_{CIN}(v_{CIN}))}{i_{CIN}^2(v_{CIN})} - \frac{I_{PV}}{i_{CIN}(v_{CIN})} \right] \\ &= \frac{1}{(n_t V_t)^2 \cdot i_{CIN}(v_{CIN})} \left[1 + \frac{I_{PV} \cdot (2I_{PV} - 3i_{CIN}(v_{CIN}))}{i_{CIN}^2(v_{CIN})} \right] \end{aligned}$$

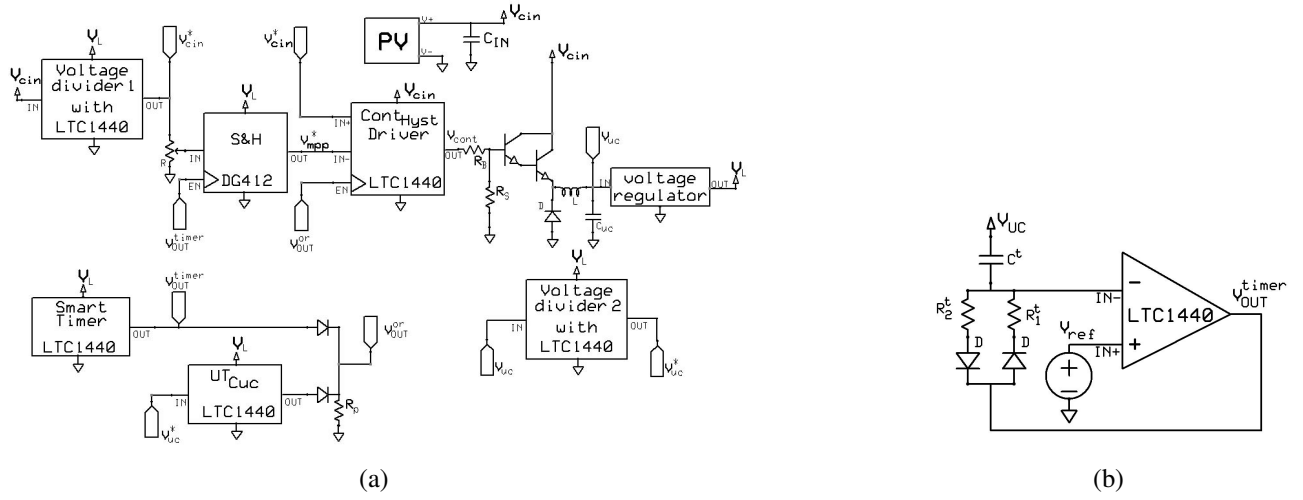


Figure A.1.: Schematic for the MPPT topology: (a) Converter and controller; (b) detail for the timer.

Then, the analytical expression of $f(v_{CIN})$ is:

$$f(v_{CIN}) \simeq \frac{1}{I_{MPP}} \left[1 + \left(\frac{1 - \sigma_I}{\sigma_I} \right) \left(\frac{v_{CIN} - V_{MPP}}{n_t \cdot V_t} \right) \right] + \frac{1}{I_{MPP}} \left[\sigma \cdot \left(\frac{v_{CIN} - V_{MPP}}{n_t \cdot V_t} \right)^2 \right] \quad (A.1)$$

with, $\sigma = \frac{\sigma_I^2 - 3\sigma_I + 2}{2 \cdot \sigma_I^2}$. By substituting (A.1) in (2.5), finally it results:

$$T'_{IN} = \frac{C_{IN} \cdot V_H}{2I_{MPP}} \left[1 - \left(\frac{1 - \sigma_I}{\sigma_I} \right) \frac{V_H}{4n_t V_t} + \sigma \frac{V_H^2}{24n_t^2 V_t^2} \right]$$

$$T''_{IN} = \frac{C_{IN} \cdot V_H}{2I_{MPP}} \left[1 + \left(\frac{1 - \sigma_I}{\sigma_I} \right) \frac{V_H}{4n_t V_t} + \sigma \frac{V_H^2}{24n_t^2 V_t^2} \right]$$

And the charging time, T_{IN}^{ch} , can be computed by:

$$T_{IN}^{ch} = T'_{IN} + T''_{IN} = \frac{C_{IN} \cdot V_H}{I_{MPP}} \left[1 + \sigma \frac{V_H^2}{24n_t^2 V_t^2} \right]$$

2. Detailed description of the MPPT topology circuitry

In Fig. A.1 we describe the details of the circuitry implementation of the proposed MPPT topology. Letting $V_L = 3.3$ V be the stabilized load supply voltage, and v_{CIN} the PV voltage, the aim of the controller is to assess $v_{CIN} = V_{MPP}$ and $V_{UC} \leq V_{UC}^{max}$ where V_{MPP} and V_{UC}^{max} are respectively the

Component	Part Name	Nominal characteristics
Hysteretic Comparator (LTC1440)	"Voltage divider 1-2", "Driver", "Smart Timer", " $UT_{C_{UC}}$ "	$\simeq 6\mu A$ at 3.3 V
Sample and Hold (DG412)	"S&H"	$\simeq 5\mu A$ at 3.3 V
LDO regulator (MPC1702)	"voltage regulator"	$\simeq 3.3\mu A$ at 3.3 V
input capacitor	" C_{IN} "	$C_{IN} = 220\mu F$ $ESR < 10m\Omega$
NPN Switcher Power Transistor		$V_{C_{DROP}}^{min} = 1V$ with $i_{C_{IN}} = 100mA$

Table A.1.: Electric characteristics for the MPPT topology scheme.

maximum power point and the maximum UC voltage. In order to reduce the power consumption and to use a low power supplied device, the proposed scheme considers the fractions $v_{C_{IN}}^* = 0.2v_{C_{IN}}$ and $V_{UC}^* = 0.5V_{UC}$ of the measured variables. Similarly, V_{MPP} is scaled as $V_{MPP}^* = 0.2\sigma_V V_{OC}$. The above variable reductions are implemented by the "Voltage divider 1" and "Voltage divider 2" in Fig. A.1(a). The tracking of the V_{MPP} is implemented by the $Cont_{Hyst}$ Driver block (LTC1440). The condition $V_{UC} \leq V_{UC}^{max}$ is ensured by the " $UT_{C_{UC}}$ " block. Indeed, the block disables the Driver (i.e. the energy transfer to the UC) if $V_{UC} > V_{UC}^{max}$. The scaled measured variables are sampled and hold by the device "DG412" in Fig. A.1(a). The "Smart Timer" block [128, 129] that is implemented by the LTC1440 component, enables the S&H device and inhibits the charging process during the sample time. The scheme is completed by the converter, UC and load. The load voltage is stabilized by the "MPC1702" component that is a voltage stabilizer with low leakage current, suitable for low power applications. Notice that the PV cell directly supplies the Driver.

The design effort is focused on the reduction in static power consumption. The following ICs have been used to implement the prototype:

a) the "Voltage dividers", "Driver" and " $UT_{C_{UC}}$ " have been implemented by the IC LTC1440 that is an Ultra Low Power Single Comparator;

b) the "Smart Timer" has been implemented by the LTC1440 as shown in Fig. A.1(b). It generates a square waveform according to the following behavior. The voltage at the terminal IN^+ is fixed at a self-generated reference voltage, $V^{IN^+} = V_{ref}$. When $V^{IN^+} > V^{IN^-}$, $V_{OUT}^{timer} = 1$ for the time interval spent to charge the capacitance C^t . The time interval depends on the time constant $\tau_1 = R_1^t \cdot C^t$. This holds until $V^{IN^-} > V^{IN^+}$. When $V^{IN^-} > V^{IN^+}$ then $V_{OUT}^{timer} = 0$. In this situation, the voltage

to the terminal IN^- decreases by virtue of the effect of the C^t discharge according to the time constant $\tau_2 = R_2^t \cdot C^t$. The above timer consumes less energy than the standard one NE555 usually used in the literature [31].

As depicted in Fig. A.1(a), the proposed controller topology is not supplied by an external battery, but uses both the PV cell and the UC as energy sources. We have experimentally measured the mean solar harvesting controller power absorption $\bar{P}_{cnt} \sim 330\mu W$. On the base of data sheet component characteristics in TABLE A.1 the computed static power consumption of controller components as $\bar{P}_{cnt} = 130\mu W$ lower than the measured one because it does not take into account of the power dynamic consumption as well as the passive resistive components used for the circuit polarization. Moreover, the overall measured efficiency $\bar{\eta}_{me}$ is greater than η_{MIN} because the measured controller power consumption is low ($\bar{P}_{cnt} \sim 330\mu W$)

Appendix to Chapter 4

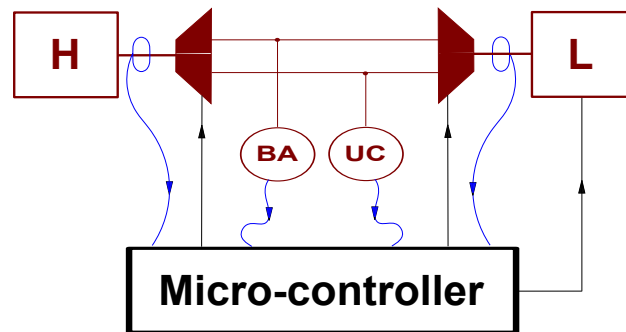


Figure B.1.: Hardware implementation for the hybrid system scheme in Fig. 4.2.

An hardware implementation of the proposed supply system in Fig. 4.2 is proposed in this Appendix. In Fig. B.1 the block scheme summarizes the system implementation. In particular: 1) red lines and blocks are the power logic chain where energy is converted from harvesting, is collected into batteries and is provided on demand to a load. Trapezes are two selectable electronic switchers, the first one is adopted to select the battery or the ultracapacitor from recharge and the second is used to supply node from one of the two devices; 2) black lines and blocks, are aimed at the supply system control, through a micro-controller; 3) blue lines represent voltage and current probes to monitor and measure the state of the hybrid system.

Block scheme in Fig. B.1 has the following characteristics:

1. composed of battery and ultracapacitor as well;
2. able to recharge both battery and the ultracapacitor (on selection) from a renewable source, such as solar or vibrations;
3. able to supply a load (e.g. a WSn) from one of battery and ultracapacitor, on selection;

4. able to trigger node duty cycle allocation;
5. integrates a micro-controller to manage the energy from harvesting source and to the load by selectively choosing which device to use.

With the use of the on-board micro-controller, it is possible to orchestrate the energy management policy by measuring the system state (harvesting and load currents, battery and ultracapacitor drop out voltage) and by controlling system input and output switchers and the duty cycle of the node. Notice that the proposed implementation scheme is a versatile demo board for energy management strategy development, since different strategies and hybrid schemes (such as those shown in Fig. 4.1.(a)-(e)) can be coded into a suitable firmware to be uploaded into micro-controller.

Hardware Overview

Main hardware components included for the implementation of the above electronic scheme are presented in this section.

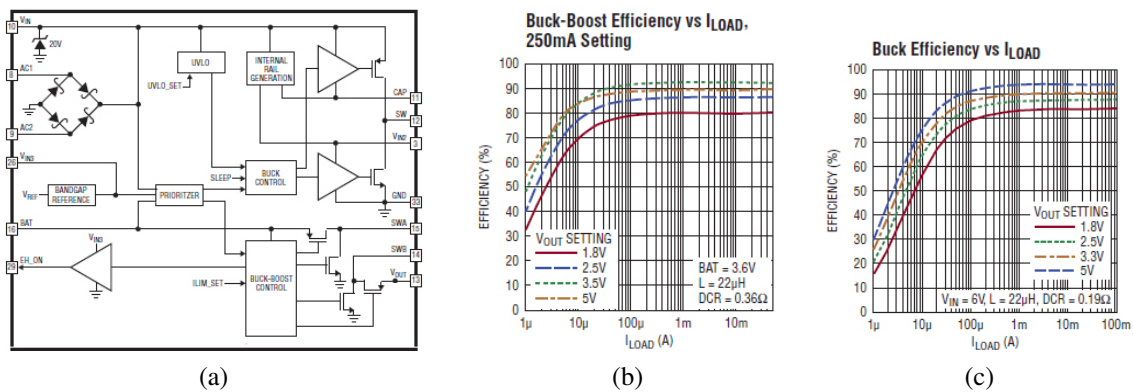


Figure B.2.: From LTC3330 Datasheet: Efficiency of the integrated (a) Buck-Boost Converter and (b) Buck Converter under different current load conditions.

H and L blocks They are two dc/dc converters that provide suitable regulated voltage from the harvesting and to supply the node. The core of these blocks is the IC LTC3330 device from Linear Technology. The LTC3330 is a 5mm x 5mm QFN-32 Package that combines renewable energy from a harvesting source and energy stored from a backup battery to deliver power to a stable voltage output supply. Internally, the LTC3330 is built with a buck switching regulator for the harvesting conversion, while a buck-boost switching regulator converts backup battery energy to the output. Converters are controlled by an internal prioritizer that selects which conversion branch

is to be used, (Fig. B.2a). It is a threshold-based controller that uses the harvesting source (the buck converter branch), if harvested energy suffices to supply the output, otherwise it uses the battery (the buck-boost branch). In this case, the LTC3330 buck branch polarizes the harvesting device within preassigned voltage ranges in order to orchestrate the maximum power point polarization of the harvesting source. The device suits many applications such as: Energy Harvesting, Solar Powered Systems with Primary Cell Backup, Wireless HVAC Sensors and so on. Additionally, the declared IC conversion efficiency can be above the 90%. In Fig. B.2 the efficiency of the LTC3330 is reported. As can be seen, better efficiency of conversion can be achieved by setting up the output voltage to 3.5V. Additionally, to cope with internal losses, ideal configuration performs better if a current load greater than 1mA is supplied. Finally, as suggested by datasheet, better efficiency performance is obtained with a 22μH output switching inductor.

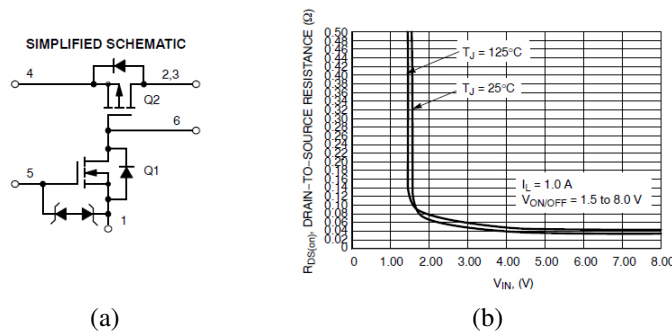


Figure B.3.: From NTGD1100L Datasheet: a) Simplified Internal scheme; b) Series ON resistance as function of input voltage.

Switchers Trapezes blocks are implemented through the NTGD1100L block that is a discrete switcher in P-mos pass transistor configuration. It integrates a P- and N- Channel MOSFET in a single package, in configuration of Fig. B.3a. This device is particularly suited for portable electronic equipment where low control signals, low input voltages and high currents are needed. The P-Channel device is specifically designed using ON Semiconductor state-of-art trench technology. The N-Channel MOSFET functions as a level-shifter to drive the P-Channel. The N-Channel MOSFET has internal ESD protection and can be driven by logic signals as low as 1.5V. The NTGD1100L operates on supply lines from 1.8V to 8.0V and can drive loads up to 3.3A with 8.0V applied to both the input (pin 4) and the control line (pin 5). Features of this device are: a) input voltage in range 1.8V to 8.0V; c) control line voltage in range 1.5 to 8.0V; b) extremely low series resistance for input voltages greater than 2V (Fig. B.3b).

Microcontroller block unit A micro-controller is used to manage the hybrid system. If, in principle, every micro-controller can be used for this purpose (low power PIC, dsPIC, etc.), the selection of this component is strictly related to the computation required to manage the board and the power consumption. Algorithms such as the conservative and the adaptive policies can be implemented with low power micro-controllers, while dsPICs are typically adopted to develop model predictive control computations ([130]).

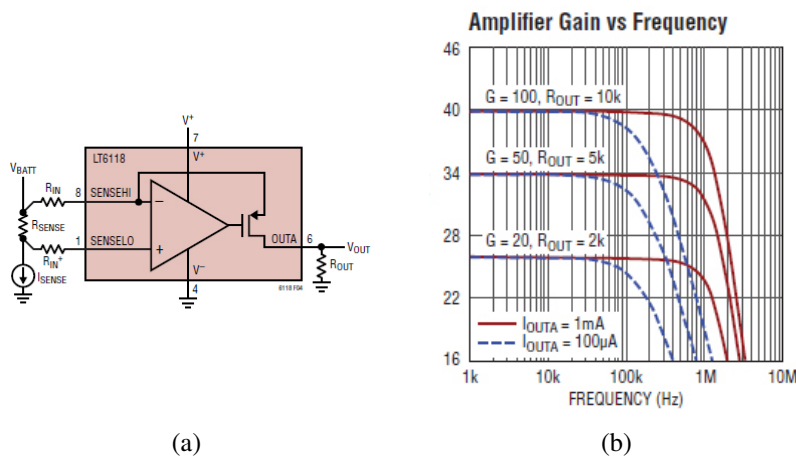


Figure B.4.: From LT6118 Datasheet: a) Simplified Internal scheme and polarization; b) Amplifier gain vs. input frequency.

Voltage and Current probes The LT6118 is a 8-Lead MSOP high side current sense device that incorporates a precision current sense amplifier, an integrated voltage reference and a latching comparator. The input and the open-drain output of the comparator are independent from the current sense amplifier. The amplifier gain is configured with external resistors. The 1MHz bandwidth allows the LT6118 to be used for precise current-to-voltage amplifier. Voltage references are read by the micro-controller through the integrated ADC converters.

System sizing

The sizing of circuit components has been selected according to the previous experience reported in Chapter 2 and Appendix A. In particular the following "rules" for the hardware design are applied:

1. reducing the number of circuit components and using low power active circuits;
2. reducing, whenever possible, resistive paths through the ground or choosing high impedance paths if present;

- power paths may be obtained with low path impedance in order to avoid power dissipation along the wire, therefore short and thick wires should be considered.

About the dimensioning of block H, the formulation of the harvesting conversion and system autonomy in Chapter 2 can be considered. In particular, $C_{UC} = 20F$ is chosen by considering equ. (2.13) and $P_{MPP} = 900mW$. Moreover, about harvesting efficiency, from equ. (2.7), can be selected $V_H = 1V$, that gives a theoretical input conversion efficiency of about 91% having assumed $\sigma = 0.76$, $n_t = 15$ and $V_t = 0.025V$. From equation (2.23) the output conversion efficiency formulation can be considered in principle to select a proper size of the switching induction and input capacitance, since the LTC3330 uses a buck converter to harvest the energy, the same converter configuration that is used into the experimentation carried out in Chapter 2. However, in this specific case, the manufacturer documentation is considered instead. In particular, the LCT3330 is optimized to work with a switching inductor of $22\mu H$ value and a maximum input capacitance of $200\mu F$, which ensures also the inductor peak current to be at its maximum ($250mA$). With the settings considered, from manufacturer's output conversion plot in Fig. B.2.(a), we have $\eta_{TP} > 90\%$.

Board topology overview and PCB realization

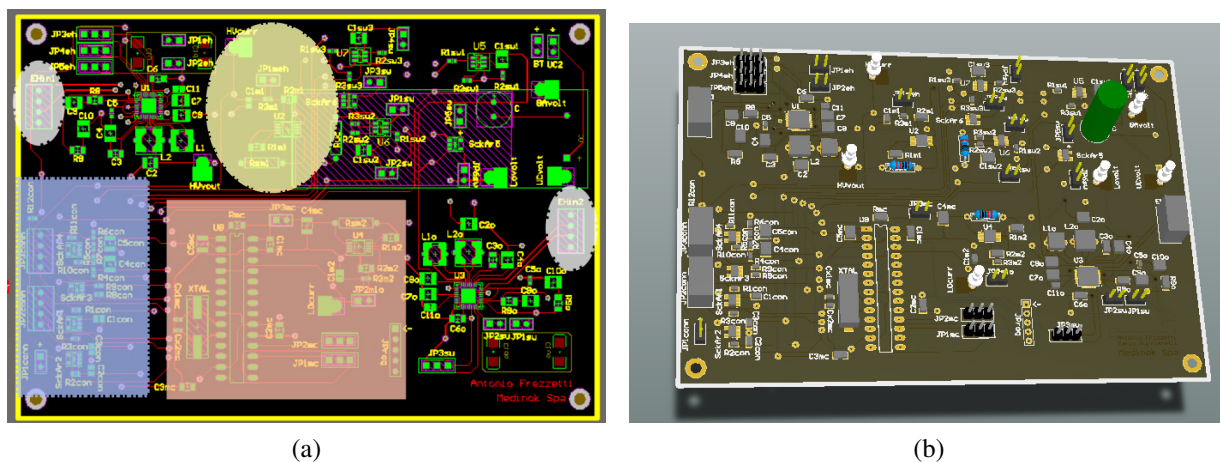


Figure B.5.: CAD design of the Smart Harvester board (Altium Designer): a) PCB layout and b) 3D view.

In Fig. B.5 the PCB layout and the 3D view of the project are shown. In Fig. B.5a, four main areas of the Smart Hybrid Harvester board are highlighted. White shaded ovals represent the power inputs, from which renewable sources (e.g. solar, vibrations, thermal, RF or grid) can be connected



Figure B.6.: A photo of the proposed hybrid system scheme.

to the board. Red shaded box is the micro-controller section. Yellow oval is one of the two units used to probe current from harvesting. Blue box is the output where signal is level-shifted, and power is delivered to the load. The remaining part of the board logic manages power from the harvesting, collects energy into the accumulation devices (that have been placed on the bottom side of the board) and provides power to the output. Finally, in Fig. B.6 a photo of the fabricated PCB board has been reported.

Appendix to Chapter 5

1. Primal-Dual convergence

In this section, the main result in [107] is reported. Let consider the dynamic system (5.3)-(5.4) and the target primal problem given in (5.7) with utility function U_i defined as:

$$U_i(g_i) = \int f_i(g_i) dg_i \quad (\text{C.1})$$

Additionally, let define the following conditions:

- (C1) For all $i \in \mathbf{N}$, F_i and γ_i are nonnegative functions so that g_i and ρ_i are non-negative variables. Moreover, equilibrium points of system equations, namely $\bar{g}_i \forall i$, exist.
- (C2) For all i , F_i are continuously differentiable and $\frac{\delta F_i}{\delta q_i} \neq 0 \in \{(g_i, q_i) | g_i > 0, q_i > 0\}$. Moreover, f_i in (5.5) is a nonincreasing function.
- (C3) Let $(\bar{\rho}_i, \bar{r}_i) \forall i$ denote the penalty and the aggregate rate at node i at the equilibrium. If $\gamma_i(\bar{\rho}_i, \bar{r}_i) = 0$ then $\bar{r}_j \leq c_j$ with equality if $\bar{\rho}_j > 0$.
- (C4) For all i , f_i are strictly decreasing functions.

Theorem A

Suppose assumptions (C1) and (C2) hold. Then the equilibrium state of dynamic system (5.3)-(5.4) exists. Additionally, $(\bar{g}_i, \bar{\rho}_i)$ solves both primal problem (5.7) and the corresponding dual problem if and only if condition (C3) holds. Finally, if assumption (C4) holds, then U_i are strictly concave $\forall i$ and the optimal vector $\mathbf{g}^* = [g_i^*]$ of primal problem is unique and then $\bar{g}_i = g_i^* \forall i$.

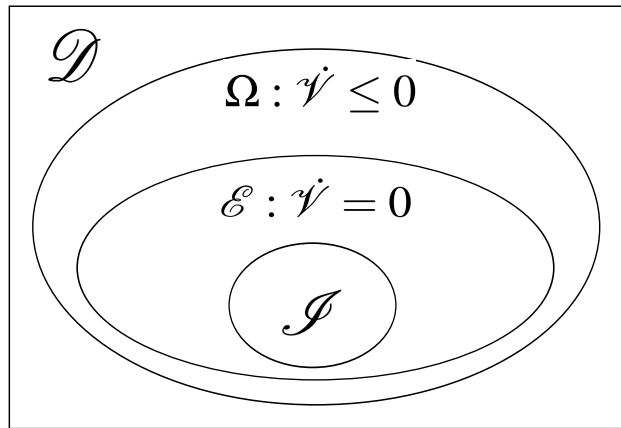


Figure C.1.: Set definition for the LaSalle invariance principle.

2. LaSalle Invariance Principle

Consider the generic dynamic equation:

$$\dot{x} = f(x(t)) \tag{C.2}$$

Let $\Omega \subset \mathcal{D} \subset \mathbb{R}$ be a set positively invariant with respect to (C.2). Let $\mathcal{V} : \mathcal{D} \rightarrow \mathbb{R}$ be a continuous differentiable function such that $\dot{\mathcal{V}} \leq 0$ in Ω . Let \mathcal{E} be the set of all points in Ω where $\dot{\mathcal{V}} = 0$. Let additionally \mathcal{I} be the largest invariant set in \mathcal{E} . Then, every solution starting in Ω approaches \mathcal{I} as $t \rightarrow \infty$.

The second corollary of LaSalle Invariance Principle, also known as Krasovskii's theorem, is enunciated. Let $x = 0$ be an equilibrium point for (C.2). Let $\mathcal{V} : \mathcal{D} \rightarrow \mathbb{R}$ be a continuous differentiable, radially unbounded function such that $\dot{\mathcal{V}} \leq 0$ in Ω . Let \mathcal{E} be the set of all points in Ω where $\dot{\mathcal{V}} = 0$ and suppose that no solution can stay identically in \mathcal{E} other than the trivial solution $x(t) = 0$. Then, the origin is globally asymptotically stable.

Bibliography

- [1] Jennifer Yick, Biswanath Mukherjee, and Dipak Ghosal. Wireless sensor network survey. *Computer networks*, 52(12):2292–2330, 2008.
- [2] Ian F Akyildiz, Weilian Su, Yogesh Sankarasubramaniam, and Erdal Cayirci. Wireless sensor networks: a survey. *Computer networks*, 38(4):393–422, 2002.
- [3] Th Arampatzis, John Lygeros, and S Manesis. A survey of applications of wireless sensors and wireless sensor networks. In *Intelligent Control, 2005. Proceedings of the 2005 IEEE International Symposium on, Mediterrean Conference on Control and Automation*, pages 719–724. IEEE, 2005.
- [4] Paolo Baronti, Prashant Pillai, Vince WC Chook, Stefano Chessa, Alberto Gotta, and Y Fun Hu. Wireless sensor networks: A survey on the state of the art and the 802.15. 4 and zigbee standards. *Computer communications*, 30(7):1655–1695, 2007.
- [5] Carlos F García-Hernández, Pablo H Ibarguengoytia-Gonzalez, Joaquín García-Hernández, and Jesús A Pérez-Díaz. Wireless sensor networks and applications: a survey. *IJCSNS International Journal of Computer Science and Network Security*, 7(3):264–273, 2007.
- [6] Cauligi S Raghavendra, Krishna M Sivalingam, and Taieb Znati. *Wireless sensor networks*. Springer, 2006.
- [7] Taieb Znati, Cauligi Raghavendra, and Krishna Sivalingam. Guest editorial: special issue on wireless sensor networks. *Mobile Networks and Applications*, 8(4):425–425, 2003.
- [8] Bhaskar Krishnamachari. A wireless sensor networks bibliography. *Autonomous Networks Research Group, University of Southern California-Los Angeles*, 103, 2007.
- [9] Charlie Chi and Mareca Hatler. Wireless sensor network. mass market opportunities. *ON World Inc*, 2004.

- [10] Roberto Faranda and Sonia Leva. Energy comparison of mppt techniques for pv systems. *WSEAS transactions on power systems*, 3(6):446–455, 2008.
- [11] Alex Phipps and Toshikazu Nishida. System modeling of piezoelectric energy harvesters. *IEEE Transactions on Power Electronics*, 27(2):790–802, 2012.
- [12] Ko Ko Win, Souvik Dasgupta, and SK Panda. An optimized mppt circuit for thermoelectric energy harvester for low power applications. In *IEEE 8th International Conference on Power Electronics and ECCE Asia (ICPE & ECCE)*, pages 1579–1584. IEEE, 2011.
- [13] Soudeh Heydari Nasab, Mohammad Asefi, Lutfi Albasha, and Naser Qaddoumi. Investigation of rf signal energy harvesting. *Active and Passive Electronic Components*, 2010, 2010.
- [14] J Kurose, V Lesser, E de Sousa e Silva, A Jayasumana, and B Liu. Sensor networks seminar. *CMPSCI 791L, University of Massachusetts, Amherst, MA, Fall*, 2003.
- [15] Philo Juang, Hidekazu Oki, Yong Wang, Margaret Martonosi, Li Shiuan Peh, and Daniel Rubenstein. Energy-efficient computing for wildlife tracking: Design tradeoffs and early experiences with zebranet. *ACM Sigplan Notices*, 37(10):96–107, 2002.
- [16] Andreas Willig. Recent and emerging topics in wireless industrial communications: A selection. *IEEE Transactions on Industrial Informatics*, 4(2):102–124, 2008.
- [17] Francisco Díaz-González, Andreas Sumper, Oriol Gomis-Bellmunt, and Roberto Villafáfila-Robles. A review of energy storage technologies for wind power applications. *Renewable and Sustainable Energy Reviews*, 16(4):2154–2171, 2012.
- [18] Susan M Schoenung. Characteristics and technologies for long-vs. short-term energy storage. *United States Department of Energy*, 2001.
- [19] W Gu, Z Wu, and X Yuan. Microgrid economic optimal operation of the combined heat and power system with renewable energy. In *Power and Energy Society General Meeting, 2010 IEEE*, pages 1–6. IEEE, 2010.
- [20] Sudipta Chakraborty and M Godoy Simoes. Pv-microgrid operational cost minimization by neural forecasting and heuristic optimization. In *Industry Applications Society Annual Meeting, 2008. IAS'08. IEEE*, pages 1–8. IEEE, 2008.
- [21] Joao P Hespanha, Payam Naghshtabrizi, and Yonggang Xu. A survey of recent results in networked control systems. *PROCEEDINGS-IEEE*, 95(1):138, 2007.

- [22] James R Moyne and Dawn M Tilbury. The emergence of industrial control networks for manufacturing control, diagnostics, and safety data. *Proceedings of the IEEE*, 95(1):29–47, 2007.
- [23] US DoE. Industrial wireless technology for the 21st century. *Technology Foresight*, 2004.
- [24] Wendi B Heinzelman, Anantha P Chandrakasan, and Hari Balakrishnan. An application-specific protocol architecture for wireless microsensor networks. *IEEE Transactions on Wireless Communications*, 1(4):660–670, 2002.
- [25] Qin Wang and Woodward Yang. Energy consumption model for power management in wireless sensor networks. In *4th Annual IEEE Communications Society Conference on Sensor, Mesh and Ad Hoc Communications and Networks, 2007. SECON'07*, pages 142–151. IEEE, 2007.
- [26] Patrik Moravek, Dan Komosny, Milan Simek, and Lubomir Mraz. Energy demands of 802.15. 4/zigbee communication with iris sensor motes. In *34th International Conference on Telecommunications and Signal Processing (TSP)*, pages 69–73. IEEE, 2011.
- [27] Antonio Frezzetti, Sabato Manfredi, and Andrea Suardi. Adaptive focv-based control scheme to improve the mpp tracking performance: an experimental validation. volume 19, pages 4967–4971, 2014.
- [28] A Frezzetti, S Manfredi, and M Pagano. A pv-model based design of a mppt controller for energy harvested wireless sensor nodes, 2 ifac workshop on convergence of information technologies and control methods with power systems-icps13, cluj- napoca. *Romania, May*, pages 22–24.
- [29] Sehwan Kim, Keun-Sik No, and Pai H Chou. Design and performance analysis of supercapacitor charging circuits for wireless sensor nodes. *IEEE Journal on Emerging and Selected Topics in Circuits and Systems*, 1(3):391–402, 2011.
- [30] Fouad Rafik, Hamid Gualous, Roland Gallay, Albert Crausaz, and Alain Berthon. Frequency, thermal and voltage supercapacitor characterization and modeling. *Journal of power sources*, 165(2):928–934, 2007.
- [31] Oscar Lopez-Lapena, Maria Teresa Penella, and Manel Gasulla. A closed-loop maximum power point tracker for subwatt photovoltaic panels. *IEEE Transactions on Industrial Electronics*, 59(3):1588–1596, 2012.

- [32] Davide Brunelli, Clemens Moser, Lothar Thiele, and Luca Benini. Design of a solar-harvesting circuit for batteryless embedded systems. *IEEE Transactions on Circuits and Systems I: Regular Papers*, 56(11):2519–2528, 2009.
- [33] Denis Dondi, Alessandro Bertacchini, Davide Brunelli, Luca Larcher, and Luca Benini. Modeling and optimization of a solar energy harvester system for self-powered wireless sensor networks. *IEEE Transactions on Industrial Electronics*, 55(7):2759–2766, 2008.
- [34] Farhan Simjee, Pai H Chou, et al. Efficient charging of supercapacitors for extended lifetime of wireless sensor nodes. *IEEE Transactions on Power Electronics*, 23(3):1526–1536, 2008.
- [35] Cesare Alippi and Cristian Galperti. An adaptive system for optimal solar energy harvesting in wireless sensor network nodes. *IEEE Transactions on Circuits and Systems I: Regular Papers*, 55(6):1742–1750, 2008.
- [36] J Alberola, J Pelegri, R Lajara, and Juan J Perez. Solar inexhaustible power source for wireless sensor node. In *Instrumentation and Measurement Technology Conference Proceedings, 2008. IMTC 2008. IEEE*, pages 657–662. IEEE, 2008.
- [37] Cuauhtemoc Rodriguez and Gehan AJ Amaratunga. Analytic solution to the photovoltaic maximum power point problem. *IEEE Transactions on Circuits and Systems I: Regular Papers*, 54(9):2054–2060, 2007.
- [38] Texas instruments ez430-rf4500 datasheet.
- [39] Giuseppe Carannante, Ciro Fraddanno, Mario Pagano, and Luigi Piegari. Experimental performance of mppt algorithm for photovoltaic sources subject to inhomogeneous insolation. *IEEE Transactions on Industrial Electronics*, 56(11):4374–4380, 2009.
- [40] Trishan ESRAM, Patrick L Chapman, et al. Comparison of photovoltaic array maximum power point tracking techniques. *IEEE Transactions on Energy Conversion EC*, 22(2):439, 2007.
- [41] Jonghoon Kim and Bo-Hyung Cho. State-of-charge estimation and state-of-health prediction of a li-ion degraded battery based on an ekf combined with a per-unit system. *IEEE Transactions on Vehicular Technology*, 60(9):4249–4260, 2011.
- [42] Joseph H Rockett. Losses in high-power bipolar transistors. *IEEE Transactions on Power Electronics*, (1):72–80, 1987.
- [43] Pressman. *Switching Power Supply Design*.

- [44] Giuseppe Anastasi, Marco Conti, Mario Di Francesco, and Andrea Passarella. Energy conservation in wireless sensor networks: A survey. *Ad hoc networks*, 7(3):537–568, 2009.
- [45] Celalettin Karakus, Ali Cafer Gurbuz, and Bulent Tavli. Analysis of energy efficiency of compressive sensing in wireless sensor networks. *IEEE Sensors Journal*, 13(5):1999–2008, 2013.
- [46] Kemal Akkaya and Mohamed Younis. A survey on routing protocols for wireless sensor networks. *Ad hoc networks*, 3(3):325–349, 2005.
- [47] David L Donoho. Compressed sensing. *IEEE Transactions on Information Theory*, 52(4):1289–1306, 2006.
- [48] Emmanuel J Candes and Terence Tao. Decoding by linear programming. *IEEE Transactions on Information Theory*, 51(12):4203–4215, 2005.
- [49] Emmanuel J Candes and Terence Tao. Near-optimal signal recovery from random projections: Universal encoding strategies? *IEEE Transactions on Information Theory*, 52(12):5406–5425, 2006.
- [50] Emmanuel J Candes, Justin K Romberg, and Terence Tao. Stable signal recovery from incomplete and inaccurate measurements. *Communications on pure and applied mathematics*, 59(8):1207–1223, 2006.
- [51] Yongyou Yang. An experimental analysis for compressive sensing in wireless sensor networks. In *2nd International Conference on Consumer Electronics, Communications and Networks (CECNet)*, pages 2372–2375. IEEE, 2012.
- [52] Gang Yang, Vincent YF Tan, Chin Keong Ho, See Ho Ting, and Yong Liang Guan. Wireless compressive sensing for energy harvesting sensor nodes. *IEEE Transactions on Signal Processing*, 61(18):4491–4505, 2013.
- [53] Wei Chen and Ian J Wassell. Energy-efficient signal acquisition in wireless sensor networks: a compressive sensing framework. *IET wireless sensor systems*, 2(1):1–8, 2012.
- [54] Marco F Duarte, Shriram Sarvotham, Dror Baron, Michael B Wakin, and Richard G Baraniuk. Distributed compressed sensing of jointly sparse signals. In *Asilomar Conf. Signals, Sys., Comput*, pages 1537–1541, 2005.

- [55] Fatemeh Fazel, Maryam Fazel, and Milica Stojanovic. Random access compressed sensing in underwater sensor networks. In *48th Annual Allerton Conference on Communication, Control, and Computing (Allerton)*, pages 768–774. IEEE, 2010.
- [56] Carlo Caione, Davide Brunelli, and Luca Benini. Compressive sensing optimization for signal ensembles in wsns. *IEEE Transactions on Industrial Informatics*, 10(1):382–392, 2014.
- [57] Vinay Sachidananda, David Noack, Abdelmajid Khelil, Kristof Van Laerhoven, and Philipp M Scholl. Optimized multi-attribute co-design for maximizing efficiency in wireless sensor networks. In *IEEE Tenth International Conference on Intelligent Sensors, Sensor Networks and Information Processing (ISSNIP)*, pages 1–6. IEEE, 2015.
- [58] Vinay Sachidananda, Abdelmajid Khelil, David Noack, and Neeraj Suri. Information quality aware co-design of sampling and transport in wireless sensor networks. In *Wireless and Mobile Networking Conference (WMNC), 2013 6th Joint IFIP*, pages 1–8. IEEE, 2013.
- [59] Chih-Ming Hsieh, Farzad Samie, M Sammer Srouji, Manyi Wang, Zhonglei Wang, and Jörg Henkel. Hardware/software co-design for a wireless sensor network platform. In *Proceedings of the 2014 International Conference on Hardware/Software Codesign and System Synthesis*, page 1. ACM, 2014.
- [60] Rainer Zelinski and Peter Noll. Adaptive transform coding of speech signals. *IEEE Transactions on Acoustics, Speech and Signal Processing*, 25(4):299–309, 1977.
- [61] Vivek K Goyal. Theoretical foundations of transform coding. *IEEE Signal Processing Magazine*, 18(5):9–21, 2001.
- [62] Emmanuel J Candès and Michael B Wakin. An introduction to compressive sampling. *IEEE Signal Processing Magazine*, 25(2):21–30, 2008.
- [63] Andrew Chu and Paul Braatz. Comparison of commercial supercapacitors and high-power lithium-ion batteries for power-assist applications in hybrid electric vehicles: I. initial characterization. *Journal of power sources*, 112(1):236–246, 2002.
- [64] Aurelien Du Pasquier, Irene Plitz, Serafin Menocal, and Glenn Amatucci. A comparative study of li-ion battery, supercapacitor and nonaqueous asymmetric hybrid devices for automotive applications. *Journal of Power Sources*, 115(1):171–178, 2003.

- [65] Jim P Zheng, T Richard Jow, and MS Ding. Hybrid power sources for pulsed current applications. *IEEE Transactions on Aerospace and Electronic Systems*, 37(1):288–292, 2001.
- [66] Roger A Dougal, Shengyi Liu, and Ralph E White. Power and life extension of battery-ultracapacitor hybrids. *IEEE Transactions on Components and Packaging Technologies*, 25(1):120–131, 2002.
- [67] Lijun Gao, Roger A Dougal, and Shengyi Liu. Power enhancement of an actively controlled battery/ultracapacitor hybrid. *IEEE Transactions on Power Electronics*, 20(1):236–243, 2005.
- [68] J Bauman and M Kazerani. An improved powertrain topology for fuel cell-battery-ultracapacitor vehicles. In *IEEE International Symposium on Industrial Electronics, ISIE*, pages 1483–1488. IEEE, 2008.
- [69] Mamadou Baïo Camara, Hamid Gualous, Frederic Gustin, Alain Berthon, and Brayima Dakyo. Dc/dc converter design for supercapacitor and battery power management in hybrid vehicle applications—polynomial control strategy. *IEEE Transactions on Industrial Electronics*, 57(2):587–597, 2010.
- [70] Zhao Qinghua, Li Hua, Wei Zhang, and Li Hongyan. Design of new power management system in wireless sensor network. In *IEEE 5th International Conference on Wireless Communications, Networking and Mobile Computing WiCom'09*, pages 1–4. IEEE, 2009.
- [71] Jordan Varley, Matthew Martino, Shahab Poshtkouhi, and Olivier Trescases. Battery and ultra-capacitor hybrid energy storage system and power management scheme for solar-powered wireless sensor nodes. In *IECON 2012-38th Annual Conference on IEEE Industrial Electronics Society*, pages 4806–4811. IEEE, 2012.
- [72] Kumar V Naveen and SS Manjunath. A reliable ultracapacitor based solar energy harvesting system for wireless sensor network enabled intelligent buildings. In *IEEE 2nd International Conference on Intelligent Agent and Multi-Agent Systems (IAMA)*, pages 20–25. IEEE, 2011.
- [73] Fabio Ongaro, Stefano Saggini, and Paolo Mattavelli. Li-ion battery-supercapacitor hybrid storage system for a long lifetime, photovoltaic-based wireless sensor network. *IEEE Transactions on Power Electronics*, 27(9):3944–3952, 2012.

- [74] John Miller, Patrick J McCleer, and Mark Cohen. Energy buffers. *Maxwell Technologies White Paper*, 2004.
- [75] Cyrus Ashtiani, Randy Wright, and Gary Hunt. Ultracapacitors for automotive applications. *Journal of Power Sources*, 154(2):561–566, 2006.
- [76] Branislav Hredzak and Vassilios G Agelidis. Model predictive control of a hybrid battery-ultracapacitor power source. In *Power Electronics and Motion Control Conference (IPEMC), 2012 7th International*, volume 3, pages 2294–2299. IEEE, 2012.
- [77] Branislav Hredzak, Vassilios Georgios Agelidis, and Minsoo Jang. A model predictive control system for a hybrid battery-ultracapacitor power source. *IEEE Transactions on Power Electronics*, 29(3):1469–1479, 2014.
- [78] Brian E Conway. *Electrochemical supercapacitors: scientific fundamentals and technological applications*. Springer Science & Business Media, 2013.
- [79] Min Chen, Gabriel Rincón-Mora, et al. Accurate electrical battery model capable of predicting runtime and iv performance. *IEEE transactions on Energy conversion*, 21(2):504–511, 2006.
- [80] Ala Al-haj Hussein and Issa Batarseh. An overview of generic battery models. In *Power and Energy Society General Meeting, 2011 IEEE*, pages 1–6. IEEE, 2011.
- [81] O Erdinc, B Vural, and M Uzunoglu. A dynamic lithium-ion battery model considering the effects of temperature and capacity fading. In *International Conference on Clean Electrical Power*, pages 383–386. IEEE, 2009.
- [82] Kannan Thirugnanam, Himanshu Saini, and Praveen Kumar. Mathematical modeling of li-ion battery for charge/discharge rate and capacity fading characteristics using genetic algorithm approach. In *Transportation Electrification Conference and Expo (ITEC), 2012 IEEE*, pages 1–6. IEEE, 2012.
- [83] John R Miller and Andrew F Burke. Electrochemical capacitors: challenges and opportunities for real-world applications. *The Electrochemical Society Interface*, 17(1):53, 2008.
- [84] B Veit, T Hempel, A Pohl, and M Bodach. Investigations on life estimation of ultracapacitors using time domain methods. In *International Multi-Conference on Systems, Signals & Devices*, 2012.

- [85] Application Note. Maxwell technologies boostcap energy storage modules life duration estimation, 2007.
- [86] Vita Lystianingrum, Vassilios Georgios Agelidis, and Branislav Hredzak. State of health and life estimation methods for supercapacitors. In *Power Engineering Conference (AUPEC), 2013 Australasian Universities*, pages 1–7. IEEE, 2013.
- [87] Paul Kreczanik, Pascal Venet, Alaa Hijazi, and Guy Clerc. Study of supercapacitor aging and lifetime estimation according to voltage, temperature, and rms current. *IEEE Transactions on Industrial Electronics*, 61(9):4895–4902, 2014.
- [88] Venkatasailanathan Ramadesigan. Capacity fade analysis and model based optimization of lithium-ion batteries. 2013.
- [89] Long Lam and Pavol Bauer. Practical capacity fading model for li-ion battery cells in electric vehicles. *IEEE Transactions on Power Electronics*, 28(12):5910–5918, 2013.
- [90] Anderson Hoke, Alexander Brissette, Dragan Maksimović, Annabelle Pratt, and Kandler Smith. Electric vehicle charge optimization including effects of lithium-ion battery degradation. In *Vehicle Power and Propulsion Conference (VPPC), 2011 IEEE*, pages 1–8. IEEE, 2011.
- [91] Soren Ebbesen, Philipp Elbert, and Lino Guzzella. Battery state-of-health perceptive energy management for hybrid electric vehicles. *IEEE Transactions on Vehicular Technology*, 61(7):2893–2900, 2012.
- [92] M Safari, M Morcrette, A Teyssot, and C Delacourt. Life-prediction methods for lithium-ion batteries derived from a fatigue approach i. introduction: capacity-loss prediction based on damage accumulation. *Journal of The Electrochemical Society*, 157(6):A713–A720, 2010.
- [93] M Safari, M Morcrette, A Teyssot, and C Delacourt. Life prediction methods for lithium-ion batteries derived from a fatigue approach ii. capacity-loss prediction of batteries subjected to complex current profiles. *Journal of The Electrochemical Society*, 157(7):A892–A898, 2010.
- [94] Muhammad Iqbal. *An introduction to solar radiation*. Elsevier, 2012.
- [95] Ali Mohammad Noorian, Isaac Moradi, and Gholam Ali Kamali. Evaluation of 12 models to estimate hourly diffuse irradiation on inclined surfaces. *Renewable energy*, 33(6):1406–1412, 2008.

- [96] I Supit and RR Van Kappel. A simple method to estimate global radiation. *Solar Energy*, 63(3):147–160, 1998.
- [97] Long Lam, Pavol Bauer, and Erik Kelder. A practical circuit-based model for li-ion battery cells in electric vehicle applications. In *Telecommunications Energy Conference (INT-ELEC), 2011 IEEE 33rd International*, pages 1–9. IEEE, 2011.
- [98] Jorge Nocedal, Andreas Wächter, and Richard A Waltz. Adaptive barrier update strategies for nonlinear interior methods. *Journal on Optimization (SIAM)*, 19(4):1674–1693, 2009.
- [99] Andreas Wächter. *An interior point algorithm for large-scale nonlinear optimization with applications in process engineering*. PhD thesis, PhD thesis, Carnegie Mellon University, Pittsburgh, PA, USA, 2002.
- [100] Demian Pimentel and Petr Musílek. Power management with energy harvesting devices. In *23rd Canadian Conference on Electrical and Computer Engineering (CCECE), 2010*, pages 1–4. IEEE, 2010.
- [101] Hana Besbes, George Smart, Dujdow Buranapanichkit, Christos Kloukinas, and Yiannis Andreopoulos. Analytic conditions for energy neutrality in uniformly-formed wireless sensor networks. *IEEE Transactions on Wireless Communications*, 2013, 12(10):4916–4931, 2013.
- [102] Hongqiang Zhai and Yuguang Fang. Distributed flow control and medium access in multihop ad hoc networks. *IEEE Transactions on Mobile Computing*, 2006, 5(11):1503–1514, 2006.
- [103] Frank P Kelly, Aman K Maulloo, and David KH Tan. Rate control for communication networks: shadow prices, proportional fairness and stability. *Journal of the Operational Research society*, pages 237–252, 1998.
- [104] Steven H Low. A duality model of tcp flow controls. In *Proceedings of ITC Specialist Seminar on IP Traffic Measurement, Modeling and Management*, volume 2, 2000.
- [105] Peng Du, Weixia Zou, Zheng Zhou, Wanxin Gao, Xiaojun Huang, and Haiyang Xin. An active congestion help mechanism in wireless sensor network. In *IEEE Vehicular Technology Conference, 2011*, pages 1–5. IEEE, 2011.
- [106] Steven H Low, Larry L Peterson, and Limin Wang. Understanding tcp vegas: a duality model. *Journal of the ACM (JACM)*, 49(2):207–235, 2002.

- [107] Steven H Low. A duality model of tcp and queue management algorithms. *IEEE/ACM Transactions on Networking*, 2003, 11(4):525–536, 2003.
- [108] Keisuke Nakayama, Nga Dang, Lubomir Bic, Michael Dillencourt, Elaheh Bozorgzadeh, and Nalini Venkatasubramanian. Distributed flow optimization control for energy-harvesting wireless sensor networks. In *2014 IEEE International Conference on Communications (ICC), 2014*, pages 4083–4088. IEEE, 2014.
- [109] Mung Chiang. Balancing transport and physical layers in wireless multihop networks: Jointly optimal congestion control and power control. *IEEE Journal on Selected Areas in Communications*, 2005, 23(1):104–116, 2005.
- [110] Junshan Zhang and Dong Zheng. A stochastic primal-dual algorithm for joint flow control and mac design in multi-hop wireless networks. In *40th Annual Conference on Information Sciences and Systems, 2006*, pages 339–344. IEEE, 2006.
- [111] Fernando Paganini. On the stability of optimization-based flow control. In *Proceedings of the American Control Conference, 2001*, volume 6, pages 4689–4694. IEEE, 2001.
- [112] Dimitri P Bertsekas. *Nonlinear programming*. 1999.
- [113] Hassan K Khalil and JW Grizzle. *Nonlinear systems*, volume 3. Prentice hall New Jersey, 1996.
- [114] Zhe Chen, Juri Ranieri, Rongting Zhang, and Martin Vetterli. *Dass: Distributed adaptive sparse sensing*. 2013.
- [115] Zhilin Zhang, Tzyy-Ping Jung, Scott Makeig, and Bhaskar Rao. Compressed sensing for energy-efficient wireless telemonitoring of noninvasive fetal ecg via block sparse bayesian learning. *IEEE Transactions on Biomedical Engineering*, 60(2):300–309, 2013.
- [116] Wei Chen and Ian J Wassell. Energy-efficient signal acquisition in wireless sensor networks: a compressive sensing framework. *IET Wireless Sensor Systems*, 2(1):1–8, 2012.
- [117] Frezzetti Antonio and Manfredi Sabato. Evaluation of energy efficiency-reconstruction error trade-off in the co-design of compressive sensing techniques for wireless lossy sensor networks. *International Journal of Wireless Information Networks*, 22(4):386–398, 2015.
- [118] Antonio Frezzetti and Sabato Manfredi. A two-layer controller scheme for efficient spatial recovery and lifetime elongation in wireless sensor network. *IEEE Sensors Journal, International Journal of Wireless Information Networks*, 16(7):2172 – 2179, 2015.

- [119] Chun Tung Chou, Rajib Rana, and Wen Hu. Energy efficient information collection in wireless sensor networks using adaptive compressive sensing. In *IEEE 34th Conference on Local Computer Networks LCN*, pages 443–450. IEEE, 2009.
- [120] Alexandras Fragkiadakis, Pavlos Charalampidis, and Elias Tragos. Adaptive compressive sensing for energy efficient smart objects in iot applications. In *4th International Conference on Wireless Communications, Vehicular Technology, Information Theory and Aerospace & Electronic Systems (VITAE)*, pages 1–5. IEEE, 2014.
- [121] Yiran Shen, Wen Hu, Rakesh Rana, and Chun Tung Chou. Nonuniform compressive sensing for heterogeneous wireless sensor networks. *IEEE Sensors Journal*, 13(6):2120–2128, 2013.
- [122] Karl Johan Åström and Tore Hägglund. *Advanced PID control*. ISA-The Instrumentation, Systems, and Automation Society; Research Triangle Park, NC 27709, 2006.
- [123] Reza Olfati-Saber and Richard M Murray. Consensus problems in networks of agents with switching topology and time-delays. *IEEE Transactions on Automatic Control*, 49(9):1520–1533, 2004.
- [124] Sabato Manfredi. Design of a multi-hop dynamic consensus algorithm over wireless sensor networks. *Control Engineering Practice*, 21(4):381–394, 2013.
- [125] Sabato Manfredi Antonio Frezzetti. Enhancing wireless networked monitoring system sustainability by multi-hop consensus algorithm. In *IEEE Workshop on Environmental Energy and Structural Monitoring Systems (EESMS)*, pages 1–6. IEEE, 2014.
- [126] <http://statweb.stanford.edu/candes/l1magic/>.
- [127] Emmanuel Candes and Justin Romberg. Sparsity and incoherence in compressive sampling. *Inverse problems*, 23(3):969, 2007.
- [128] Antonio Frezzetti, S Manfredi, and Mario Pagano. An implementation of a smart maximum power point tracking controller to harvest renewable energy of wireless sensor nodes. In *International Conference on Clean Electrical Power (ICCEP)*, pages 503–508. IEEE, 2013.
- [129] Antonio Frezzetti, Sabato Manfredi, and Mario Pagano. A design approach of the solar harvesting control system for wireless sensor node. *Control Engineering Practice*, 44:45–54, 2015.

- [130] Liuping Wang. *Model predictive control system design and implementation using MATLAB®*. Springer Science & Business Media, 2009.